ACS NANO

www.acsnano.org

REVIEW

Innovative Heating for the Nano Age: Exploring the Potentials of Carbothermal Shock

Jingyun Zou,* Lei Tang,* and Lixing Kang*

Cite This: https://doi.org/10.1021/acsnano.4c12350

Read Online

ACCESS | Metrics & More | Article Recommendations

ABSTRACT: Heating techniques have underpinned the progress of the material and manufacturing industries. However, the explosive development of nanomaterials and micro/nanodevices has raised more requirements for the heating technique, including but not limited to high efficiency, low cost, high controllability, good usability, scalability, universality, and eco-friendliness. Carbothermal shock (CTS), a heating technique derived from traditional electrical heating, meets these requirements and is advancing at a high rate. In this review, the CTS technique, including the material to support CTS, the power supply to generate CTS, and the method to monitor CTS, is introduced, followed by an overview of the progress achieved in the application of CTS, including the modification and fabrication of nanomaterials as well as many other interesting applications, e.g., soldering/welding of micro- and macroscopic carbon materials, sintering of ceramic electrolytes, recycling of Li-ion battery, thermal tips, actuators, and artificial muscle. Problems and challenges in this area are also pointed out, and future developing directions and prospects are presented.

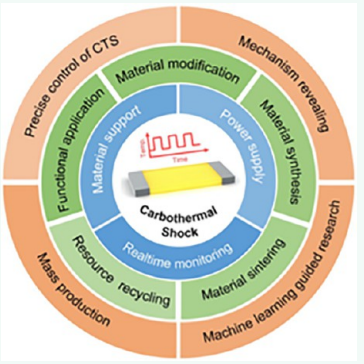

KEYWORDS: *carbothermal shock, flash joule heating, methodology and application, material synthesis, device fabrication, waste recycling, high-throughput synthesis, mass production*

1. INTRODUCTION

The improving heating technique has supported the progress of material preparation, manufacturing, and human society ever since. The usage of fire heating brought light and warmth to ancient human beings and prompted the development of food processing and pottery craft.[1,2] Then, with the improving temperature of fire heating, porcelain, bronzeware, and ironware were made by ancient craftsmen.[3] In modern society, the heating technique advanced with the progress of science and technology and thus supported the industries of modern metallurgy, heat treatment, ceramics, equipment manufacturing, chemical engineering, medicine, etc.[4−6] Nowadays, the emergence of advanced nanomaterials and micro/nanodevices has attracted a lot of attention from academia and industry. Their precise and controllable fabrication or manufacturing puts higher requirements on the heating technique. For example, to fabricate lateral two-dimensional (2D) heterostructures with multiple distinct material blocks, e.g., WS_2−WSe_2−WS_2−WSe_2 and WS_2−MoS_2−WS_2, Zhang et al. designed a complicated step-by-step thermal chemical vapor deposition (CVD) process with a tube furnace to avoid the formation of 2D transition metal dichalcogenide alloys.[7] Excessive thermal degradation or uncontrolled nucleation will take place between sequential growth steps because the low heating and cooling rates of the conventional tube furnace make it unachievable to realize a quick temperature swing. This has become the key obstacle to the controllable growth of monolayer heterostructures with sharp interfaces. To solve this problem, the authors adopted a reverse gas flow from the substrate to the source during the temperature swing to prevent the unintended supply of the chemical vapor source at undesired temperatures and eliminate the uncontrollable nucleation.[7] Yet, if a heating method or equipment can realize the rapid temperature swing, the growth procedure can be radically simplified even for the synthesis of much more complicated 2D lateral heterostructures. Besides, the quick preparation of device-quality 2D materials is crucial for their future application. Some researchers have focused on the ultrafast growth of 2D transition metal dichalcogenides

Received: September 4, 2024
Revised: November 28, 2024
Accepted: December 5, 2024

(TMDCs), e.g., MoS_2 and WS_2.[8,9] However, the heating rate of conventional tube furnaces is quite low. It is hard to precisely distinguish the growth time of the obtained TMDCs. Big errors may exist in the assessed growth speed, and it is difficult to implement the quick preparation of 2D materials when taking the slow heating and cooling processes into account. Hence, an ultrafast heating technique is required to quickly prepare 2D materials.

Low-cost, high-speed, and large-batch preparation or manufacturing is the first prerequisite for the practical application of nanomaterials and micro/nanodevices, but a rapid, scalable, and eco-friendly manufacturing process remains elusive. Taking the industrial fabrication of graphene or, more precisely, reduced graphene oxide (rGO) as an example, the chemical exfoliation process consumes lots of electric energy, water, and other chemical reagents ($KMnO_4$, H_2O_2, H_2SO_4, HCl, $C_6H_8O_7$, etc.) to get graphite oxide (GO), and further chemical or thermal reduction is required to reduce GO into rGO. This method is not in line with the green manufacturing strategy. Besides, the quality of the chemically exfoliated rGO is not good enough to exert the utmost performance of graphene for many applications, such as conductive additives. The bottom-up methods, especially CVD, can yield high-quality nanomaterials, such as graphene, black phosphorus, transition metal dichalcogenide, etc. However, it is quite hard to achieve the mass production of these nanomaterials via this bottom-up method because of the low yield and high cost, and they also do not echo green manufacturing owing to their high energy consumption.

Recently, a state-of-the-art heating technique has been developed by using carbon materials as the heating elements, which is called carbothermal shock (CTS), flash joule heating (FJH), or high-temperature shock (HTS).[10−12] Usually, CTS and HTS are realized based on electric power sources that can output high-power direct or alternating current, while FJH relies on capacitor banks to provide the required electricity.[13,14] The essences of CTS, FJH, and HTS are the same. They are all realized based on the electrical Joule heating effect. So, CTS is used to refer to this innovative heating technique. The robust sp^2 C−C bonding ensures an ultrahigh heating temperature of up to 4000 K.[15,16] The ultrahigh temperature achieved by CTS can force the molting or even evaporation of most materials, laying a solid foundation for the high-temperature synthesis of various materials. The ultrahigh temperature can also cause extremely high crystallinity or graphitization of carbon nanomaterials, facilitating the delicate modification of functional carbon materials. Meanwhile, the low mass density and specific heating capacity yield ultrafast heating and cooling rates, which can reach the level of 10^5 K/s.[17] Such a high heating/cooling rate will facilitate the formation of special materials at nonequilibrium conditions that are hardly realized by conventional heating methods. Besides, an interesting remote Joule heating effect exists in the carbon nanomaterials—carbon nanotubes (CNTs) and graphene.[18] The electric current conducted in CNTs and graphene can couple to the vibrational modes of neighboring materials. This effect makes the heat transfer from the carbon nanomaterial to the neighboring materials more efficient,[19] which further improves the heating efficiency of this cutting-edge heating technique. CTS can also cause highly efficient nonradiation heating, generating localized internal heat in targeted objects.[20] Hence, with low energy consumption, CTS can realize the ultrafast synthesis of nanomaterials and the ultrafast fabrication of devices within seconds or even milliseconds. Moreover, defective sites on the surfaces of carbon heating elements can serve as barriers to suppress agglomeration and coalescence of nanomaterials by surface energy minimization and thus facilitate the fabrication of nanomaterials, especially nanoparticles and single atoms.[21] By tailoring the carbon-based heating element, localized heating can be realized with arbitrary heating configuration from nano/microscale to macroscale.[18,22,23] All these fantastic features make CTS favorable in the fabrication or modification of nanomaterials and micro/nano machining with high efficiency, low cost, and low energy consumption.

Here, we systematically summarize recent progress in the CTS technique and its applications in various fields. As shown in Figure 1, we first briefly introduce how to realize CTS, including the materials to support CTS, the power supply to generate CTS, and measurement methods to monitor CTS. Then, we move on to the application of CTS in the modification of graphene and other 2D materials and then to the synthesis of zero-dimensional (0D), one-dimensional (1D), and 2D materials. We also summarize the application of CTS in several other interesting areas, including the soldering/welding of micro- and macroscopic carbon materials, sintering of ceramic electrolytes, recycling of Li-ion batteries, thermal tips, actuators, and artificial muscles. Finally, the prospects of CTS are outlined. We point out the developing directions of CTS, including the precise control of CTS, the revelation of the mechanism behind CTS, the machine-learning guided synthesis, and the mass production of nanomaterials. We believe that this review will help fledglings to get an overall understanding of this heating technology. It will broaden the horizons of veteran researchers to bring CTS into practical applications in the future.

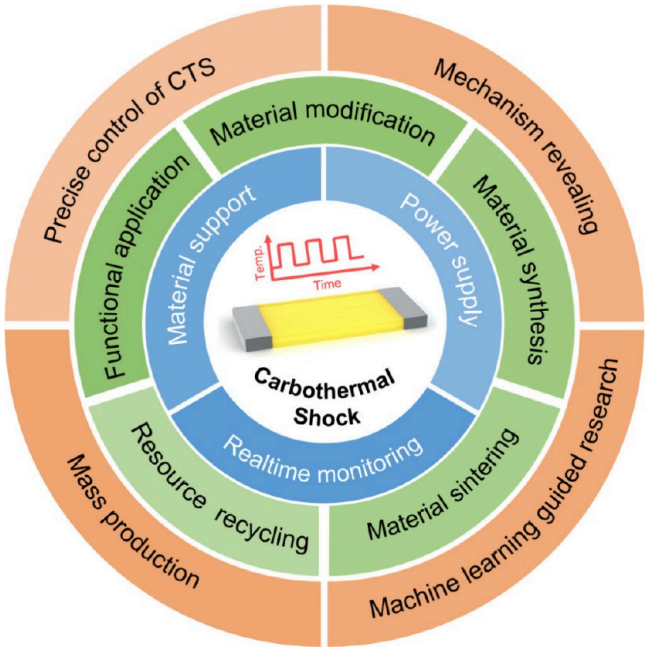

Figure 1. Schematic diagram to show the core content of this review.

2. REALIZATION AND MONITORING OF CTS

2.1. Materials to Support CTS. Various conductive carbon materials have been used to generate CTS, including CNT,[24] graphene,[25] rGO,[26−28] carbon nanofiber (CNF),[10,29,30] carbon fiber,[31,32] and carbonized biomass (e.g., woods).[33,34] Owing to

https://doi.org/10.1021/acsnano.4c12350
ACS Nano XXXX, XXX, XXX−XXX

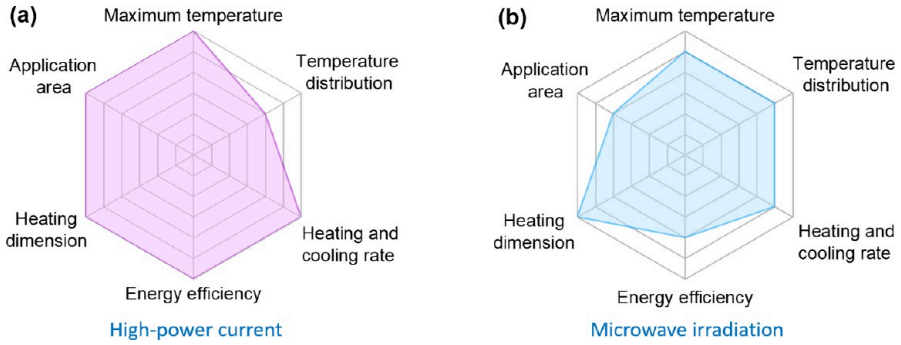

Figure 2. Comparison of the two power supplies. Merits and demerits of (a) the high-power electrical current and (b) the microwave irradiation.

the robust sp^2-hybridized C═C bonds, the highly crystalline carbon materials, especially CNT and graphene, can sustain an extremely high temperature of up to 4000 K.[35] Besides, the mass density and specific heat capacity of carbon materials are much lower than the conventional heating elements made of ZrO_2, SiC, and $MoSi_2$. So, carbon materials' heating and cooling rates are much higher than alloy materials. For instance, the heating and cooling rates of the CNT- or graphene-based heating elements reach 10^3−10^5 K/s.[17,36] Moreover, the assembly of carbon materials usually possesses excellent mechanical performance, including high modulus, strength, and flexibility. The mechanical strength of pure CNT fiber has reached 5.18 GPa, and it can be arbitrarily bent.[37] These fantastic features make nanocarbon materials easily constructed into free-standing or self-supporting heating elements with arbitrary shapes by fiber knitting/soldering, film clipping, or 2D/3D printing. For example, by knitting CNT fibers and soldering the joints, Zou et al. have constructed complex CNT-based heating elements with various 2D and 3D constructions.[22] Graphene-based heaters were fabricated by 2D ink printing.[38,39] Graphene-based probes and miniaturized reactors were constructed by 3D printing.[23,28] Conventional carbon materials, e.g., carbonized wood, carbon fiber, and carbon cloth, can also be used to generate CTS.[31,40,41] For example, carbonized Balsa wood, one of the most typical carbonized biomass, was used as the heating element to generate a high temperature of >2000 K, and the vascular system of the wood directly served as the microreactor for the CTS preparation of nanoparticles.[33]

Next, the heating dimension can be adjusted by increasing the size of these heating elements toward the real application of CTS in the fabrication of micro- and nanomaterials and devices. Besides, the configuration of heating elements should be dedicatedly designed to realize a high heating uniformity and thus guarantee the consistency of products and their performances. The stability of carbon-based heating elements should be evaluated and further improved to elongate the life expectancy and raise the reliability of CTS heating sources. So, more efforts are still in demand to generate reliable in situ CTS from microscale to macroscale to meet the requirements of the scalable synthesis/fabrication of micro- and nanomaterials/devices.

2.2. Power Supply to Generate CTS. An efficient power supply is the other prerequisite for precisely controlling the heating parameters. High-power electrical current and microwave irradiation are the two main sources to support ultrafast carbothermal shocks.

2.2.1. High-Power Electrical Current. The high-power current source is the most used power supply to generate CTS.[42] The input current will force electrons to collide with the lattice, which can significantly enhance the lattice vibration to raise the temperature of carbon heaters. The maximum temperature, heating rate, and burst length of CTS can be well regulated by adjusting the value, ramping rate, and width (time period) of the pulse current. Benefiting from the low mass of carbon atoms and the strong sp^2-hybridized C═C bonds, carbon materials' maximum heating temperature and heating/cooling rates are much higher than conventional alloy heaters. The highest temperature of 3500 K is realized using graphene as the heating element,[25] and the temperature ramping and cooling rates exceed 10^5 K/s.[43] It is also easy to roughly estimate the generated temperature according to the input power. As reported by Wang et al., the average temperature rose from about 1500 to 2000 K while the input current power increased from about 125 to 600 W.[33] For the real application, the relationship between the temperature and input power should be established, which will help to realize the precise control of the temperature progress of CTS. Besides, such a high heating temperature can only be achieved under a high vacuum or inert atmosphere. Trace amounts of oxygen will cause the degeneration or even the failure of thin carbon-based heaters. So, ultrahigh-temperature CTS proposes high demands for the environmental atmosphere. Only low-temperature CTS (T < the thermal oxidation temperatures of carbon heaters) can be performed in the air or an oxidizing atmosphere. Next, antioxidation coatings can be deposited onto carbon-based heaters to extend the application of high-temperature CTS into oxidizing conditions,[44,45] which will also enhance the processing capacity of CTS to handle oxidizing materials.

2.2.2. Microwave Irradiation. Microwave is another feasible power supply to generate CTS. Carbon materials, e.g., CNT, graphene, GO, rGO, and carbon fiber, are good microwave susceptors. They can convert electromagnetic energy to intense thermal energy.[31,46−49] The microwave heating mechanism of these carbon materials is quite different from that of a solution caused by the dipole rotation of polar solvent molecules. No freely rotatable dipoles exist in these electron-rich carbon materials. It is the motion of electrons that generates the heat through Joule heating. In other words, the microwave electric field causes the motion of electrons, enhances the collision of electrons with the lattice, and thus causes the Joule heating of carbon materials. Taking CNT as an example, Ester Vázquez and Maurizio Prato discussed the interaction between CNT and microwave.[46] The imperfections and impurities in CNTs damp the transverse vibration mode to generate Joule heating with an ultrahigh energy flux density. This microwave-motivated heating method generates extremely short thermal shocks of 1600 K within just 100 ms,[49] and it has been used to grow various nanomaterials.[50] For example, since 2006, nanoparticles (NPs),

https://doi.org/10.1021/acsnano.4c12350
ACS Nano XXXX, XXX, XXX−XXX

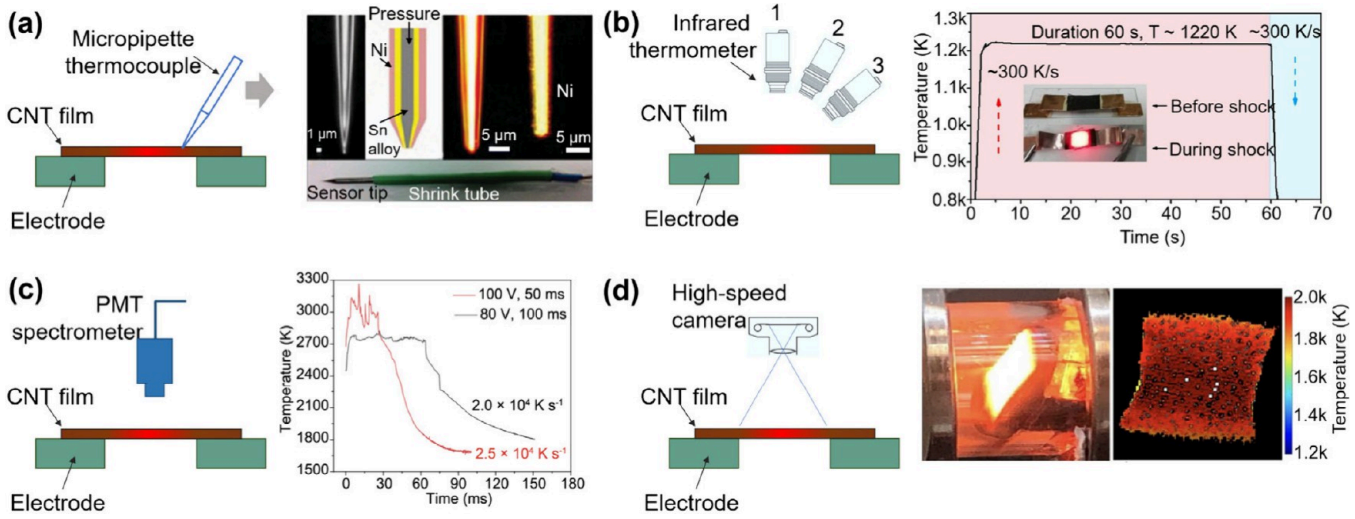

Figure 3. Typical temperature monitoring methods of CTS. (a) Micropipette thermocouple. Reprinted with permission from ref 56. Copyright 2013 AIP Publishing. (b) Infrared thermometer and the detected temperature evolution. Reprinted with permission from ref 41. Copyright 2022 American Chemical Society. (c) Temperature detecting system based on photomultiplier tube arrays and the detected temperature evolution. Reprinted with permission under a Creative Commons CC BY License from ref 11. Copyright 2022 Springer Nature. (d) Color ratio pyrometer based on high-speed camera and the mapped temperature distribution. Reprinted with permission from ref 33. Copyright 2020 Elsevier.

e.g., Au and Pt NPs, have already been decorated on the surface of CNT through the microwave-assisted CTS.[51,52] However, the controllability of microwave-triggered CTS synthesis is much lower because of the difficulty in the direct assessment of the generated temperature from the input power.

Figure 2 summarizes both the merits and demerits of the two power supplies. With the use of high-power electrical current, most of the electrical energy can be converted into thermal energy, and an extremely high heating temperature can be reached in the carbon-based heating element. However, the temperature generated by the current is not uniform. Usually, the temperature gradually lowers from the center to the periphery of the heating element. In contrast, the temperature generated by microwave irradiation is uniform, which will benefit the CTS-triggered controllable synthesis of nanomaterials. However, only part of the microwave irradiation can be absorbed by carbon materials. Its energy efficiency is lower than the current-supplied CTS, and so is the temperature. Besides, with the quick turn on/off of current or the use of pulse current, the heating and cooling rate of CTS is higher than that realized with the input of microwave irradiation. The heating dimensions can be easily enlarged by increasing the size of the carbon heating element and the input energy. This feature is critical for the future large-scale applications of CTS. Besides, the electrical current-supplied CTS can be used to fabricate nanomaterials and many other interesting applications, e.g., actuator and thermal tip. So, the possible application area of electrical current supplied CTS is wider than the microwave-triggered one.

2.3. Methods to Monitor CTS. Accurate measurement of the temperature procedure is essential for the precise control of CTS and its application in different fields. Key parameters of CTS, including the maximum temperature (T_{max}), heating rate (K_h), cooling rate (K_c), shock-on and shock-off duration (τ_{on} and τ_{off}), should be monitored to get a thorough understanding of the CTS technology and its effects on the modification and synthesis of nanomaterials. Throughout recently published works, contact and contactless methods were used to characterize the temperature procedure of CTS, including thermocouples, infrared thermometers, temperature detecting systems based on photomultiplier tube arrays, and color ratio pyrometers based on high-speed cameras.

2.3.1. Thermocouple. The utilization of thermocouples can get the precise temperature of CTS in a wide range from room temperature to 2500 °C, depending on the material of the thermocouple. It has been applied in the carbothermal reduction of Al_2O_3, ZnO, and SiO_2, as well as the fabrication of ZnN and SiC.[53−55] A micropipette thermocouple with a tiny sensing tip is used to detect the temperature gradient across the suspended CNT film (Figure 3a).[56] The sensing tip size varies from 2 to 5 μm, which yields a high spatial resolution. Meanwhile, this micropipette thermocouple has a high accuracy and can measure thermal fluctuation with a resolution of ±0.01 K. However, the drawbacks of thermocouples are obvious. First, it takes a certain time to reach the heat balance, as sufficient heat exchange should be completed between the thermos-element and the object under test. So, there is a delay in the temperature measurement, which makes thermocouples unsuitable to measure high-frequency thermal shocks or get the real-time temperature procedure of CTS. Second, thermocouples can be easily affected by the external electromagnetic field. The existence of high-power current pulses and microwaves will disable the thermocouple. So, thermocouples are not universal in measuring the temperature profile of CTS.

2.3.2. Infrared Thermometer. As one of the most commonly used contactless temperature measuring methods, infrared thermometers can quickly collect the high temperature up to 3723 K (3500 °C). Many researchers have adopted infrared thermometers to measure the temperature procedure of CTS.[41,57,58] The operation is very simple, as shown in Figure 3b. Usually, several infrared temperature probes are needed to ensure accuracy and cover the temperature range from room temperature to the desired ultrahigh temperature. It will cause many inconveniences for the real application of CTS, especially some microzone reactions. Besides, the response time of infrared thermometers is more than 20 ms. So, it can detect the highest temperature of CTS but cannot accurately depict the rapid

https://doi.org/10.1021/acsnano.4c12350
ACS Nano XXXX, XXX, XXX−XXX

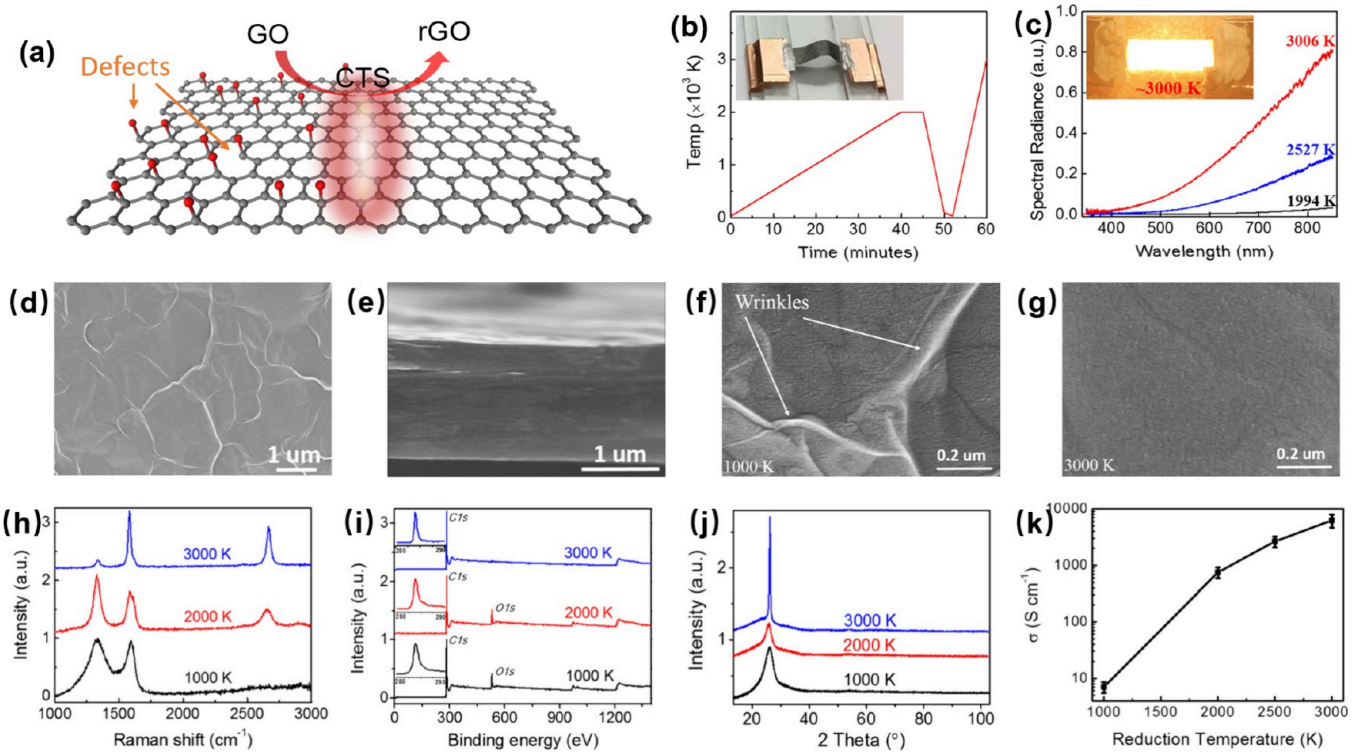

Figure 4. CTS-induced reduction of GO. (a) A two-step reduction of GO film via CTS. (b) The temperature procedure of a CTS process, (c) radiance spectra of the rGO film at different temperatures, in which the inset shows an optical image of the rGO film heated to 3000 K, (d, e) SEM images to show the top view (d) and cross-section (e) of the 3000-K-reduced rGO film, (f, g) high-resolution SEM images to show the surface morphology of the 1000-K-reduced (f) and 3000-K-reduced (g) rGO films, (h) Raman spectra, (i) XPS spectra, and (j) XRD patterns of rGO films reduced at 1000, 2000, and 3000 K, and (k) room-temperature conductivities of rGO films reduced at 1000 K, 2000 K, and 3000 K. Reprinted with permission from ref 74. Copyright 2018 Elsevier.

heating and cooling process of CTS or the high-frequency temperature change. The detected heating and cooling rates are only 300 K/s (Figure 3b).[41] Recently, with the advancing infrared-sensitive materials, the maximum detecting temperature and response speed of infrared thermometers have improved significantly, reaching the level of 3600 °C and 1 ps (response time), respectively.[59,60] Customized infrared thermometers or imaging systems targeted are in urgent demand to monitor the temperature evolution or even the temperature distribution of CTS in real-time.

2.3.3. Temperature Detecting System Based on Photomultiplier Tube Arrays. Using a 16- or 32-channel photomultiplier tube (PMT) array, the spectral radiance from the heating element can be collected in a certain wavelength range (Figure 3c).[11,61] Then, the emission spectra can be fitted to the graybody radiation equation (eq 1) to get the temperature.

$$L_\lambda(\lambda, T) = \frac{2hc^2\gamma\varepsilon_{\text{gray}}}{\lambda^5\left[\exp\left(\frac{hc}{\lambda k_B T}\right) - 1\right]} \quad (1)$$

where L_λ, λ, T, c, k_B, h, $\varepsilon_{\text{gray}}$, and γ are the radiance, wavelength of the emitted light, temperature, light speed, Boltzmann constant, Planck constant, constant emissivity, and scaling constant considering the unknown coupling factor, respectively. Owing to the ultrafast response of PMT (at the level of several nanoseconds),[62] this temperature detecting system can record the real-time temperature procedure of CTS. For example, Deng et al. reported an ultrafast CTS heating rate of 10^4 K/s (Figure 3c),[11] and Xie et al. demonstrated that the heating rate reached 10^5 K/s by monitoring the real-time temperature program with a PMT system.[61] These researches have confirmed that the PMT system is one of the most suitable methods to monitor the temperature profile of CTSs.

2.3.4. Color Ratio Pyrometers Based on High-Speed Camera. High-speed cameras can record the video of CTS processes at thousands of frames per second (e.g., 4000 frames/s captured by the Vision Research Phantom Miro M110 camera), and then temperature measurement can be performed using color ratio pyrometers based on the recorded frames (Figure 3d), which can be calibrated by blackbody infrared light source to ensure the accuracy.[33,63] Raw pixel values extracted from video files using a custom MATLAB script are demosaiced to recover the values for the red, green, and blue channels at each pixel. Then, to determine the temperature, three ratios of different color channels (green/red, blue/green, and blue/red) for theoretical pixel intensity will be calculated with the following equation:

$$\frac{I_i}{I_j} = \frac{\psi_i \int L(\varepsilon, \lambda, T)\chi_i(\lambda)\, d\lambda}{\psi_j \int L(\varepsilon, \lambda, T)\chi_j(\lambda)\, d\lambda} \quad (2)$$

where I, ψ, ε, λ, and T are the channel intensity, channel gain, emissivity, wavelength, and temperature, respectively. χ is the spectral response of the channel as a function of wavelength, respectively. The radiance L is given by eq 1. Calibration factors ($C_{ij} = \psi_i/\psi_j$) can be applied to these ratios and matched to the theoretical curves with a minimization algorithm by using the following equation:

https://doi.org/10.1021/acsnano.4c12350
ACS Nano XXXX, XXX, XXX−XXX

$$\left(\frac{I_i}{I_j}\right)_{exp} = C_{ij}\left(\frac{I_i}{I_j}\right)_{theor} \quad (3)$$

Finally, the temperature can be calculated by fitting the emitted light spectra according to the gray body radiation (eq 1). As the shot frame per second of high-speed cameras can reach millions or even higher, this method can easily trace CTS's ultrafast heating and cooling procedure. Meanwhile, the temperature distribution throughout the heating element can also be depicted (Figure 3d), which will help to precisely control the CTS process. So, color ratio pyrometers are another powerful method to monitor the temperature profile of CTS. The cost and dimension of the equipment are the two main challenges to integrate the high-speed camera into the CTS system.

These four temperature monitoring methods have their own advantages and disadvantages, which are applicable to different applications of CTS with different requirements. For example, thermal couples can be used to monitor carbon heating elements operated at "low temperatures", such as defogging devices,[64] flexible heating fabric,[65] and those in situ nanomaterial synthesis systems without the need for ultrahigh temperatures and ultrafast thermal shocks.[54] Temperature-detecting systems based on photomultiplier tube arrays and color ratio pyrometers based on high-speed cameras are highly efficient in dealing with high temperatures, making them suitable for detecting ultrahigh temperature and ultrafast thermal shock. But they are less effective in the low temperature region, which needs the complement of thermocouples or infrared thermometers. The advance of infrared-sensitive materials have improved significantly to 3600 °C and 1 ps (response time), respectively.[59,60] So, with the improving infrared temperature measurement technology, infrared thermometers and photodetection systems will become the optimal method to monitor the temperature evolution of CTS with high spatial and temporal resolutions, which are almighty in low, high, and ultrahigh temperature regions.

3. APPLICATION OF CTS

3.1. Modification of Materials. With the ultrahigh temperature and superfast ramping/cooling rate, CTS can be used to modify the composition, morphology, structure, and properties of various nanomaterials, e.g., graphene oxide (GO), CNT, and 2D TMDCs. Early in 2002, Avetik et al. have utilized microwave heating to purify CNTs.[66] Zou et al. used Joule heating to remove organic molecules inside CNT assemblies to modify the mechanical properties of CNT fibers.[67] However, these works have not exerted the utmost potential of CTS in material modification as the heating temperature and ramping/cooling rate are rather limited in these works. By increasing the input power, ultrahigh temperatures can be generated to reduce GO, further modification of rGO, and structure and phase transition of 2D TMDCs.

3.1.1. GO Reduction. As the early exploratory works reported, GO can be effectively reduced once the temperature reaches about 1050 °C in an argon atmosphere or 800 °C in a hydrogen atmosphere.[68,69] These high temperatures can be easily reached by CTS in a vacuum or under nonoxidizing conditions. Hence, CTS becomes a feasible method for the effective mass production of rGO.[70−72] For example, as schematically shown in Figure 4a, with the input of a high-power current pulse (50 ms in duration), CTS with tunable high temperatures (1000−2000 K) is generated in the GO−CNT hybrid to fulfill the reduction of GO, in which CNTs were added to make the GO−CNT hybrid conductive.[73] Compared with the conventional heating method, CTS not only motivates the reduction of GO but also maintains the aperiodic porous structure and flexible feature of the hybrid material. To be specific, the structural defects are repaired, the aromatic structures are recovered by CTS, and meanwhile, CNT strands interweave in the hybrid to create nanopores (>50 nm in size). The obtained porous GO-CNTare favorable for mass transport. Interestingly, organic constituents and functional metal particles with higher melting points are prevalent in the reduced GO−CNT hybrid after the CTS treatment, which is crucial to improve the electrochemical performance of this hybrid material.[73] Therefore, the CTS-reduced GO−CNT shows excellent electrochemical performance with the well-modified component and porous microstructure. The specific capacitance of this GO−CNT electrode reached 45 F/g, coupled with a high capability.[73]

The conductive additives can be abandoned by preannealing GO at a relatively low temperature via conventional furnace heating to make GO conductive. Then, ultrafast CTS treatment can be performed on the preannealed GO to complete the full reduction at an elevated temperature. As reported by Wang et al., GO films are preannealed at 1000 K for 1 h in an argon-filled furnace to make it electrically conductive with a conductivity of 7 S/cm.[74] Then, a direct current (DC) is applied to the preannealed sample to generate CTS with the maximum temperature reaching 2000−3000 K. Figure 4b shows this two-step reduction method via CTS, while Figure 4c shows the pyroluminescence of the rGO film during the CTS reduction process and the corresponding radiance spectra obtained at different temperatures. Figures 4d and 4e show the top view and cross-section of the 3000-K-reduced rGO film. The rGO flakes were randomly oriented in the plane and densely layer-by-layer stacked in the vertical aspect. It should be noted that the temperature of CTS greatly affected the morphology of the obtained rGO film. Lots of wrinkles existed in the 1000-K-reduced film, while the 3000-K-reduced one was quite smooth (Figures 4f and 4g). The crystallinity of the as-obtained rGO films increased with the temperature of CTS as reflected by the increased Raman intensity ratio of I_G/I_D, the reduced core level of O 1s in the XPS spectra, and the sharper XRD peak (Figures 4h−j). Meanwhile, the conductivity of the rGO film improved with the increasing temperature of CTS. As shown in Figure 4k, the room-temperature resistances of the obtained rGO films improved to 750 S/m, 2650 S/m, and 6300 S/m after being reduced by CTS at 2000, 2500, and 3000 K, respectively. The high electrical conductivity of the rGO film reduced at 3000 K originated from the high crystallinity as reflected by the decreased intensity ratio of Raman D and G peaks (I_D/I_G = 1.05 for the 1000-K-preannealed GO and 0.1 for the 3000-K-reduced rGO) and the significantly increased C/O atomic ratio (7.8 for the 1000-K-preannealed GO and 130.6 for the 3000-K-reduced rGO).[74]

GO reduction can also be realized via CTS without the help of conductive CNTs or preannealing treatment.[75,76] For the continuous GO film formed by drop-casting, Yao et al. observed an accelerated current increase when a voltage was applied to the film and swept from 0 to 30 V.[75] Or with a constant voltage (30 V for 77 s), the current increased from ca. 1×10^{-8} A to ca. 5×10^{-5} A. The intensity ratio of Raman D and G peaks decreased after the current treatment. All these results demonstrated that the electric stimuli caused the reduction of GO film through this

https://doi.org/10.1021/acsnano.4c12350
ACS Nano XXXX, XXX, XXX−XXX

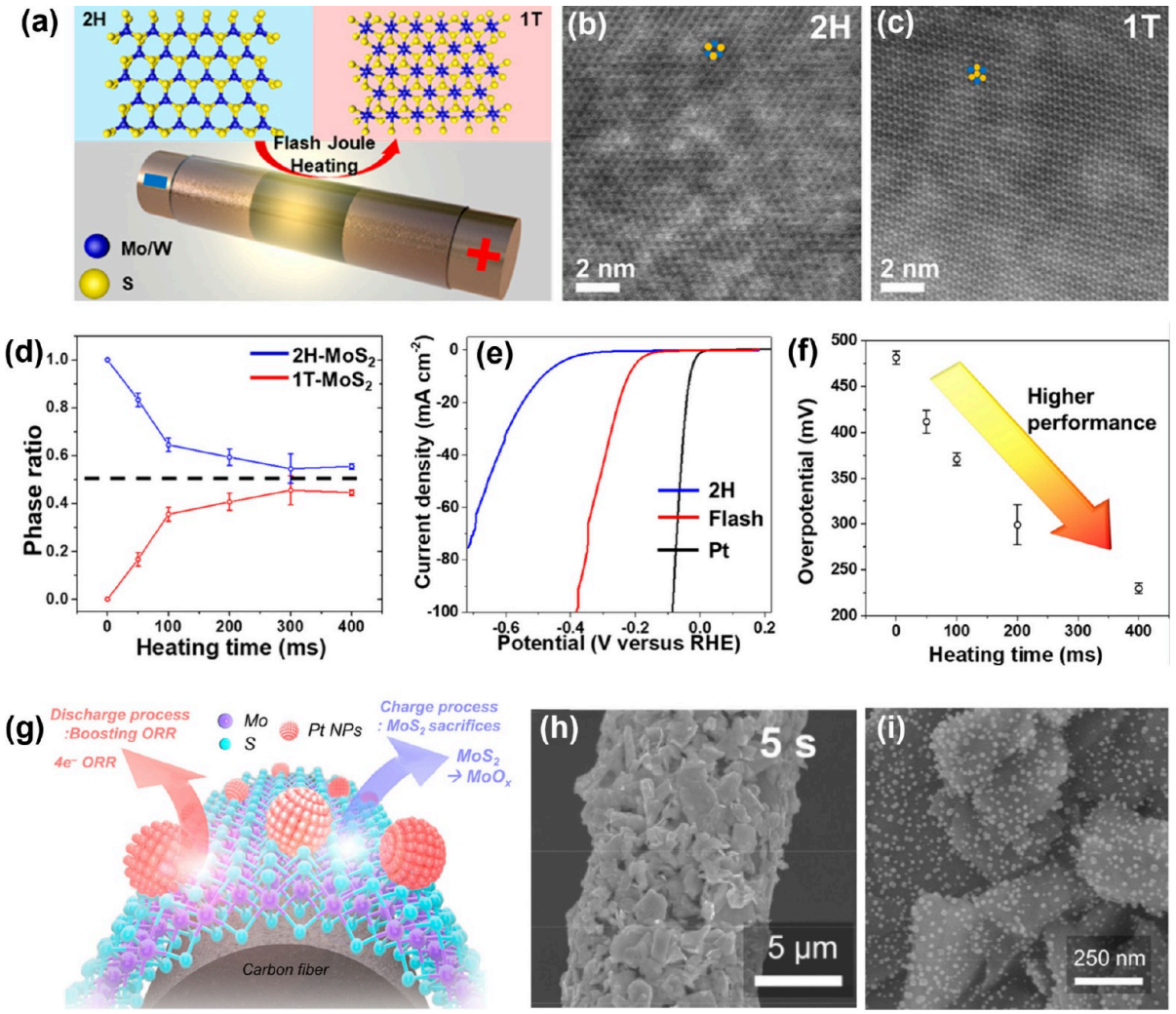

Figure 5. CTS-induced phase transition of MoS_2. (a) Schematic of the setup for the 2H-1T phase transition of MoS_2 via CTS, (b) atomic structure of 2H MoS_2 and (c) 1T MoS_2, (d) the 2H-1T phase ratio versus CTS treating time, (e) polarization cures of 2H and 1T MoS_2, and (f) the relationship between electrochemical overpotential at 10 mA/cm^2 and the CTS treating time. Reprinted with permission from ref 86. Copyright 2021 American Chemical Society. (g) Schematic of the coaxial 1T-MoS_2/carbon felt decorated with Pt NPs, (h) morphology of the 1T-MoS_2/carbon felt, and (i) the distribution of Pt NPs on MoS_2 flakes. Reprinted with permission from ref 88. Copyright 2023 American Chemical Society.

clean and dry method. And the obtained rGO can be directly used as efficient electrodes in organic photoswitching devices. However, this CTS reduction of GO was performed in air, and the maximum temperature of CTS was quite low (<100 °C). So, the crystallinity of the obtained rGO was relativity low, as reflected by the strong Raman D peaks. Interestingly, in another work, Ekiz et al. found that the low-temperature CTS realized by small current pulses could realize the reversible reduction and oxidation of GO.[76] GO at the positive contact was oxidized, whereas GO at the negative contact was reduced when a bias of ±2.5 V was applied. The oxidation and reduction of GO were reversed by inverting the bias. These CTS-reduced GO can be applied as functional materials in various applications including energy and opto-bioelectronic devices.

When using microwave irradiation as the energy input, both the introduction of foreign conductive heating elements and the preannealing treatment can be discarded, further improving the convenience and lowering the cost of the CTS-triggered GO reduction.[77−80] Moreover, some rewarding phenomena will further extend the application of microwave-induced CTS in the reduction of GO. For example, O.-K. Park et al. revealed that defects inside GO were repaired by the intercalated benzene during the microwave-induced CTS process.[81] The strong $\pi-\pi$ interaction made benzene tightly adhere to the surface of GO, and these low-molecular-weight benzenes decomposed into acetylenes following the reaction of $C_6H_6 \rightarrow 3CH_2$ when being heated up by the surrounding GO sheets with the help of the high-power microwave. Then, through the carbon atom incorporation and H_2-releasing process, the formed acetylenes could bond to the carbon atoms at the divacancy sites to form covalent C−C bonds. Consequently, defects in the obtained rGO were well repaired as reflected by the declined Raman 2D peak.[81] Acetylene has been confirmed to be one of the most promising carbon sources to repair defects in graphene sheets.[82] So, the crystallinity of this CTS-treated rGO dramatically improved. However, it should be noted that the high-power microwave can also destroy the graphene lattice and generate more structural defects.[83] So, by controlling the input microwave power, the crystallinity of rGO can be carefully tailored within a few seconds.

https://doi.org/10.1021/acsnano.4c12350
ACS Nano XXXX, XXX, XXX−XXX

Overall, CTS not only becomes an efficient means to fulfill the bulk reduction of GO via the deoxygenation reaction but also provides an effective method to regulate the defect level of the obtained rGO according to specific demands. With the improving CTS technique, more complicated surface modification will be done to rGO, such as the in situ doping of heteroatoms and the graft of functional groups. More importantly, owing to the easy implementation of CTS, the production of rGO can be easily scaled up to realize large-scale industrial manufacturing.

3.1.2. Further Modification of RGO. The ultrahigh carbothermal temperature can further modify the morphology, structure, and property of rGO assemblies produced by other reduction methods, e.g., chemical and thermal reductions. For instance, the rGO film obtained by annealing GO film at 773 K in an argon atmosphere exhibited a smooth surface morphology after being further treated by CTS at an ultrahigh temperature of 2750 K. The crystallinity of the CTS-treated rGO film improved greatly, as reflected by the dramatically reduced Raman I_D/I_G ratio. Meanwhile, the film's conductivity increased by 76-fold from 40 S/cm to 3023 S/cm after the CTS treatment.[84] The authors attributed the improved electrical conductivity to two main reasons: (i) the improved crystallinity of rGO as the defects were self-healed at such high temperatures; (ii) interlayer bridging bonds between neighboring rGO layers which were formed at the defective sites, e.g., vacancies, grain boundaries, voids, line defects, and so forth. The DFT calculation confirmed that when heated from 300 to 1420 K, the adjacent rGO layer was not bonded as the interlayer sliding took place between the top and bottom rGO layers, which was driven by thermal fluctuation. At higher temperatures, interlayer bridging bonds formed as the interlayer sliding closed the defects in the top and bottom layers. With the interlayer bonding, this highly conductive rGO film also showed high flexibility, making it a promising candidate for the ultralight current collector in various batteries.[84]

Combining the roll-to-roll fabrication technique, Liu et al. continuously fabricated graphene films from the chemically reduced rGO films via CTS.[85] To be specific, the GO film was first blade-coated onto the glass substrate from the GO dispersion and chemically reduced by hydroiodic acid at 90 °C. Then, the obtained rGO film was repeatedly washed with ethanol and further thermally reduced at 300 °C. Finally, the rGO film was cut into strips to undergo the CTS treatment through a continuous roll-to-roll method. When CTS-treated at an ultrahigh heating temperature of 2835 °C, impurities were removed, and defects were repaired. The rGO strips were fully converted into graphene strips with excellent flexibility as well as high electrical and thermal conductivities of 4.2×10^5 S/m and 1285 W/(m·K), respectively. So, CTS provides a time-saving, energy-efficient, and cost-effective method to realize the mass production of graphene films and thus lay a solid material foundation for the scale-up applications of graphene in thermal management, energy batteries, and flexible electronic devices.

3.1.3. Phase Transition of 2D Materials. CTS can motivate the phase transition of 2D TMDCs. As reported by Chen et al., MoS_2 and WS_2 were converted from the 2H phase into the 1T phase within milliseconds via CTS (Figures 5a–c).[86] To be specific, MoS_2 or WS_2 was mixed with 5 wt % carbon black to perform the CTS treatment. The converted 1T phase MoS_2 and WS_2 were confirmed by Raman, high-resolution transmission electron microscopy (HR-TEM), and high-angle dark-field scanning TEM (HAADF-STEM). Changing the conductive additive from carbon black to tungsten increased the conversion efficiency significantly to 76%. It was attributed to tungsten's strong electron doping effect because it lowered the formation energy of 1T-MoS_2 and stabilized this metastable phase.[87] The conversion ratio could also be regulated by changing the duration of CTS. As shown in Figure 5d, the ratio of 1T-MoS_2 increased with the increasing duration, contributing to the improved electrochemical properties of the product (Figures 5e and 5f).

More efforts were made to establish the relation between conversion ratio and CTS parameters. As reported by Son et al., a coaxial 1T-MoS_2/carbon felt was directly fabricated by a similar CTS conversion (Figures 5g and 5h), and the ratio of converted 1T-MoS_2 increased with the stepwisely elongating CTS duration.[88] The authors also confirmed that the charge transfer dramatically promoted the 2H-1T phase transition as the conversion ratio was finite until Pt precursor, H_2PtCl_6, was added. During this conversion process, Pt nanoparticles with diameters of 10−15 nm were uniformly decorated on the surface of MoS_2 flakes (Figure 5i). Hence, Pt-decorated 1T-MoS_2 with high ORR activity was fabricated via CTS, which can be used in seawater batteries with an ultralong lifespan.[88] The CTS treatment can also improve the interfacial interaction between CNT and MoS_2. The CTS generated by CNTs forced the inside-out crystallization of MoS_2 and yielded a robust interface between CNTs and MoS_2 flakes electrodeposited on the CNTs' surface.[89] The obtained composites showed high electrical and mechanical properties. The modulus, strength, and axial electrical conductivity reached up to 8.82 ± 5.5 GPa/SG, 200 ± 58 MPa/SG, and 1.72×10^5 S/m, respectively, making this CNT/MoS_2 composite a good candidate for battery electrodes.

Though only the 2H-1T phase transition of MoS_2 has been reported, however, considering that most of the found TMDCs have two or more phases, CTS will extend its application in the phase modification of TMDCs. At present, the researchers have not yet figured out how MoS_2 and other TMDCs change during the ultrafast CTS process. More efforts are still needed to understand the thermodynamic and kinetic mechanisms of the phase transition process and, thus, to guide the controllable phase transition of TMDCs. Next, the controllability of this ultrafast modification process can be further improved with the introduction of various control parameters, e.g., temperature, heating duration, gas composition, and pressure, and in situ doping engineering of these nanomaterials besides TMDCs can be accomplished by CTS with the introduction of doping agents to further modify the composition, defect level, and phase structure of obtained rGO, TMDCs, and other nanomaterials for better performances.

3.2. Synthesis of Nanomaterials. Owing to the ultrahigh temperature it can reach, CTS can activate the decomposition and reaction of almost all chemical substances, making it applicable in synthesizing nanomaterials with different dimensions. Together with the ultrahigh ramping and cooling rate, CTS can expand both the source of raw materials and the composition of the products.

3.2.1. Growth of 0D Materials. 3.2.1.1. Nanoparticles. CTS has shown tremendous potential in the low-cost and scalable manufacture of miscellaneous nanoparticles (NPs).[90−92] Currently, microparticles or melt salt/metallo-organic compounds have been introduced into the carbon matrix as the precursors to fabricate NPs following the top-down or bottom-up strategies, respectively. For example, in 2006, Chen et al. reported that silicon, tin, and aluminum particles with diameters

https://doi.org/10.1021/acsnano.4c12350
ACS Nano XXXX, XXX, XXX−XXX

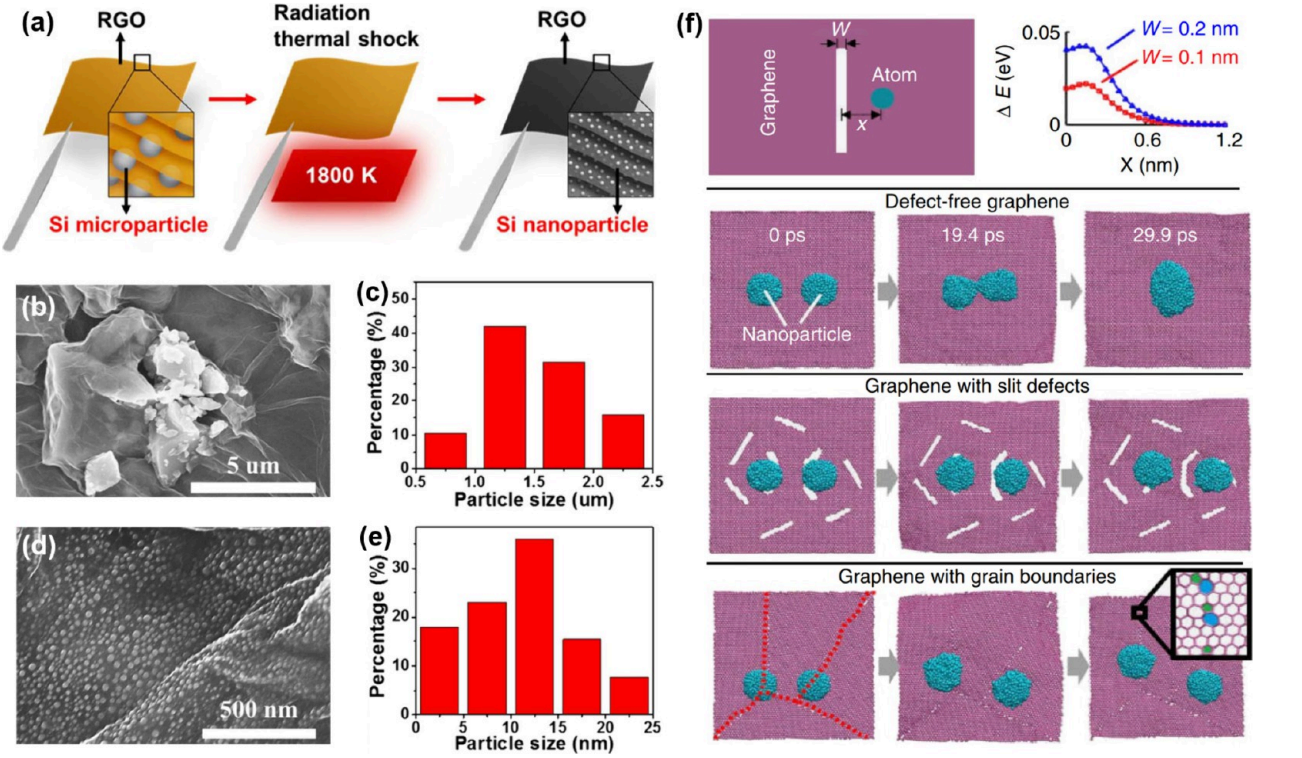

Figure 6. Top-down fabrication of nanoparticles. (a) Schematic to show the fabrication process, (b) microparticles embedded in rGO matrix and (c) their size distribution, (d) as-fabricated nanoparticles and (e) their size distribution. Reprinted with permission from ref 93. Copyright 2016 American Chemical Society. (f) Defects-constrained formation mechanism of nanoparticles. Reprinted with permission under a Creative Commons CC BY License from ref 21. Copyright 2016 Springer Nature.

on the order of a few micrometers embedded in the rGO matrix were converted into NPs with diameters of 10−15 nm in less than 1 min via CTS (1550−1800 K).[93] Figures 6a−e show the fabrication process, the source—microparticles, the product—NPs, and their size distributions. The short synthesis time effectively suppressed the agglomeration of the formed NPs. Once the hold time of CTS was elongated to 1 h, the size of as-synthesized Si NPs increased to 50 nm. In another work published by the same team, the authors proposed the formation mechanism of NPs in the rGO matrix during the CTS process.[21] Taking Al NPs as an example, they elaborated that the Al microparticles melt and vaporized under the Joule heating-induced high temperature. When cooled at an ultrahigh speed, the Al vapor aggregated and condensed to form NPs. During this process, the inevitable defects (e.g., vacancies, grain boundaries, and voids) in the rGO matrix served as effective barriers to constrain the migration of NPs within one domain demarcated by neighboring defects (Figure 6f). Hence, the agglomeration of Al was prevented to form Al NPs with the desired nanoscale size/diameter.

For the bottom-up strategy, melt salt or metallo-organic compounds are introduced into the carbon matrices through drop casting or immersing. For example, the ethanol solution of $CuCl_2$ was drop-casted onto cellulose, and then the hybrid was supported on a carbon paper to perform the CTS treatment.[42] After being treated by CTS at 830 °C for 1.5 s, Cu NPs were formed and densely distributed on the surface of cellulose (Figure 7a). By changing the hold time of CTS, the average size of formed Cu NPs was regulated. The average size decreased from 52 to 35 nm when the hold time increased from 0.4 to 1.5 s, but further increasing the hold time could not decrease the particle size (Figure 7b). Another work systematically studied

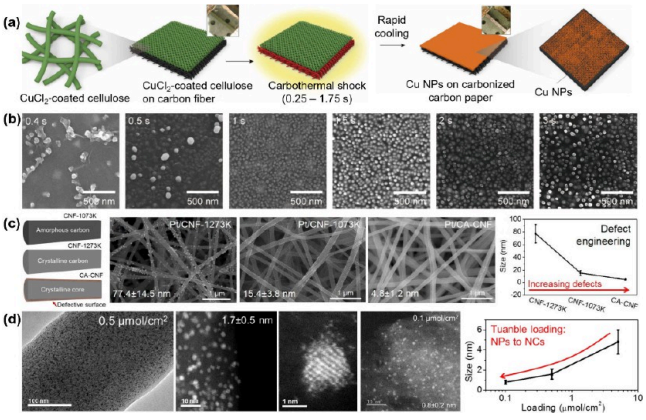

Figure 7. Bottom-up synthesis of nanoparticles. (a) Schematic of the synthesis process and (b) the as-synthesized Cu NPs with different holding times of CTS. Reprinted with permission from ref 42. Copyright 2021 AAAS. (c) Particle size control via defect engineering and (d) particle size control via precursor loading engineering. Reprinted with permission from ref 94. Copyright 2019 American Chemical Society.

the size and distribution control of the as-synthesized NPs.[94] The high-concentration defects in the CNF matrix promoted the uniform distribution and miniaturization of the formed Pt NPs (Figure 7c). The particle size decreased from 77.4 nm on the defect-less CNF-1273K (CNF carbonized at 1273 K) to 4.8 nm on the defect-rich CA-CNF (CO_2-activated CNF-1273K). Besides, the metal precursor's loading amount also affected the Pt NPs' size. By decreasing the precursor loading from 5 to 0.1 μmol/cm^2, the particle size substantially decreased from about

https://doi.org/10.1021/acsnano.4c12350
ACS Nano XXXX, XXX, XXX−XXX

4.8 to 0.8 nm (Figure 7d). Hence, with a low precursor loading, high-density and ultrasmall Pt NPs were loosely packed on the surface of the CA-CNF matrix, which would aggrandize the active sites for various catalytic applications.

Further, through precursor design, compound or alloy NPs were synthesized via CTS.[27,41,95−104] Deng et al. reported that various interstitial transition metal carbide (TiC, ZrC, HfC, VC, NbC, TaC, Cr_2C_3, MoC, and W_2C) and covalent carbide (B_4C and SiC) NPs were produced from low-cost precursors.[11] The noncarbon precursors (Ti, $Zr(OH)_4$, HfO_2, VO_2, $NbCl_5$, $TaCl_5$, Cr, $MoCl_3$, WO_3, B, or SiO_2 powder) were mixed with the carbon black to accomplish the CTS growth process. The heating temperature reached ∼2700 K and ∼3000 K with different applied voltages, and the discharging time was only 50 ms. Then, the sample cooled down at a high rate of 10^4 K/s to get the carbide NPs. The formation of carbide nanoparticles might follow the inverse gas−solid reaction interface theory. As the vapor pressure of the noncarbon precursors is higher than that of carbon (carbon sublimes at an extremely high temperature of ∼3900 K[105]), the noncarbon precursors were volatilized by CTS and reacted with the solid carbon source to form the carbide NPs with higher catalytic activity than products formed from traditional carburization process. Besides, CTS could accomplish the phase-selected synthesis of molybdenum carbide NPs. By increasing the voltage, i.e., the heating temperature, pure β-Mo_2C, α-MoC_{1-x}, and η-MoC_{1-x} were synthesized. The ab initio calculation results demonstrated that the carbon vacancies dominated the energy landscape of the Mo−C system and drove the topotactic transition from β-Mo_2C to α-MoC_{1-x} and then η-MoC_{1-x}. More importantly, the ultrafast CTS process permitted the formation of these metastable phases and helped to retain these metastable phases kinetically.

Except for the metal carbide, binary alloy NPs were also synthesized. Using $H_2PtCl_6{\cdot}6H_2O$ and $CoCl_2$ solution as the precursors, bifunctional Pt−Co alloy NPs with different compositions were in situ synthesized by changing the precursor ratio on the carbon felt.[98] By adjusting the duration time of CTS (1−10 s) and the precursor concentration (0.01−0.04 M), the size and distribution of the synthesized Pt−Co NPs were well controlled. Also, the Gibbs free energy (ΔG_{*O}) for the catalyst surface to bind O intermediates was modulated by changing the component of the nanoparticle. The Pt−Co NPs with the optimal component exhibited a ΔG_{*O} of 2.34 eV, close to the optimal oxygen-binding strength. Seawater battery with this alloy-NP-loaded carbon felt as the current collector yielded an improved overpotential and cycle endurance for OER and ORR reactions.[98]

More significantly, CTS can fulfill the synthesis of high entropy alloy (HEA) NPs by taking advantage of the ultrahigh heating temperature and the ultrafast heating and cooling rate. In 2018, Yao et al. reported the CTS synthesis of NPs with binary to octonary components.[10] As shown in Figure 8a, the mixture of metal salt MCl_xH_y (M is Pt, Pd, Ni, Fe, Co, Au, Cu, or Sn, among others) solutions were loaded onto a conductive carbon support, e.g., carbon nanofibers (CNFs). The ultrahigh temperature of 2000 K generated by CNFs caused the complete decomposition of these metal salts and prompted the formation, fission, and fusion of liquid metal particles (Figure 8b). So, a solid solution formed during the 55 ms thermal shock protocol when binary to octonary metallic elements were mixed to maximize the mixing entropy. Then, the ultrafast cooling rate facilitated the kinetic control over the thermodynamic mixing

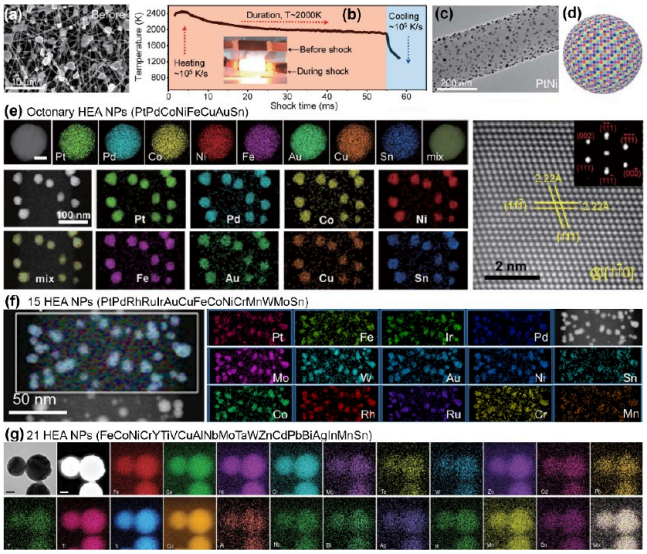

Figure 8. CTS synthesis of HEA NPs. (a) Precursors loaded on CNFs, (b) CTS generated by CNFs, (c) HEA NPs in situ synthesized on the surface of CNFs, (d) schematic to show the structure of HEA NPs, and (e) the octonary HEA NPs with 8 elements. Reprinted with permission from ref 10. Copyright 2018 AAAS. (f) HEA NPs with 15 elements. Reprinted with permission from ref 106. Copyright 2021 Elsevier. (g) HEA NPs with 21 elements. Reprinted with permission under a Creative Commons CC BY License from ref 58. Copyright 2022 Oxford University Press. Both the scanning electron microscope (SEM) and energy dispersive X-ray detector (EDX) images are displayed in (e−g), while the high-angle annular dark field-scanning transmission electron microscope (HAADF-STEM) image of the NPs was shown in (e).

regimes and enabled the formation of crystalline solid-solution NPs. In other words, the ultrafast cooling process, quite literally, "freezes" the mixing state of the liquid particles, leading to the formation of HEA NPs (Figures 8c and 8d). So, via CTS, multicomponent NPs with desired chemistry (composition), size, and phase (solid solution or phase-separated) were successfully synthesized by controlling the parameters (substrate, temperature, shock duration, and heating/cooling rate). Unary to octonary NPs were synthesized in this work (Figure 8e).[10]

Inspired by this innovative work, many researchers have focused on the CTS synthesis of HEA NPs and provided many encouraging results in the controllable fabrication and application of HEA NPs.[29,61,107] First, CTS fabrication can greatly extend the elemental composition of HEA NPs. Usually, the formation of bulk alloys is guided by the Hume−Rothery alloying rule.[108] The compositions of alloys are limited to similar elements, i.e., elements with atomic size difference (δ) < 15%, similar structure, valences, and electronegativity. A small mixing enthalpy (ΔH_{mix}) of <37 meV (3.57 kJ/mol) is the safe upper limit for the uniform alloy.[109] A similar empirical rule guides the formation of multicomponent HEA NPs fabricated via conventional methods, such as wet chemistry,[110] ball-milling,[111] arc melting,[112] etc. The limitations include −15 kJ/mol < ΔH_{mix} < 5 kJ/mol, δ < 5%, and similar confinement.[109,113,114] Therefore, the composition of HEA NPs fabricated by conventional methods is restricted in a certain region. Fortunately, CTS motivates a nonequilibrium reaction due to its ultrahigh heating temperature and ultrafast thermal quenching process. It overcomes the restriction of immiscibility in selecting the

https://doi.org/10.1021/acsnano.4c12350
ACS Nano XXXX, XXX, XXX−XXX

elemental composition of HEA NPs.[115] Thus, a variety of elements have been incorporated together via CTS, including the AlCoCrCuFeNi,[61,116] FeNiCoCrMn,[29,32] noble alloy systems,[107,117] and their derivatives, e.g., high entropy metallic oxide (HEO)[32,118] and high entropy metallic carbide (HEC).[95] The number of mixed elements is progressively increasing. Yao et al. reported the successful synthesis of octonary HEA NPs (PtPdCoNiFeCuAuSn),[10] and they further mixed 15 elements (PtPdRhRuIrAuCuFeCoNiCrMnWMoSn) to form HEA NPs (Figure 8f).[106] Very recently, an ultramixed HEA NP system was realized by incorporating 21 elements (FeCoNiCrYTiV-CuAlNbMoTaWZnCdPbBiAgInMnSn) together (Figure 8g).[58] It is foreseeable that more elements will be mixed in HEA NPs via CTS.

Second, CTS can control the size of the as-synthesized HEA NPs. The duration of CTS and the heating/cooling rate greatly affect the size, distribution, and structure of the obtained HEA NPs. Narrow size distribution and uniform dispersion of HEA NPs were achieved across the carbon support by adjusting the key parameters of CTS and the defect level of the carbon support.[10] The size of HEA NPs increased with the increasing duration of CTS, and the decreasing cooling rate would cause the phase separation, aggregation, structural crystallinity, and nonuniform particle dispersion of the HEA NPs. In addition, the surface defects of the carbon support, especially the O* residuals, would drive the movement of liquid metal by O* harvesting and thus the fusion of liquid NPs to form single-phase alloys. So, the defect level and distribution would directly affect the size distribution and site dispersion of the formed HEA NPs. In another work, through the defect engineering of the carbon support and the optimization of precursor loading, the particle size of as-synthesized HEA NPs was robustly tuned from >50 nm to <1 nm with the increasing defects, and meanwhile, the dispersion density was greatly improved.[94] Song et al. revealed that except for O* residuals, the sp^3-hybridized C—C also helped to miniaturize the size of as-synthesized HEA NPs.[42] The high content of sp^3-hybridized C—C bonds contributed to the formation of the uniformly dispersed ultrasmall HEA NPs on the carbon supports and caused a high surface coverage.

Third, CTS can fulfill the structure-controlled synthesis of HEA and other NPs. By controlling the CTS parameters, especially the maximum temperature (T_{max}), Lu et al. synthesized interesting Janus homologous heteronanoparticles, in which transition metal (TM) alloys and transition metal sulfides (TMS) were sewed together to form the TM/TMS heterostructures (Figures 9a–d). Unary to quaternary TM/TMS NPs, e.g., Co/Co_9S_8, Fe/FeS, Ni/Ni_3S_2, $FeNi/(FeNi)_9S_8$, $FeCo/(FeCo)S$, $CoNi/(CoNi)_9S_8$, $FeCoNi/(FeCoNi)_9S_8$, and $FeCoNiCu/(FeCoNiCu)_9S_8$, were synthesized on the surface of CNFs by varying the component of precursors. The sulfuration and carbothermal reduction coexisted and competed with each other, which caused the formation of the Janus heterostructures at the proper temperatures. Taking Co/Co_9S_8 as an example, it formed in a moderate temperature range of 980–3600 K, and meanwhile, the proportion of Co increased with the rising temperature (Figure 9e). At temperatures of ≤980 K or >3600 K, only Co_9S_8 or Co existed, respectively. With this well-controlled Janus homologous heterostructure, this work provided an efficient method to modify the electrochemical performance of these TM/TMS NPs by tuning the active sites and their synergistic effect for oxygen reduction and evolution reactions (ORR and OER).

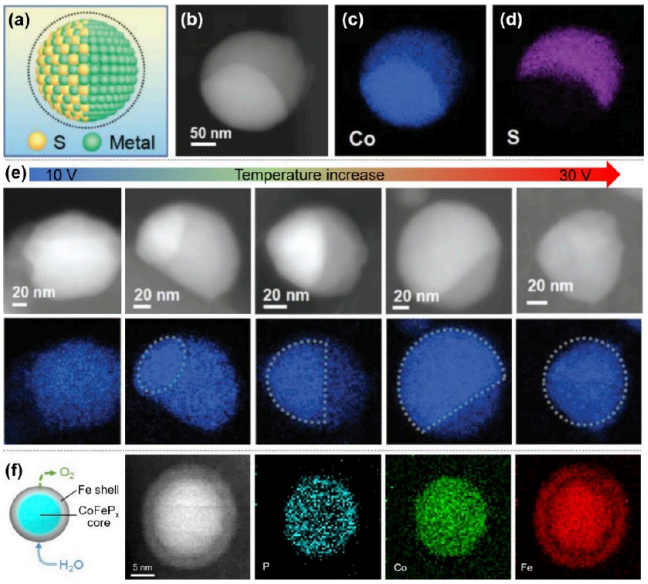

Figure 9. Structure-controlled synthesis of NPs via CTS. (a) Schematic of the Janus homologous heteronanoparticles, (b) morphology of the heteronanoparticles, (c, d) distribution of Co (c) and S (d) in the heteronanoparticles, and (e) temperature-controlled structural evolution of the nanoparticles. Reprinted with permission from ref 119. Copyright 2022 John Wiley and Sons. (f) Core–shell $CoFeP_x$-Fe nanoparticle, including its structure, morphology, and elemental distribution. Reprinted with permission from ref 120. Copyright 2019 Elsevier.

Utilizing the difference in the vapor pressures of Fe and Co at high temperatures, core–shell structured $CoFeP_x$-Fe nanoparticles were fabricated via CTS (Figure 9f).[120] Carbonized basswood with numerous vessel channels was used to generate CTS, and a current pulse was applied to the carbonized wood for 0.5 s to trigger the ultrashort CTS with maximum temperatures of 1200–1400 K. The ethanol solutions containing $Fe(NO_3)_3$, $Co(NO_3)_2$, and trioctylphosphine oxide were dispersed in the carbonized bass wood to serve as the precursors. At high temperatures, phosphorus atoms quickly bonded with the carbon matrix via oxygen displacement, and then Co and Fe solidified, alloyed, and bonded with the P atoms anchored on the carbon matrix to form metal phosphide nanoparticles. Since the vapor pressure of Fe is 4 times that of Co, partial Fe deposited more slowly than Co and thus coated on the surface of the preemptively agglomerated $CoFeP_x$ NPs to form the core–shell structure. The inner $CoFeP_x$ core possessed excellent activity toward OER, while the Fe shell (about 2 nm) protected the $CoFeP_x$ core and dramatically enhanced its stability without degrading the catalytic activity.[120]

All the research works mentioned above have identified the power of CTS in the controllable synthesis of NPs. It can effectively prevent the agglomerating and coarsening of formed NPs and guarantee good dispersity on the surface of carbon matrices.[121] Through the careful design of precursors (elementary composition and amount), carbon matrix (defect concentration), and key parameters of CTS (temperature, heating/cooling rate, duration, number of shocks, and pressure), it is very efficient to tune the composition, size, structure, and distributions of the as-synthesized NPs via CTS and thus modify their properties according to the requirements of different applications. In other words, CTS can implement the customized preparation of NPs for specific applications, such

https://doi.org/10.1021/acsnano.4c12350
ACS Nano XXXX, XXX, XXX–XXX

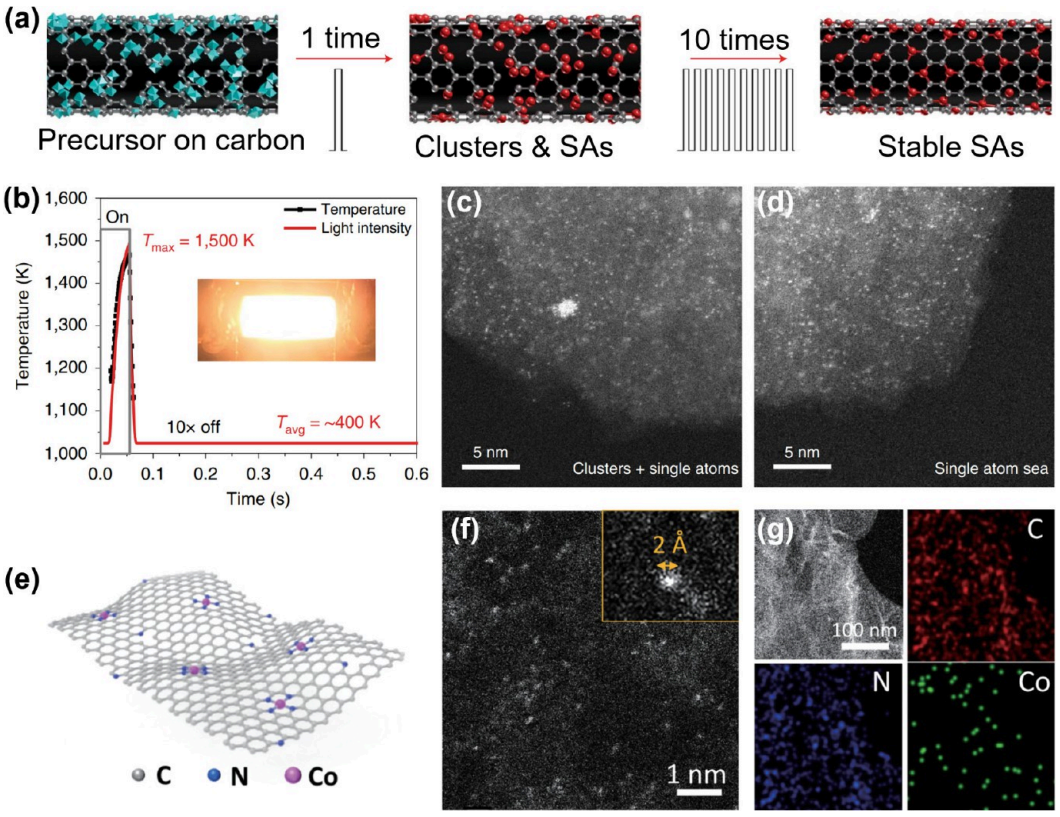

Figure 10. Synthesis of SAs via CTS. (a) Schematic to show the synthesis process and the structure of the CNF-supported SAs, (b) temperature profile of the CTS process, while the inset picture shows the light-emitting CNF film which has been heated up to 1500 K, (c) morphology of the cluster + SAs and (d) pure SAs synthesized with one and ten thermal shocks, respectively. Reprinted with permission from ref 30. Copyright 2019 Springer Nature. (e) Schematic to show the atomic CoN_x moieties supported on the graphene, (f) morphology of the CoN_x moieties, and (g) elemental composition analysis of the CoN_x moieties. Reprinted with permission from ref 138. Copyright 2022 Springer Nature.

as ORR,[122] OER,[123] hydrogen evolution reaction (HER),[124] CO_2RR,[125] photothermal therapy,[126] etc. These superiorities will encourage the intense research of the CTS synthesis of functional NPs and bring it into real applications.

3.2.1.2. Single Atom (SA). SA has become one of the most popular research frontiers and attracted lots of attention in fields of heterogeneous catalysis,[127] energy storage and conversion,[128] environmental remediation,[129] biosensing and biomedicine,[130] etc. The controlled synthesis of SAs is the first and foremost prerequisite to delve into these applications. Recently, CTS has shown its competence in the controlled fabrication of SAs.[131−134] Compared to the wet chemistry methods (e.g., sol−gel and ion-exchange),[135] thermochemical methods,[136] and electrochemical methods,[137] CTS can realize the ultrafast synthesis of various SAs and the control over the density and distribution of formed SAs. Meanwhile, it can prevent the isolated SAs from thermodynamically spontaneous agglomeration and thus stabilize the formed SAs. So, CTS will accelerate the research and application processes of SAs.

As reported by Yao et al.,[30] Pt SAs were in situ decorated on the surface of CNF via CTS with the salt precursor (H_2PtCl_6) (Figure 10a). The temperature of the periodic on−off heating was controlled at 1500−2000 K, and the duration of the on-state was 55 ms while the off-state was 550 ms (Figure 10b). CTS disassembled the Pt clusters, and just after one thermal shock, high-density SAs together with Pt nanoclusters were observed on the surface of CNFs, as shown by the HAADF-STEM images (Figure 10c). The amount of SAs increased with the increasing number of thermal shocks. Almost only SAs existed and were distributed uniformly on the CNFs after ten shocks (Figure 10d). This evolution was further confirmed by the macroscopic extended X-ray absorption fine structure (EXAFS) characterization. Both the Pt−Pt bond (Pt cluster) and Pt−C bond (Pt SA) were observed after one thermal shock, while almost only Pt−C bonds existed after 10 thermal shocks. The high temperature and short shockwave heating were necessary for forming SAs. Generally speaking, the high temperature provided the activation energy to disperse Pt atoms and bond them with the carbon matrix, while shockwave heating prevented the long-range diffusion and agglomeration of these atoms. Besides, the defects in CNF were also crucial for the formation of SAs as they bound the mobile single atoms onto the carbon matrix. So, high-density SAs formed on the surface of CO_2-activated CNFs with improved defect concentration and the presence of micropores (i.e., carbon vacancies). Moreover, the covalent Pt−C bond between SAs and CNFs endowed these SAs with high structural stability. Pt SAs and Pt−C bonds survived from harsh conditions, e.g., a long-time high-temperature condition of 1273 K. So, these CTS-synthesized SAs supported on conductive CNFs are very favorable for catalyst applications like CO oxidation and methane conversion in which high temperature exists.

CTS has been proved to be a facile and universal method for the synthesis of different SAs (e.g., Pt, Co, and Ru) on different substrates (e.g., CNF, rGO, C_3N_4, and TiO_2) by changing the precursors and heating method (current or microwave irradiation).[30] Except for these monoplasmatic SAs, Xing et al. also reported the synthesis of atomic CoN_x moieties in the

https://doi.org/10.1021/acsnano.4c12350
ACS Nano XXXX, XXX, XXX−XXX

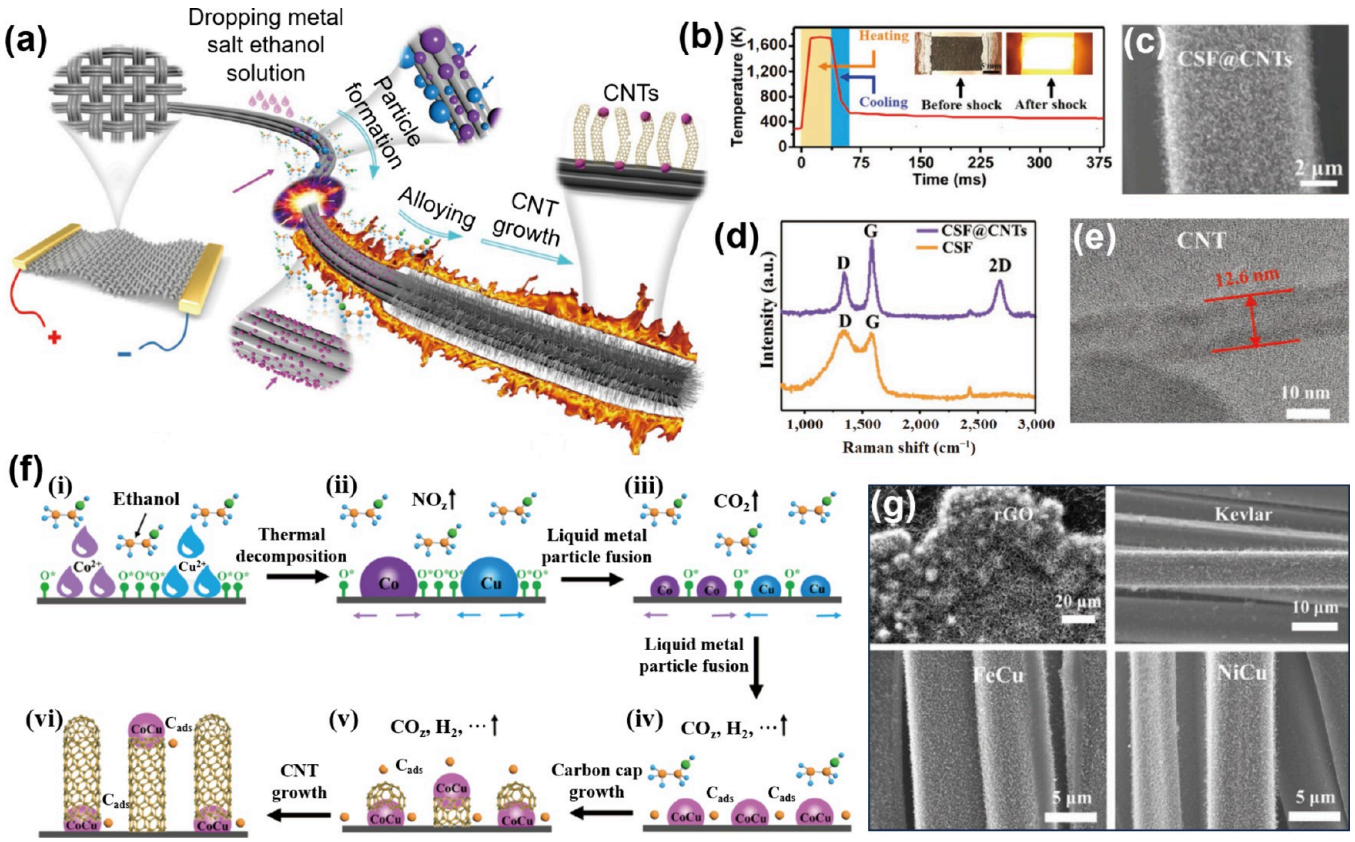

Figure 11. Synthesis of 1D CNT via CTS. (a) Schematic to show the growth process, (b) temperature profile of the CTS, (c) the fluffy morphology of the CNT-covered CSF after the growth, (d) Raman spectra of the original CSF and the CNT-covered CSF, (e) TEM image of the as-grown CNT, (f) schematic illustration of the growth mechanism, and (g) CNTs grown on different carbon matrix and with different catalysts. Reprinted with permission from ref 17. Copyright 2022 Springer Nature.

graphene matrix.[138] Within the 2-s CTS process, nitrogen and cobalt atoms were codecorated into graphene at the defective sites (Figure 10e). Co and N atoms were uniformly distributed throughout the graphene flake, as depicted in Figures 10f and 10g. Further, the XPS characterization confirmed the bond between Co and N by the deconvoluted peak, which arose from N−Co/pyridinic N at 398.5 eV. These highly active CoN_x moieties made the hierarchically porous graphene-based Co−N−C single-atom monoliths a good electrode for the hydrogen evolution reaction.

The CTS-synthesis technique of SAs is developing rapidly. Researchers have an initial understanding of its kinetics and mechanism. However, the synthesis process of SAs is similar to that of the aforementioned NPs. The key parameters that determine the form of the product, i.e., NP or SA, need to be ascertained. Besides, only monocompositional SAs were synthesized in the works mentioned above. To extend the functionality of SAs, the technique to synthesize bi- or even multicompositional SAs should be developed. Moreover, the map to show the effect of the composition, concentration, and distribution density on the performances of SAs should be drawn to guide the CTS synthesis of SAs supported on carbon matrices. All these efforts will dramatically improve the serviceability of CTS-synthesized SAs in different areas, such as catalysis, environmental remediation, biosensing, and biomedicine.

3.2.2. Growth of 1D CNT. CTS generated by carbon materials can, in turn, serve as the energy motivation to activate the growth of CNTs. Wang et al. reported the ultrafast CTS growth of CNTs on the surface of carbonized silk fabric (CSF) within just one second (Figure 11a).[17] The mixed ethanol solution of two nitrate salts, e.g., $Co(NO_3)_2$-$Cu(NO_3)_2$, $Fe(NO_3)_3$-$Cu(NO_3)_2$, or $Ni(NO_3)_2$-$Cu(NO_3)_2$, was loaded on the heating element of CSF to catalyze the growth CNTs and provide the carbon source. As shown in Figures 11b−e, fluffy CNTs (12.6 nm in diameter and 1.5 μm in length) were grown on the surface of CSF fibers when the CSF was heated up to 1700 K at a ramp rate of 10^5 K/s with the pulse voltage input (40 V for 50 ms). During this process, the applied voltage, i.e., the heating temperature, rather than the duration of thermal shock, controlled the formation of CNTs. As revealed by the authors, liquid alloy catalyst droplets formed from the nitrate salts only when the input voltage was high enough (40 V) to generate a high temperature (1700 K). CO_2 gas released from the CSF surface and generated by the carbon metabolism reaction drove the quick move and split of the liquid alloy droplets to form the uniformly distributed catalytic NPs. Then, with the absorption of carbon fragments formed from the pyrolysis of ethanol, CNTs were catalytically grown with a high efficiency and at a high speed (Figure 11f). The whole CTS growth was completed in 50 ms or less. Following this strategy, CNTs were grown on different carbon matrixes and with different catalysts (Figure 11g). All these results showed CTS's high efficiency and feasibility in the growth of CNTs.[17]

Interestingly, another work reported that CNTs can be synthesized using high-entropy oxide (HEO) as the catalyst to form the HEO−CNT nanocomposite and the reduced nanocomposite (rHEO−CNT).[139] The authors found that HEO

https://doi.org/10.1021/acsnano.4c12350
ACS Nano XXXX, XXX, XXX−XXX

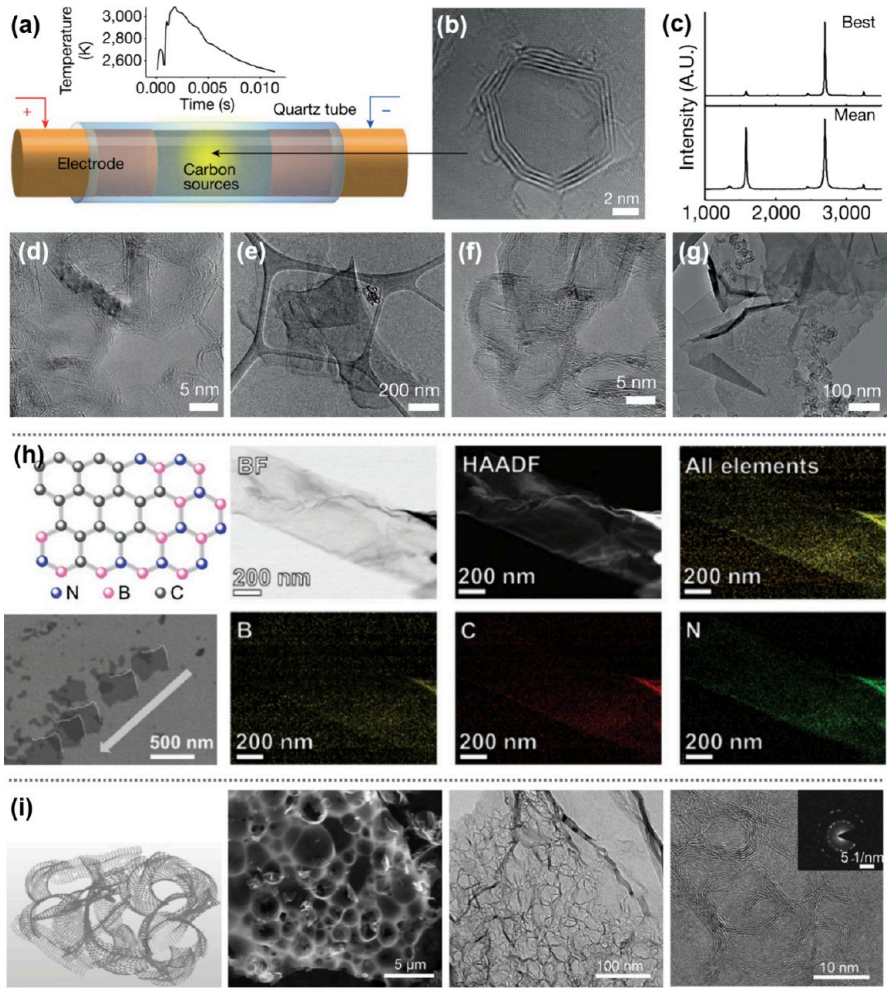

Figure 12. CTS synthesis of 2D materials. (a) Schematic to show the growth setup of FG, (b) HR-TEM of the coffee-derived FG, (c) Raman spectra of the coffee-derived graphene, (d–f) morphologies of FG derived from carbon black (d), anthracite coal (e), calcined coke (f), and coffee (g). Reprinted with permission from ref 143. Copyright 2020 Springer Nature. (h) BCN, its structural schematic, morphology, and elemental distribution shown by BF-STEM, HAADF-STEM, and EDS images, and the exfoliated BCN grown via CTS. Reprinted with permission from ref 144. Copyright 2022 American Chemical Society. (i) Porous graphene, its structural schematic, and its morphology and structure shown by the SEM and TEM images. Reprinted with permission from ref 145. Copyright 2023 John Wiley and Sons.

nanoparticles showed high catalytic efficiency. An unexpectedly high yield of CNT was achieved. With the use of 100 mg of HEO nanoparticle, 1.5 g of rHEO−CNT or 1.2 g of HEO−CNT nanocomposites were produced with or without H_2 gas as the reductant. The HEO NPs can also act as the electrochemistry catalyst when the HEO−CNT or rHEO−CNT nanocomposite is used in different electrochemical reactions. The HEO NPs were well encapsulated inside the as-grown CNTs, making them quite stable in electrochemical reactions. So, combining the high electrical conductivity, high surface area, good mechanical stability, and excellent electrochemical redox activity, the HEO−CNT nanocomposite showed great potential in the application of electrochemical capacitors.[139] Unfortunately, the HEO NPs were fabricated by using the sol−gel autocombustion technique while the CNTs were grown through a conventional furnace CVD process in this work. The synthesis process involved many complicated steps and was highly time- and energy-consuming. As mentioned above, both the HEO and CNT can be synthesized via CTS. So, by taking advantage of CTS, CNTs can be ultrafast synthesized in one pot through sequential operations, i.e., loading of catalyst precursors—CTS synthesis of HEO—injection of carbon source—CTS growth of CNTs, and the mass production can be achieved by repeating the growth sequence.

These works have demonstrated the efficacy of CTS in synthesizing 1D materials. However, only CNT has been successfully grown via CTS. It figuratively forms an interesting "from carbon to carbonene" growth route. Next, intense studies are needed to go beyond the "from carbon to carbonene" growth and realize the CTS synthesis of other 1D materials. A thorough study is in urgent demand to comprehend the reaction kinetics and growth mechanism behind this ultrafast synthesis process. Meanwhile, more works are needed to extract the key growth parameters that determine the growth result, and strict regulation on the extracted parameters will enhance control over the dimensions of synthesized 1D materials, e.g., diameter, length, wall number, and wall thickness.

3.2.3. Growth of 2D Materials. The controllable synthesis of 2D materials has been intensely studied in the past several years, which will lay the solid foundation for their application as structural and functional materials in electronic, optoelectronic, catalytic, and energy devices. Now, CTS has provided an ultrafast route to synthesize 2D materials with special structures,

https://doi.org/10.1021/acsnano.4c12350
ACS Nano XXXX, XXX, XXX−XXX

such as porous, cage-like, and flat graphene, from low-cost precursors or even wastes.

Recently, CTS has been intensely employed in synthesizing high-quality graphene film by conducting current through the metal substrates, and mass production has been achieved through a roll-to-roll method.[140−142] The application of CTS also facilitates the ultrafast growth of graphene powder and framework (the products are usually called flash graphene, FG). For example, using CTS, Luong et al. synthesized high-quality FG on the gram scale from low-cost carbon sources, such as coal, petroleum coke, biochar, carbon black, discarded food, rubber tires, and mixed plastic wastes.[143] The growth setup is shown in Figure 12a. Amorphous conductive carbon powder was loosely condensed in a quartz or ceramic tube by two electrodes made of copper, graphite, or other conductive refractory material. A capacitor bank was used to generate high-voltage electric discharges to heat the carbon source to 3000 K within 100 ms. During this short process, the carbon black was converted to turbostratic FG (Figure 12b). Raman characterization demonstrated that the product from carbon black had an intense 2D peak and extremely low D band, and the intensity ratio of 2D and G bands (I_{2D}/I_G) reached 17 (Figure 12c). The X-ray diffraction pattern showed a well-defined (002) peak at the diffraction angle 2θ = 26.1°. Meanwhile, the high-resolution transmission electron microscopy (HR-TEM) showed the highly crystalline feature of the as-obtained FG, in which the turbostratic structure with an average size of 13 nm was observed. All these characterization results demonstrated that high-quality FG was successfully synthesized during the short CTS-activated reaction process (reaction time <1 s).

Other precursors, including coffee, charcoal, biochar, humic acid, keratin (human hair), lignin, sucrose, starch, pine bark, olive oil soot, cabbage, coconut, pistachio shells, potato skins, rubber tires, mixed plastic, polyethylene terephthalate (PET or PETE), high- or low-density polyethylene, polyvinyl chloride, polypropylene, and polyacrylonitrile, were also converted into FG. However, the microstructures of the FGs obtained from different precursors were quite different (Figures 12d−g). For example, the carbon-black-generated FG showed a porous structure with a surface area of about 295 m^2/g and a pore size of <9 nm (Figure 12d). Similar results were observed in calcined petroleum-generated FG, whose average size increased to about 17 nm (Figure 12f). In contrast, anthracite coal and coffee were converted into folded FG sheets with average sizes of 0.5 and 1.2 μm (Figure 12e and 12g), respectively. And the product was a mixture of monolayer and turbostratic FGs. Ignoring this difference, CTS provides a universal method to fabricate FGs. More importantly, Luong et al. realized the gram-scale production of FG in less than one second. The yield was high, about 80% to 90%, depending on the precursors' carbon content. The electric energy cost for this CTS conversion was about 7.2 kJ/g, much lower than that of conventional CVD synthesis. So, it provides a practical method to realize the mass production of high-quality graphene with low cost and low energy consumption via CTS.

Inspired by this work, graphene was produced from various low-cost or even waste materials, such as rubber and various plastic waste.[25,146−152] However, the precursor type, composition, structure, and the CTS parameters greatly affect the morphology and elemental composition of the products. Though some works demonstrate that the high temperature generated during the CTS process fully removed the noncarbon atoms (e.g., hydrogen, oxygen, chloride, and nitrogen) from the precursors, e.g., poly(vinyl chloride), to produce intrinsic FG,[148,151] flash nitrogen-doped graphene (FNG) was synthesized via CTS by using the mixture of carbon black and urea as the precursor (Figure 12h).[144] More heteroatom-doped FGs were synthesized via CTS with different dopants.[153] Single-element-doped FG (boron, nitrogen, oxygen, phosphorus, sulfur), two-element-*co*-doped FG (boron and nitrogen), and three-element-*co*-doped FG (boron, nitrogen, and sulfur) were successfully synthesized by using elements (M), oxides (MO_x), or organic compounds (C_xH_yM) as the dopants. Compared to the intrinsic FG, these heteroatom-doped FGs not only had similar good quality, expanded interlayer spacing, and superior dispersibility but also showed greatly improved electrochemical performances, especially for the sulfur-doped FG.[153]

Except for the elemental composition and atomic structure, the microstructure of the as-synthesized graphene can also be modified via CTS. For example, Zhou et al. successfully synthesized porous graphene frameworks (Figure 12i).[145] To realize this, sucrose and zinc nitrate hexahydrate were mixed and reacted at 180 °C in air to generate porous carbon. Then, the product was annealed at 750 °C in a tube furnace with the protection of Ar gas. At this point, porous carbon was produced with quite low crystallinity. After being immersed in the dilute hydrochloric acid to remove ZnO, the porous carbon was loaded in a quartz tube to perform the CTS treatment with different discharging voltages. A short thermal shock with a duration of 300−1000 ms fully converted the amorphous porous carbon into highly crystalline porous FG. The crystallinity was well controlled by tuning the duration of CTS. Both micro- and mesopores existed in the as-synthesized porous FG with a specific surface area of 503 m^2/g, while nanopores ruptured during the short CTS process. The synthesized porous graphene showed superior electrical conductivity, which will facilitate the formation of the conductive network when being added to composite materials with a low filling content. The high electrical conductivity, porous structure, and tunable defect level made this porous graphene a good candidate for electromagnetic wave absorption.

In short, CTS provides a simple, low-cost, ultrafast, and environmentally friendly method to convert different carbon-rich materials into graphene. It is easy to realize the mass production of graphene, and the energy consumption was quite low, in the range of 1.2−23 kJ/g for CTS,[153,154] while the energy consumption is at a high level of 500−1640 kJ/g for the graphene powder exfoliated through the conventional Hummers method and 1.7−199 kJ/cm^2 for the CVD-grown graphene film.[155−157] Besides, CTS can convert low-cost material or even waste into graphene, which will help to dispose waste materials and upcycle the value of wastes. It not only echoes the concept of green manufacturing but also provides significant economic advantages and environmental benefits to fulfill a circular economy. For the CTS synthesis of other nanomaterials, e.g., HEA NPs, SA, and CNTs, although there are no quantitative reliable data to illustrate the mass production ability and energy consumption, the production can be easily scaled up, and the energy consumption must be kept at a low level owing to the ultrafast synthesis process, the localized in situ heating mode, and the high heating efficiency of carbon heating elements. So, it is foreseeable that CTS will find its wide application in the mass production of nanomaterials. At present, the CTS synthesis technique is still in its infancy. More efforts are needed to address the ambiguity and uncertainty in the kinetics of and the growth mechanisms behind the ultrafast high-temperature

https://doi.org/10.1021/acsnano.4c12350
ACS Nano XXXX, XXX, XXX−XXX

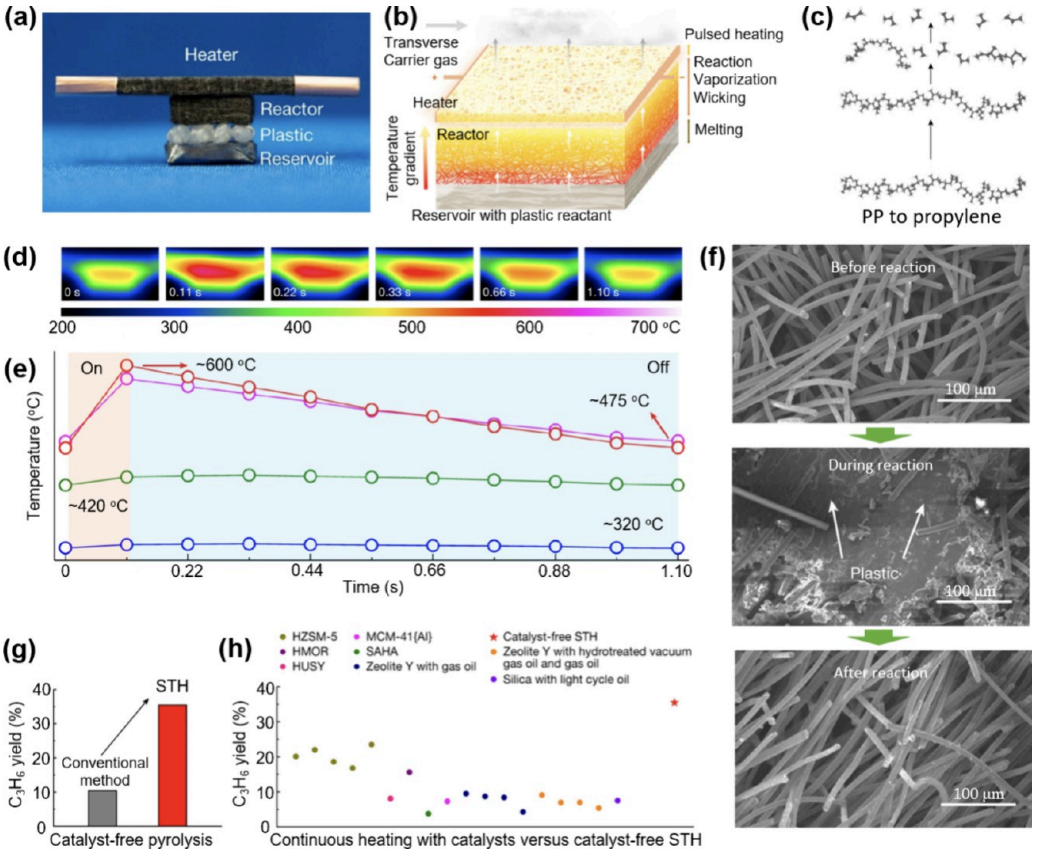

Figure 13. Depolymerization of plastics via CTS. (a) The whole setup for the CTS-triggered depolymerization of plastics, (b) schematic to show the process and mechanism of the CTS-triggered depolymerization, (c) schematic to show the depolymerization process of PP, (d) temperature maps to show the temperature gradient and evolution of the heater and reactor layers, (e) temporal temperature profiles recorded at four representative regions to show the temperature evolution process, (f) SEM images to show the wicking and vaporization process of PP, (g) comparison of the C_3H_6 monomer yield between the CTS-triggered depolymerization and conventional catalyst-free pyrolysis, and (h) comparison of the C_3H_6 monomer yield between CTS-triggered depolymerization and other methods with the utilization of different catalysts, reaction media and processes. Reprinted with permission from ref 177. Copyright 2023 Springer Nature.

reactions to further improve the controllability over the CTS synthesis of nanomaterials, e.g., to realize the composition/size-controlled synthesis of HEA NPs or the diameter/chirality-controlled synthesis of single-walled CNTs.

3.3. Sustainable Management of Solid Waste. With the rising income, population, urbanization, and industrialization, a lot of municipal solid waste (MSW) is generated every day.[158,159] 1.9−2.01 billion tons of MSW is produced worldwide per annum, and the amount is expected to increase to the range of 3.04−5.09 billion by 2050.[160−162] Most of these MSW is progressively concentrated in metropolitan areas. A conservative estimate, more than 33% of the MSW is not handled in an ecologically sustainable method.[163] The huge amount of MSW is causing great economic losses and drastically impacting the environment and human health.[164] The sustainable management of MSW has become one of the urgent world-class problems to be solved. The emergence of the CTS technique provides several alternative approaches to realize the sustainable treatment of MSW (e.g., plastic and rubber) and many other wastes (e.g., biomedical and agricultural wastes).

3.3.1. Upcycling of Plastic and Other Carbonaceous Wastes. As mentioned above, the ultrahigh heating temperature and ultrafast heating/cooling rate endow CTS with the ability to convert different carbonaceous wastes into FG with a surprisingly low level of energy consumption.[143] Following this strategy, various carbonaceous wastes, including plastic, rubber, asphaltenes, and biomasses, can be upcycled in an eco-friendly way.[146,148−151,165−168] The concrete implementing method has been introduced in Section 3.2.3, and nano- or microscale FG with different morphologies can be obtained within only several shocks. Except for these waste materials, other carbonaceous materials, such as leaves, wood wastes, vegetable wastes, rice husks, papers, and textiles, can also be converted into FG. The gross amount of carbon in solid wastes now has exceeded 1300 Mt and is expected to be over 2100 Mt (2.1×10^{12} kg) in 2050.[169] CTS has the power to fulfill the waste valorization by upcycling these solid wastes into high-valued FG, and meanwhile, it can avoid the shortcomings of the conventional waste disposal methods, e.g., landfilling, open dumping, incineration, and pyrolysis. For example, landfilling and open dumping occupy many territories and seriously pollute the environment because many kinds of contaminants are released, including but certainly not limited to greenhouse gases, hazardous gaseous pollutants, volatile organic compounds, and toxic leachate.[170−173] For incineration, though it can significantly reduce the mass and volume of waste by 70−80% and 80−90%, respectively, and thus ease land scarcity, it generates a lot of polluting gases, including SO_x, NO_x, CO_x, and polyaromatic hydrocarbon.[170,174,175]

It is ecologically and economically beneficial to upcycle solid waste into high-valued FG via CTS. Jia et al. have pointed out that this upcycling method can greatly decrease the overall life-

https://doi.org/10.1021/acsnano.4c12350
ACS Nano XXXX, XXX, XXX−XXX

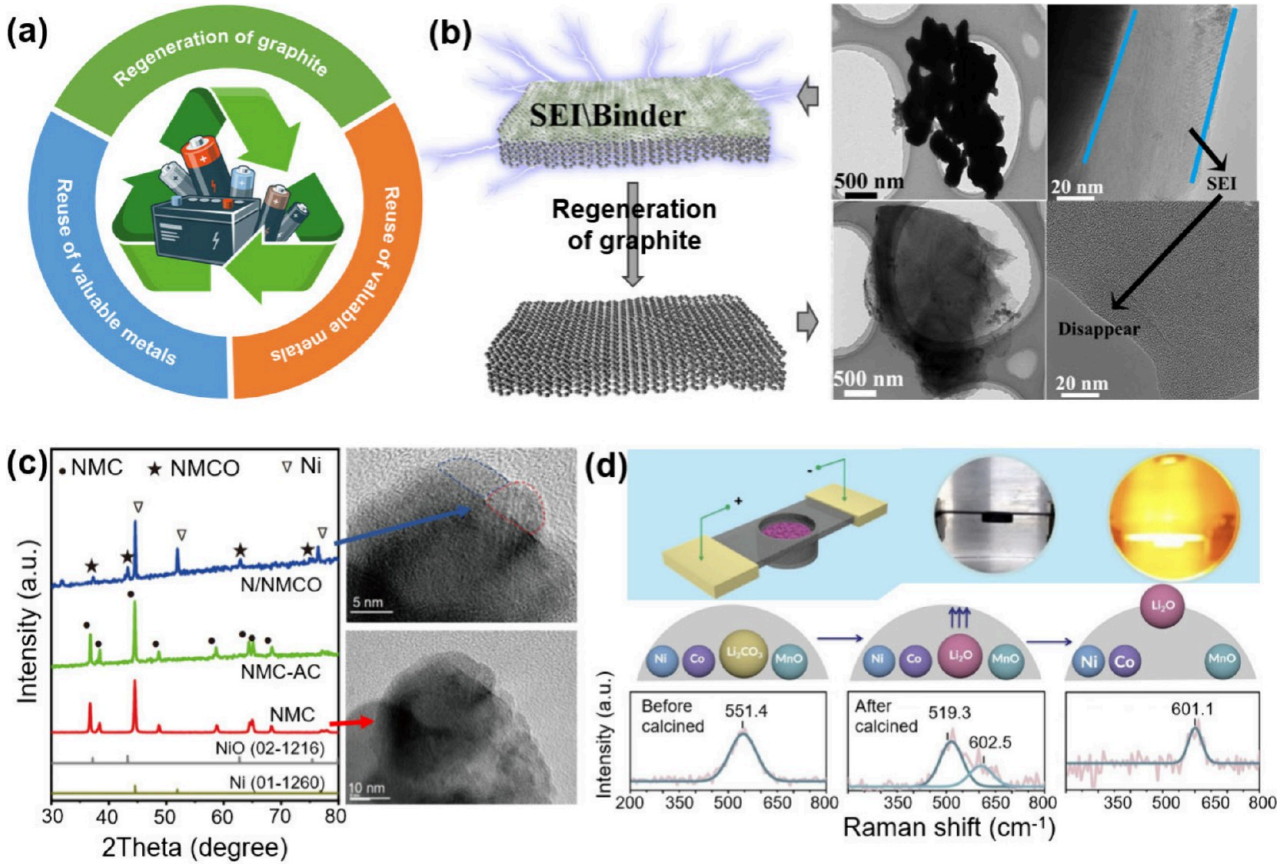

Figure 14. Recycling of LIBs. (a) Schematic to summarize the recycling strategies. (b) Regeneration of spent graphite anode, during which the spent thick graphite was converted into thin graphite, and the SEI layer was removed. Reprinted with permission under a Creative Commons CC BY 4.0 License from ref 178. Copyright 2022 John Wiley and Sons. (c) Reuse of valuable metals. The spent cathode NMC was turned into catalytically active Ni/Ni-MnCo-O composites. Reprinted with permission from ref 180. Copyright 2022 Springer Nature. (d) The extraction of valuable metals from the spent cathodes. NCM was reduced to Li_2O, Co, Ni, and MnO by CTS, and then these metals were leached by water and dilute acid to fulfill the high-efficiency recycling. Reprinted with permission from ref 181. Copyright 2023 John Wiley and Sons.

cycle environmental impacts by more than 10 folds compared to the conventional approaches.[167] To be specific, the climate change impact based on the production of 1 g graphene from the four biomass feedstocks, i.e., sawdust, wheat, straw, corn straw, and rice straw, calculated through the ReCiPe 2008 method is only in the range of 2.73−11.5 g CO_2e per g for CTS-synthesized FG. But for other graphene fabrication methods, the climate change impact falls in the range of 49−407 g CO_2e at the lab scale and 28−407 g CO_2e at the commercial scale, respectively. The fossil depletion impact is about 1.81−3.97 g oil-eq, while it is at a high level of 43.8−102 g oil-eq for the traditional technologies at the lab scale. Other impacts, including terrestrial acidification impact, metal depletion, and particulate matter formation, are also at a low level, all less than 10% of that of the traditional graphene fabrication methods. In another work, Wyss et al. demonstrate that the cumulative energy demand (CED), the global warming potential (GWP), and the cumulative water use (CWU) needed to upcycle vehicle waste plastic into FG via CTS reduce by 88%, 85%, and 93%, respectively, in comparison with the ultrasonication synthetic method of graphene. Compared to the chemical exfoliation method, CTS also affords an 80%, 80%, and 97% reductions in CED, GWP, and CWU, respectively.[176]

Recently, Prof. Hu's team proposed another breakthrough route to recycle plastic waste via CTS, i.e., to depolymerize plastics into constituent monomers for subsequent repolymerization.[177] Figure 13a shows the whole setup, while Figures 13b and 13c schematically depict the process and mechanism of the CTS-triggered depolymerization of plastics. A porous bilayer carbon felt is set above and in contact with the solid plastic reactant (Figure 13a). The top layer serves as the heating element, while the bottom layer acts as the reactor layer. When a pulsed electrical current is applied to the top heater layer, the Joule heat will be generated and conducted from the top layer to the bottom reactor layer and then to the underlying plastic reactant (Figure 13b). The plastic then will melt and decompose continuously at sufficiently high temperatures as the molten plastic can wick upward inside the porous carbon felt with the driven capillary force. Figure 13c schematically shows the depolymerization of polypropylene (PP) into propylene. To be specific, the evolution of the spatial temperature gradient generated by a pulse voltage (22 V for 0.11 s and 0 V for 0.99 s) is exhibited in Figure 13d. The temporal temperature profiles were recorded at four different regions, including the interfacial region between the heater reactor layers (red trace) as well as the top, middle, and bottom sections of the reactor layer (pink, green, and blue traces, respectively), as shown in Figure 13e. The temperature gradient ranges from 475−600 °C at the interfacial region to about 320 °C at the bottom section of the reactor layer. And the maximum heating temperature recorded at the interfacial region evolves from about 475 to 600 °C when the current is turned on and then back to 475 °C.

https://doi.org/10.1021/acsnano.4c12350
ACS Nano XXXX, XXX, XXX−XXX

The vertically distributed spatial temperature gradient and the periodic high peak temperatures are critical for the continuous melting, wicking, vaporization, and reaction of the underlying plastic. They enable a high degree of depolymerization and suppress unwanted side reactions. So, a high C_3H_6 monomer yield of 35.5% ± 6.2% for PP is achieved without further optimization. As shown in Figures 13g and 13h, this yield is much higher than other catalyst-free pyrolysis methods and even many optimized with-catalyst methods. For poly(ethylene terephthalate) (PET), this CTS-triggered depolymerization can also give a high monomer yield of 43%. Next, with the introduction of catalysts and the further modification of the material properties of the reactor layer (e.g., pore shape, pore size and distribution, and surface energy) and the heating program (e.g., heating duration, frequency, maximum temperature, and temperature distribution), the product yield can be further improved, and meanwhile, the energy cost can be further reduced. When moving beyond the proof-of-concept demonstrations, this CTS-triggered depolymerization strategy holds great potential for converting many solid wastes, including plastics, biomass, and other supramolecules, to their monomers for the next sustainable and energy-efficient manufacturing of value-added chemicals.

3.3.2. Recycling of Li-Ion Battery. With the wide-scale use of Li-ion batteries (LIBs), lots of batteries have been scrapped now and there will be more spent batteries in the future. It has become a world-class problem to recycle and reuse these dead Li-ion batteries efficiently with low power consumption, low time consumption, and high environmental friendliness. CTS has show great potential in this area and will be a vital force to recycle and reuse the carbon electrode and valuable metals, as schematically shown in Figure 14a. As reported by S. Dong et al., the binder and solid electrolyte interphases (e.g., LiF and Li_2CO_3) in the graphite anode were removed by thermal decomposition or volatilization after being treated by CTS.[178] Meanwhile, the high-temperature CTS converted the spent graphite into flash graphite (F-RG) with a reconstructed structure, reduced impurity, and larger surface area (Figure 14b). The regenerated F-RG recovers the multiplier and cycle performance or even shows higher performance. The energy and energy consumption are quite low to recycle the spent graphite anode in this way, which is at the level of 112 kJ/g and 77 CNY/ton. This work highlights a promising CTS method to recycle spent graphite anodes and reuse them in LIBs. In another work, Luo et al. confirmed that the regenerated defect-rich graphite has a high charging specific capacity of 323 mAh/g, outperforming commercial graphite with a charging specific capacity of 120 mAh/g.[179] Zeng et al. reported that the supercapacitor made of porous carbon electrodes recycled by CTS has a high energy density of 35 Wh/kg and a high power density of 875 W/kg in $EMIMBF_4$ ionic liquid. These results demonstrate that CTS-triggered recycling will not only help to solve the problem of environmental pollution and relieve environmental stress caused by spent LIBs but also create greatly improved economic benefits owing to the high application value of regenerated products.

For the valuable metals, two different strategies are used to recycle them from the spent cathodes or anodes via CTS. The first is to convert the metals into catalytically active materials and reuse them in other electrochemical applications. As reported by Zheng et al., the spent cathodes ($LiNi_{0.8}Mn_{0.1}Co_{0.1}O_2$, NMC for short) were turned into Ni/Ni-MnCo-O (N/NMCO) via CTS.[180] The regenerated composite exhibits a high catalytic activity and can be directly used in oxygen evolution, oxygen reduction, hydrogen evolution reactions, and Zn-air batteries. To realize this, the spent cathodes were loaded onto a carbon cloth to perform the CTS treatment, i.e., heated up to 750 °C for 1−2 s at a heating/cooling rate of 10^4−10^5 K/s. During this process, part of the metastable Ni^{3+}/Ni^{4+} ions in the spent NMC were reduced to zerovalent Ni NPs while the other part of Ni^{3+}/Ni^{4+}, Co^{3+}/Co^{4+}, and Mn^{4+} cations became their respective oxides, and hence the N/NMCO composite formed after the short CTS treatment (Figure 14c). Significantly, the quick thermal shock not only lowered the power consumption but also facilitated the formation of NPs and the coexistence of mixed transition metal oxides. All these beneficial structural and componential features made the regenerated N/NMCO nanocomposite highly catalytically active in HER, ORR, OER, and Zn-air battery, surpassing the performance of conventionally used Ir/C, Pt/C, etc.[180] Moreover, as reported by other works, the rapid calcination realized by CTS can lower the concentration of surface oxygen vacancies, reduce the content of Mn^{3+}, and suppress the formation of surface reconstruction layers in the synthesized $LiNi_{0.5-x}Mn_{1.5+x}O_4$ cathode,[182] and the ultrafast nonequilibrium high-temperature shock can introduce Li−Fe antisite defects and tensile strain field into the lattice of $LiFePO_4$ cathode, which will create more diffusion channels and promote the isotropic two-dimensional interchannel Li^+ hopping toward better charging performance and cycling stability in LIBs.[183] So, CTS has become a powerful method to recycle and reuse spent batteries, especially in the regeneration of electrode materials.[184]

The second strategy is to extract valuable metals from the LIB cathodes. Taking the spent $LiNi_{0.3}Mn_{0.5}Co_{0.2}O_2$ (NCM352) cathode as an example, after being CTS treated at 2200 °C for 20 s in the argon atmosphere, it decomposed and reduced to Li_2O, Co, Ni, and MnO.[181] Then, Li was selectively water-leached with an efficiency of >90% (Figure 14d). Other metals, i.e., Co, Ni, and MnO, were subsequently recycled through dilute acid leaching with efficiencies of >98%. For this recycle strategy, the temperature and duration of CTS are very important to improve the leaching efficiency. NCM325 was fully reduced to Li_2O, Co, Ni, and MnO only when the applied current reached 180 A (∼2100 °C) for 30 s or 200 A (∼2200 °C) for 20 s. However, higher CTS temperatures (>2200 °C) caused the evaporation of Li and the encapsulation of Li or Li_2O in the calcined products, which lowered the leaching efficiency. The authors have confirmed that with optimal parameters, CTS can recycle various spent Li-ion batteries, including NCM111, $LiNi_{0.5}Co_{0.2}Mn_{0.3}O_2$, $LiNi_{0.6}Co_{0.2}Mn_{0.2}O_2$, $LiNi_{0.8}Co_{0.1}Mn_{0.1}O_2$, $LiCoO_2$ (LCO), and $LiMn_2O_4$ with high leaching efficiencies.[181]

Recently, many works have recycled or reused Li-ion batteries via CTS and confirmed the superiority of this strategy.[185,186] Interestingly, to recycle valuable metal, the graphite anode can be directly used as the heating element to generate CTS, further improving resource utilization and reducing the cost of treating dead batteries.[185] Overall, the use of CTS in the regeneration and recycling of Li-ion batteries can lower energy and time consumption, simplify operation steps, improve efficiency, and reduce pollution as well as greenhouse gas emissions. As estimated by Chen et al., the water consumption, energy consumption, and greenhouse gas emission to produce 1 kg CTS-recycled graphite anode are 20.06 L, 14.3 MJ, and 1.85 kg, respectively. All these values are lower than that of natural graphite from mined ore (105.94 L, 35.34 MJ, and 4.9 kg), synthetic graphite prepared from hard coal and crude oil (247.55

https://doi.org/10.1021/acsnano.4c12350
ACS Nano XXXX, XXX, XXX−XXX

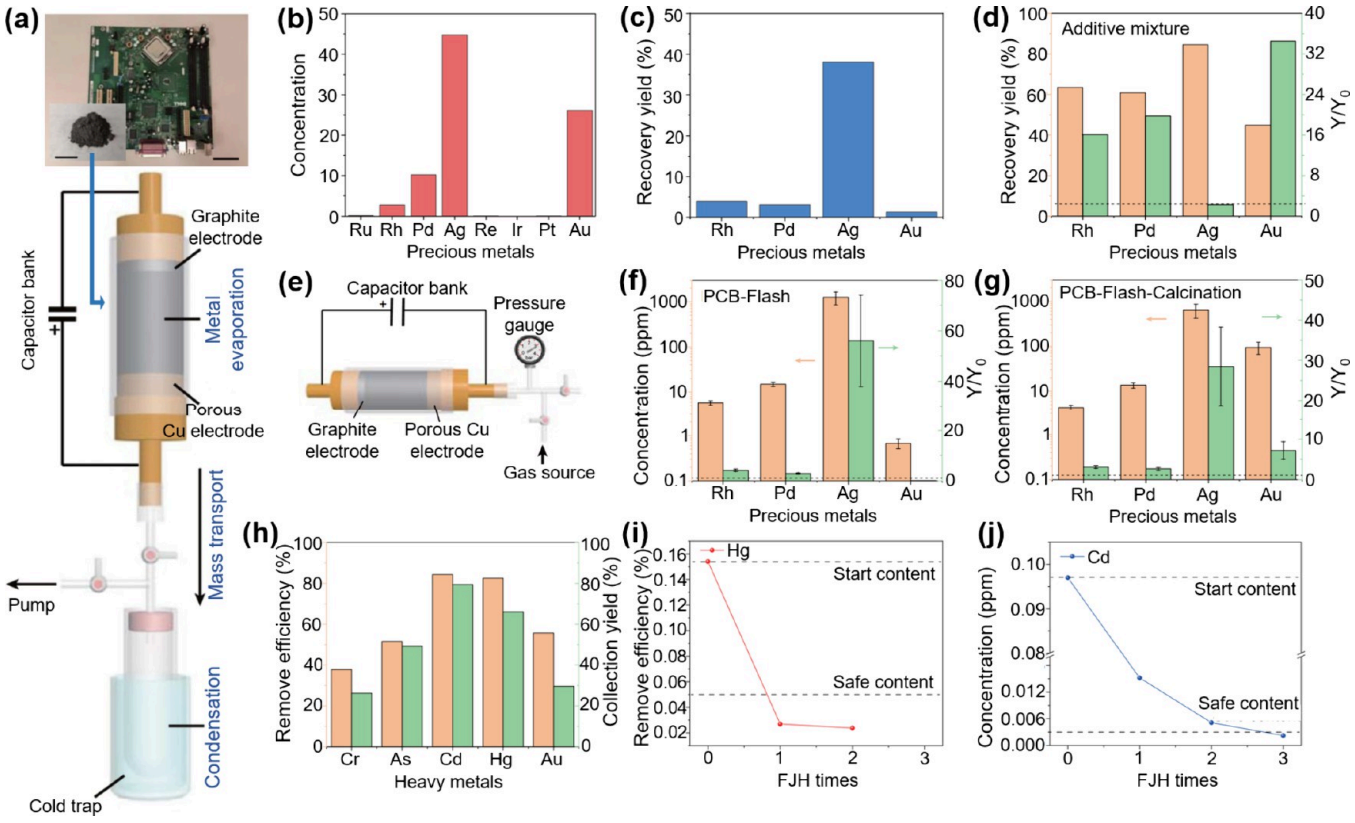

Figure 15. Urban mining via CTS. (a) Schematic of the evaporative separation strategy, (b) concentrations of precious metals in PCB, (c) recovery yield of precious metals by evaporation-based extraction, (d) recovery yield of precious metals with the additive mixture of NaF, NaCl, and NaI. Y_0 and Y are the recovery yields obtained without and with additives, respectively, (e) schematic of the pressurized strategy, (f, g) the concentration of precious metals and improved recovery yield caused by CTS (f) and CTS + calcination (g). Y_0 and Y are the recovery yields obtained by leaching the raw PCB and the treated PCB, respectively, (h) removal efficiency and collection yield of heavy metals, (i, j) the concentration of Hg (i) and Cd (j) in the residues after multiple CTS treatments. Reprinted with permission under a Creative Commons CC BY License from ref 191. Copyright 2021 Springer Nature.

L, 371.25 MJ, and 105.94 kg), and calcination-recycled anode (33.0 L, 28.76 MJ, and 3.78 kg).[187] So, CTS will become one of the most promising and reliable techniques to solve the world-class problem of recovering spent Li-ion batteries. Next, this recycling method's recovery efficiency and environmental conservation should be further evaluated to confirm whether it echoes the green manufacturing strategy before its practical application by resource recycling companies.

3.3.3. Urban Mining. Electrical and electronic equipment (EEE) is improving people's way of life and has become contemporary in the contemporary world. The quantity of electrical and electronic equipment utilized worldwide increased by 2.5 Mt annually.[188] When looking at another facet of EEE, 53.6 Mt electronic waste (e-waste) was generated in 2019 worldwide from damaged or obsolete devices, and the number will reach 74.7 Mt by 2030.[189] E-waste contains a lot of valuable and dangerous metals, and the concentrations of some precious metals in e-waste are much higher than those in ores.[190] Recycling valuable metals from e-waste, i.e., urban mining, has become very important for the circular economy.

CTS is starting to show its power in the area owing to its low energy consumption and pollutant discharge. Deng et al. reported the realization of recycling precious metals and the removal of toxic metals from a typical e-waste, i.e., a printed circuit board (PCB) removed from a discarded computer.[191] As shown in Figure 15a, the PCB was pulverized into powder, mixed with about 30 wt % carbon black, and then loaded into the quartz tube to perform the CTS treatment. The abundant precious metals in PCBs, including Rh, Pd, Ag, and Au (Figure 15b), evaporated at a high temperature of >3000 K. Then, the metal vapors were transported under vacuum and captured by condensation in the cold trap. The recovery yield of Ag was about 40%, while the yield of Rh, Pd, and Au were at a low level of 3% (Figure 15c). To improve the recovery yield, halides were added to raise metal atoms' vapor pressure by forming metal halides. The authors found that the F- and Cl-containing additives significantly improved the recovery yield of Rh, Pd, and Ag but contributed little to the recovery of Au. The effect of NaI on the recycling of Rh, Pd, and Ag was inferior to the F- and Cl-containing additives, but it improved the recovery yield of Au to >60%. Taken together, high recovery yield (>60% for Rh, >60% for Pd, >80% for Ag, and >40% for Au were achieved with the addition of the mixture of NaF, NaCl, and NaI (Figure 15d).

Besides the evaporative separation strategy, a pressurized setup was also adopted to trap precious metal atoms (Figure 15e). And then by leaching with dilute acids, precious metals were recycled from the residual CTS-treated solids. Compared to the leaching of the raw PCB materials, the recovery yield of the CTS-treated PCB increased by about 4.17, 2.90, and 56.0 times for Rh, Pd, and Ag, respectively (Figure 15f). However, the recovery yield of Au decreased due to the formation of covalent Au−C bonds. A further long-time and energy-consumption calcination was required to improve the recovery yield of Au. So, with both the CTS and calcination treatments, the recovery

https://doi.org/10.1021/acsnano.4c12350
ACS Nano XXXX, XXX, XXX−XXX

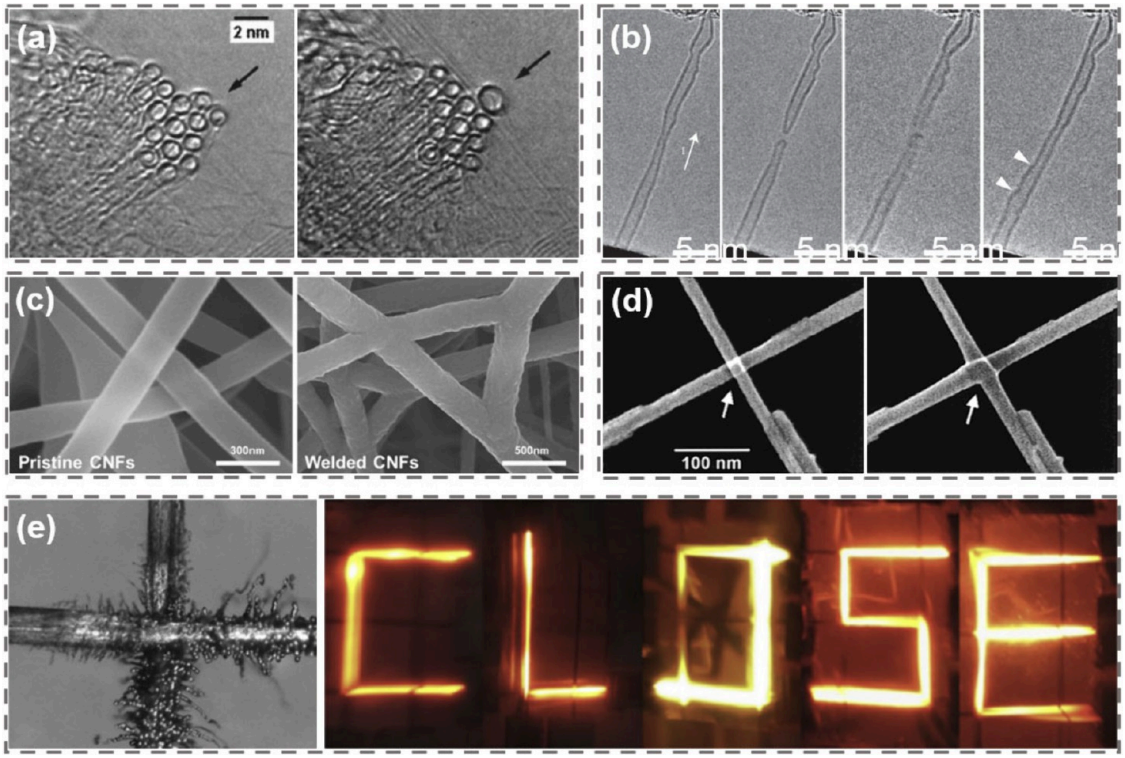

Figure 16. Soldering of carbon materials via CTS. (a) Coalescence of neighboring CNTs. Reprinted with permission from ref 194. Copyright 2021 Springer Nature. (b) Tip-to-tip joint of CNTs. Reprinted with permission from ref 196. Copyright 2008 Springer Nature. (c) Soldered cross-linking CNFs. Reprinted with permission from ref 282. Copyright 2016 American Chemical Society. (d) Soldered cross-linking single CNTs. Reprinted with permission from ref 201. Copyright 2001 American Chemical Society. (e) Soldered CNT fibers with different geometry.[22] Reprinted with permission from ref 22. Copyright 2017 Elsevier.

yields of Rh, Pd, Ag, and Au were increased by 3.11, 2.64, 28.5, and 7.24 times, respectively (Figure 15g). Both the economic efficacy and environmental efficiency of this strategy are inferior to that of the direct evaporation-based extraction strategy.

Toxic heavy metals in e-wastes, such as Cd, As, and Hg, can be selectively separated. The concentrations of these heavy metals in PCBs are at the level of 0.1−20 ppm, which have exceeded the safe limits of heavy metals in soils for agriculture. After the CTS treatment, these heavy metals were greatly removed from the residual solids and collected by condensation in the cold trap. The removal efficiencies were >80% for Hg and Cd, >50% for Pb, and >35% after one cycle of CTS treatment (Figure 15h). Concentrations of these toxic heavy metals can be further reduced by multiple CTS treatments. As shown in Figures 15i and 15j, the concentrations of Hg and Cd both went below the safe limits for agriculture.

In a nutshell, CTS began to show its power in recycling plastics, Li-ion batteries, and e-wastes. The ultrahigh temperature and ultrafast heating/cooling rate make it omnipotent in dealing with these wastes to regenerate valuable organics, minerals, and metals with high efficiency and low energy consumption. Next, it is foreseeable that the recyclable wastes of this rapid recycling strategy will be extended, and the recovery efficiency can be improved with other efforts. For instance, Deng et al. remediate multiple pollutants in soil via CTS.[192] All the heavy metals are vaporized while persistent organic pollutants are graphitized by the CTS-induced high temperature. This ultrafast CTS treatment can also retain soil mineral constituents, increase infiltration rate and exchangeable nutrient supply, and thus improve soil fertility and germination rates of crops.[192] For the CTS upcycling of organic wastes, catalysts used in conventional pyrolysis, hydrogenolysis, and photocatalysis methods can be introduced to further boost its efficiency.[193] However, a strict contamination assessment should be performed, especially on the gaseous byproducts, to confirm the environmental friendliness of this rapid CTS recycling strategy before its practical application.

3.4. Other Interesting Applications. Besides modifying and synthesizing nanomaterials, CTS can be used in many other applications, including the soldering of carbon materials, sintering of ceramic electrolytes, thermal tips, artificial muscles, and actuators. Here, we will discuss these applications in detail.

3.4.1. Soldering or Welding of Micro- and Macroscopic Carbon Materials. Soldering is one of the most reliable methods to firmly join two or more workpieces together and thus restore the joint's mechanical and electrical performance. However, unlike metals and thermoplastic polymers, carbon materials cannot be melted. The traditional fusion soldering technique does not work for carbon materials. CTS provides feasible methods to solder carbon materials through the reconstruction of carbon lattice or the growth of nanocarbon materials. In 2000, Terrones et al. reported the coalescence of CNTs (Figure 16a).[194] Since then, many researchers have verified that Joule-heating-induced high temperature can cause the coalescence and joining of different CNTs.[195−198] Sumio Iijima et al. observed that two CNTs with the same diameter were tip-to-tip joined together, just like plumbing water pipes, to form a long seamless CNT within 0.5 s (Figure 16b).[196] They demonstrated that the combined effect of Joule heating and electro-migration caused the joint of CNTs. Joule heating provided the activation energy for the joint of CNTs, while electro-migration prompted the generation and migration of topological defects and the

https://doi.org/10.1021/acsnano.4c12350
ACS Nano XXXX, XXX, XXX−XXX

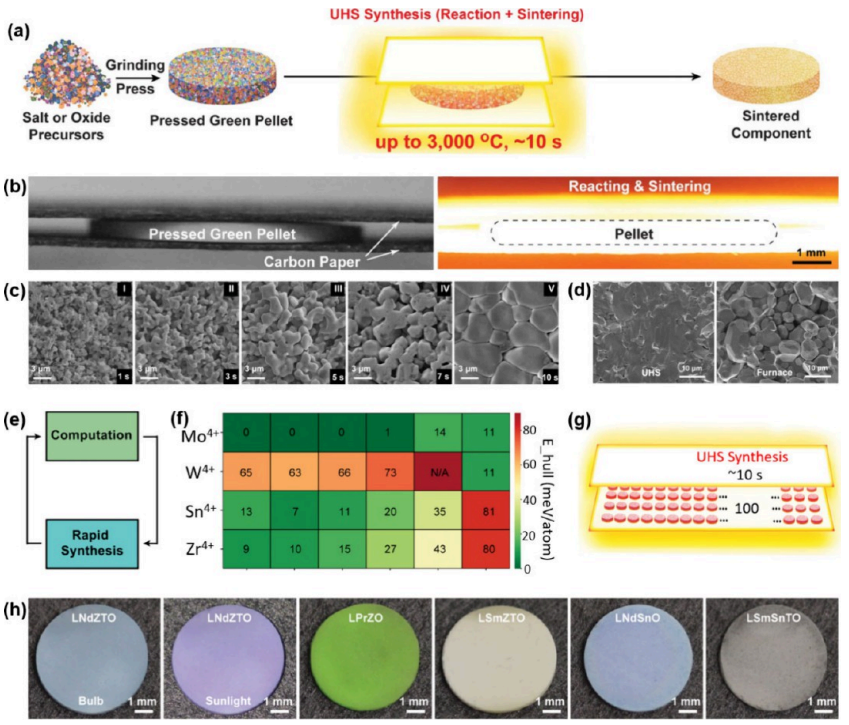

Figure 17. Sintering of ceramic solid electrolytes. (a) Schematic to show the sintering process of ceramic electrolytes via CTS, (b) photographs of the CTS sintering setup before heating (left panel) and heated at 1500 °C (right panel), (c) morphology evolution of the LLZTO ceramic during a 10-s CTS sintering, (d) cross-section view of the fractured CTS-sintered and conventional furnace-sintered LLZTO, (e) schematic to show the accelerated materials discovery enabled by computational prediction and rapid synthesis, (f) the predicted garnet compositions with different stabilities, (g) schematic to show the rapid and batch sintering of ceramic electrolytes via CTS in just ~10 s, and (h) garnet materials sintered via CTS technique and predicted by computation. Reprinted with permission from ref 118. Copyright 2020 AAAS.

interaction of local atoms. The formed defects can survive for tens of seconds,[197] and thus facilitate the tip-to-tip joint of CNTs. Wall-to-wall coalescence of double-walled CNTs was also observed.[198,199] Through the in situ TEM observation, Zhao et al. observed the zipping and unzipping process of two neighboring double-walled CNTs when they were electrically heated up to 2000 °C, and the two CNTs were coalesced together following the wall-to-wall configuration.[199]

Other carbon materials, e.g., CNFs and graphene, were also soldered via CTS. As reported by Yao et al., when polyacrylonitrile (PAN) based CNFs were heated up to a high temperature of >2500 K at a rate of ~200 K/min, hydrogen and nitrogen defects were activated, and then Bergman cyclization took place to form covalent bonds between adjacent CNFs with the removal of H and N.[200] Through these reactions, CNFs were further carbonized and the adjacent nanofibers were welded together to form 3D continuous carbon networks (Figure 16c). Confirmed by the Raman and TEM characterizations, the outer amorphous carbon shell of the PAN-based CNFs was converted into highly crystalline graphitic structures aligned along the longitudinal direction, and the formed carbon layers well bridged the neighboring CNFs at the cross-linking points, yielding an improved electrical conductivity of 380 S cm^{-1} and mechanical performance (the tensile strength increased from 0.31 to 3.86 MPa while the toughness improved from 1.265 kJ/m^3 to 20.65 kJ/m^3).[200] So, robust CNF joints were constructed via CTS. In another work, macroscopic graphene films were soldered with different configurations via the same CTS soldering technique.[202] The authors confirmed that during the CTS soldering process, the reactivity of carbon atoms at defective sites increased, and lots of dangling bonding formed at a high temperature of 2000 °C. It prompted the formation of interlayer covalent cross-linking around the defect sites. Benefiting from this effect, high adhesive strength and low contact resistance were restored at the joint of the welded graphene films. Other complex 3D architectures can also be constructed from 2D tailor-cut graphene sheets via CTS.[202]

Carbon materials can also be soldered via CTS with the deposition of carbon materials at the joint sites. As reported by Banhart in 2001, two crisscross CNTs were soldered together by the deposited amorphous carbon (Figure 16d).[201] However, though high mechanical properties can be restored at the joints, the deposited amorphous carbon cannot guarantee a good intertube electrical performance. As mentioned above, CTS can activate the growth of highly crystalline carbon materials. It provides a feasible way to connect two CNTs or CNT fibers mechanically and electrically with the newly grown highly crystalline carbon materials. As reported by our group in 2017, carbon nanofibers, carbon nanowalls, and amorphous carbon were grown at the joint of two overlapped CNT fibers via an electrothermal-induced deposition process (essentially, it is a CTS process).[22] SEM and TEM characterizations confirmed that a long carbon nanofiber was grown and firmly anchored in the CNT fibers. Then, clusters composed of short CNFs, carbon nanowalls, and amorphous carbon grew around this long CNF, and finally, a continuous and strong "rope" was formed to tie the two CNT fibers. With the growth of numerous "ropes", the two CNT fibers were robustly soldered together with fully recovered or even enhanced mechanical and electrical performances. And joints with different configurations, e.g., 1D line, 2D cross-linking, 3D skeleton, and even complex programmed circuits, were built through this quick soldering method (Figure 16e).

https://doi.org/10.1021/acsnano.4c12350
ACS Nano XXXX, XXX, XXX−XXX

Following this strategy, with the introduction of the iron catalyst (ferrocene), the deposition of nanocarbons also took place on the surface of other carbon materials and thus to solder the overlapped carbon materials, which confirms the university of this CTS-triggered soldering technique.

So far, nano-, micro-, and macro-scale carbon materials have been soldered via CTS, demonstrating the effectiveness of CTS in tailing and constructing complicated carbon structures at different scales. With the further improving CTS technique, especially the further reduction of heating size, micro/nano-scale carbon-based circuits and architectures can be constructed in the future, which is in line with the developing CNT- and graphene-based electronic and optoelectronic devices. But carbon-based circuits and devices are in their infancy. Practical applications are required to verify the reliability of the CTS soldered points, especially the mechanical strength, electrical conductivity, and long-term stability.

3.4.2. Sintering of Ceramic Electrolytes. Oxide ceramic electrolyte is one of the most appropriate solid electrolytes (SEs) to construct all-solid-state Li- and Na-ion batteries owing to its high ionic conductivity, chemical stability, and wide electrochemical window.[203] High temperature and long time are essential to densify SEs through conventional sintering techniques. However, there is a high risk of causing the volatilization of active Li or Na ions and the introduction of impurities during the long-time and high-temperature sintering process.[204] A reliable sintering method is in great demand to manufacture high-performance SEs and bind SEs with electrodes. Wang et al. have confirmed that CTS is appropriate to fabricate various ceramic electrolytes in seconds.[118] Taking Ta-doped $Li_{6.5}La_3Zr_{1.5}Ta_{0.5}O_{12}$ (LLZTO) as an example, the whole sintering procedure involved the mixing and pressing of precursors and the CTS sintering to get the final LLZTO electrolyte as schematically shown in Figure 17a. Two parallel strips of carbon paper were used as the heating element to generate CTS, between which the pressed green pallet of the precursor mixture was loaded (Figure 17b). After being heated up to 1500 °C (maximum 3000 °C) at a ramping and cooling rate of 10^3–10^4 °C/min and 10^4 °C/min, respectively, LLZTO ceramic electrolytes were sintered with a relatively small grain size of 8.5 ± 2.0 mm and a high relative density of ~97%.[118] Figure 17c shows the morphology evolution of the LLZTO electrolyte during a 10-s CTS sintering. The precursor pallet eventually became a densified LLZTO electrolyte. The cross-section views of the fractured CTS-sintered show a much more densely packed structure (left panel in Figure 17d) than the conventional furnace-sintered LLZTO (right panel in Figure 17d).

The heating temperature and ramping rate are crucial to control the grain size of the as-grown ceramic SEs. At low temperatures, although coarsening and densification of precursor particles competed during the sintering process, surface diffusion dominated the reaction and thus caused the coarsening of grains rather than densification. In contrast, at high temperatures, grain boundary and bulk diffusion played the leading role and thus led to the fast densification of ceramic SEs. The fast-heating rate shortened the low-temperature process and surpassed the grain coarsening while maintaining the higher capillary driving force for sintering. Besides, the ultrafast CTS sintering restrained the volatilization of Li atoms and helped retain most Li atoms. The Li loss was less than 4% after the CTS sintering, whereas 99% of the Li atoms were removed in the conventional furnace-sintered LLZTO.[118]

The combination of computational prediction and ultrafast CTS sintering accelerated the exploration of more ceramic electrolyte materials (Figure 17e). The authors listed the compounds calculated by density functional theory calculation, and their phase stability was described by the lower energy value above the hull (E_{hull}) in Figure 17f. Then, owing to the great universality of CTS to sinter various ceramic SEs, many ceramic electrolytes were sintered. Figure 17g schematically shows that 100 ceramic pellets were cosintered using a 20 × 5 matrix setup within an area of just 12 × 3 cm^2. So, this CTS-triggered sintering can be used in the high-throughput screening of bulk ceramics. Five different ceramics, including $Li_7Pr_3Zr_2O_{12}$ (LPrZO), $Li_7Sm_3Zr_2O_{12}$ (LSmZO), $Li_7Nd_3Zr_2O_{12}$ (LNdZO), $Li_7Nd_3Sn_2O_{12}$ (LNdSnO), and $Li_7Sm_3Sn_2O_{12}$ (LSmSnO), were successfully sintered as shown in Figure 17h. Besides, bilayer or even multilayer electrolytes were cosintered together without detectable side reactions or cross-diffusion, which retained the excellent performance of each layer. When incorporated with the 3D printing technique, CTS realized the sintering of ceramic structures with complex geometries, which were further stacked to form a more complex 3D lattice designed for different applications (e.g., the stacking of honeycomb structures featuring Al-doped SiOC for piezoresistive response and Co-doped SiOC for magnetic response to form a magnetic flux sensor).[118]

Similar works were also conducted by other researchers to sinter $Li_7La_3Zr_2O_{12}$ (LLZO), $Li_{1.3}Al_{0.3}Ti_{1.7}(PO_4)_3$ (LATP), $Na_3Zr_2Si_2PO_{12}$ (NZSP), and SiC-based electrodes with different power inputs (current or microwave irradiation) and different CTS parameters (temperature, duration, and heating/cooling rate).[57,95,205,206] For instance, LLZTO was also sintered using microwave-induced CTS. High relative density (94.5%), Li retention (94%) as well as the cosintering of the LLZTO electrolyte layer and LATP electrode were all realized.[57] So, CTS becomes a powerful method to fabricate ceramic and other SEs, and the performance of these SEs can be easily modified by changing the composition and the CTS parameter. With the scaled-up batch production or the roll-to-roll sintering method, CTS also has the potential to fulfill the industrialization and commercialization of various SEs.

3.4.3. Thermal Tips. Thermal tips are a kind of tiny hot-point drills that can convert electrical energy into highly centralized heat efficiently and generate localized high temperatures at the microscale or even nanoscale.[207] It is the key unit of the thermal scanning probe photolithography (TSPL) system. With a setup to scan the thermal tip on the sample surface, TSPL can implement efficient direct-write patterning to create dense high-resolution features on material surfaces.[208,209] During patterning, the thermal tip is scanned in contact with material surfaces to trigger highly localized reactions, and meanwhile, topography can be visualized by the scanning probe microscopy imaging system in real time. All these fantastic features of TSPL make it versatile in the surface modification of materials or the fabrication of micro- and nanodevices.[210−212] The heating temperature of the thermal tip controls the localized reaction, while the tip size determines the machining precision of TSPL. That is, the capability of the thermal tip determines the overall performance of TSPL. The maximum sustainable heating temperature and the processing speed of the conventional metal tips are restricted by their low melting point and heating/cooling rate. Now, TSPL are usually used in biomedical, nanomagnetic, and nanoelectronic fields to deal with biological tissues, to produce local field cooling, and to remove heat-labile

https://doi.org/10.1021/acsnano.4c12350
ACS Nano XXXX, XXX, XXX−XXX

resist now.[208,211,213] The machining precision of TSPL has reached sub-10 nm.[214] It has been used to fabricate high-performance 2D devices—edge-contact MoS_2 FETs.[215] However, TSPL is only used to pattern organic resists now. With the development of CTS, the carbon-based tip will bring a vital force into this field. The ultrahigh temperature (>3000 K) and ultrafast heating/cooling rate (10^5 K/s) will enable the mask-less patterned growth or modification of materials to realize the direct construction of nanodevices.

In 2021, Zhi et al. published an important work in which a 3D-printed rGO-based thermal probe was made to realize the patterned deposition of Pt nanoparticles with high spatial (submillimeter scale) and temporal (milliseconds) resolutions.[28] rGO probes were constructed with different sizes, shapes, and geometries (Figures 18a–f). They all have smooth surfaces and cellular porous internal microstructures (Figures 18c and 18d). The smooth surface facilitated the smooth movement of the tip on the sample surface, while the cellular microstructure not only maximized the structural robustness to maintain its shape,[216,217] but also facilitated the control over the electrical conductivity of the thermal tip, which contributed to the efficient heating and operability of the rGO thermal probe. The thermal probe that featured a microtip possessed excellent heating capabilities. It could be heated up to 3000 K at an ultrahigh ramping rate of about 10^5 K/s, and ultrashort durations of milliseconds were achieved to generate the controllable thermal shock. So, it is an ideal thermal source for nonequilibrium heating and to activate the material synthesis,

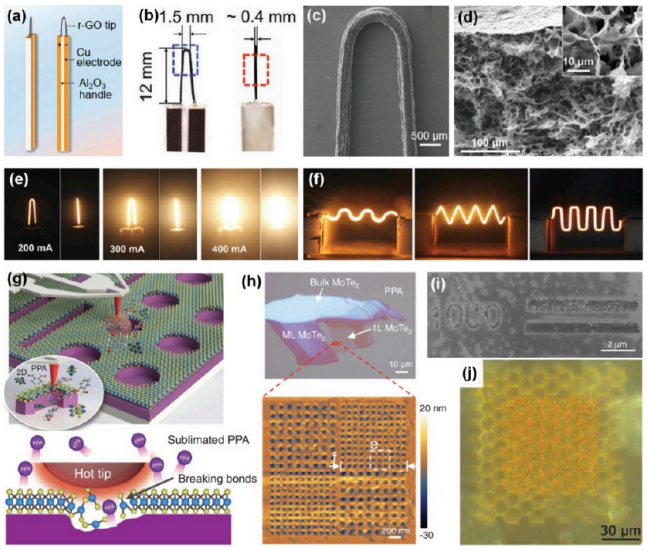

Figure 18. Carbon-based thermal tips. (a) Structure of a graphene-based thermal tip, (b) overall shape and size of this thermal tip, (c) overall surface morphology and (d) interior morphology of this thermal tip, (e) the same thermal tip heated by different currents, and (f) heated thermal tips with different shapes. Reprinted with permission from ref 28. Copyright 2021 John Wiley and Sons. (g) Schematic to show the nanocutting of 2D TMDC via TSPL, and (h) TSPL treated $MoTe_2$ flake and the $MoTe_2$ nanosquare structures with 50 nm side (top right and bottom left) and 70 nm (top left and bottom right). Reprinted with permission from ref 218. Copyright 2020 John Wiley and Sons, Ltd. (i) Sb_2S_3 structure created by TSPL, and (j) double-layer 3D honeycomb Sb_2S_3 structure. Reprinted with permission under a Creative Commons CC BY License from ref 219. Copyright 2020 John Wiley and Sons.

Thermal tips based on CNT and carbon fiber were also fabricated. The outstanding axial thermal conductivity and high mechanical strength make it the perfect thermal probe to measure the nanoscale thermophysical properties.[220] Owing to the ultrasmall radius of the single CNT, the spatial resolution of CNT-based thermal tips can reach up to the nanometer scale, the limit defined by fundamental constraints such as the mean free path of heat carriers.[221,222] For example, an extremely high thermal spatial resolution of 30 nm was achieved while the topography resolution reached 20−30 nm for a CNT thermal tip.[220] It was used to study thermal transport in microscale interconnects and few-layer graphene. It would facilitate the direct writing of complex structures and the manufacture of customized materials with high resolutions.[220] Recently, Xie et al. reported that the carbon-fiber tip can even generate uniform large-area volumetric plasma at atmospheric pressure with a temperature of up to 8000 K.[223] The generated hot plasma has surpassed many conventional atmospheric plasmas in spatial uniformity, stability, and heating temperature range. This tip can realize rapid temperature switches between 10,000 and 6000 k within 1 s, which can generate a miraculous nonequilibrium condition for the synthesis of extreme materials, including ceramics, alloys, and CNTs.[223] This will further extend the application range of CTS-enhanced thermal tips.

Now, many works have demonstrated the nanofabrication of 2D devices using TSPL. For example, Liu et al. reported the nanocutting of 2D materials to construct arbitrarily shaped nanostructures with a resolution of 30 nm via TSPL.[218] During this process, the chemical bonds were thermomechanically cleaved, while the polymer layer underneath the 2D material was rapidly sublimated by the thermal nanotip (Figures 18g and 18h). Conde-Rubio et al. combined hot-tip patterning and Ar^+ milling to etch 2D materials. Followed by metal deposition and the lift-off procedures, edge-contact MoS_2 FETs were fabricated via TSPL.[215] This device fabrication method can also be applied to other 2D materials, e.g., graphene[224] and $MoSe_2$.[225]

Besides, the Joule heat generated by the thermal tip can activate the localized chemical reaction and thus directly fabricate patterned micro- or nanodevices. For example, devices based on metal chalcogenide semiconductors were directly grown from the metal−organic precursors via TSPL patterning (Figure 18i).[219] To be specific, during the TSPL patterning process, the thermally treated metal−organic precursors decomposed to form insoluble metal chalcogenides while the untreated region remained soluble. Then, devices with well-patterned structures were directly obtained by washing away the untreated soluble parts. However, the machining precision and processing capability of TSPL at present is inferior to conventional UV light lithography (UVL) and two-photon absorption lithography (TPAL), as shown in Figures 18i and 18j. It must be admitted that the spatial resolution of TSPL is now far below that of photolithography. The further miniaturization of thermal tips is one of the direct methods to improve the resolution of TSPL. So, the fabrication technique of thermal tips should be further improved. The limiting dimension of thermal tips can reach the level of the diameter of a single CNT or the thickness of monolayer graphene. Both the CNT and graphene-based thermal tips have high thermal conductivity. The resolution of carbonene-based thermal tips has the potential to reach the limits defined by fundamental constraints, e.g., the mean free path of heat carriers and Kapitza contact

https://doi.org/10.1021/acsnano.4c12350
ACS Nano XXXX, XXX, XXX−XXX

resistance.[220,221,226] In the future, with the improving techniques of CTS and thermal tip, especially the improvement in precision and accuracy of the heating temperature and dimension, the machining precision of TSPL can be improved, and the "lab-on-chip" preparation of electronic and optoelectronic devices will be realized via TSPL.

3.4.4. Actuators and Artificial Muscle. Actuators and artificial muscles can change their shape or volume in response to external stimuli. Here, actuators refer to those carbon-based soft "motors" that can generate rotation motions and be widely utilized in various fields, e.g., robotics and sensors. Artificial muscles are soft actuators that can produce axial rectilinear motion, and they have attracted lots of attention owing to their ultrafast response, large stroke, and high output power.[227−232] CTS generated in carbon materials is an effective stimulus to activate the tensile and rotational movement of actuators and artificial muscles. As reported by Baughman et al. in 2012, by infiltrating and confining paraffin wax inside the nanopores of the twist-spun CNT fibers, the formed CNT/wax actuator generated high-force and large-stroke actuations when stimulated by the ultrafast CTS generated by the current passing through the CNT fiber.[233] The working mechanism of the actuator is very simple. The intermittent Joule heat generated by the CNT fiber would make the wax change between solid and melting states and thus generate a volume change of about 20%. The helical geometry of CNT fiber helped to convert the volume change into torsional rotation and tensile contraction. High-performance actuators were fabricated from this simple structure. Benefiting from the ultrafast heating and cooling rate of CTS, the actuator spun at a high average rotation speed of 11,500 rpm and delivered 3% tensile contraction at 1200 cycles/min. Soon after, the same team improved the stability of the actuator, which spun at a speed of 9800 rpm without noticeable oscillation.[228] The specific mechanical powers were increased to 5.3 W/g for the actuator based on CNT-wrapped sewing thread[229] and 1.98 W/g for a sheath-run artificial muscle.[234]

Wang et al. reported that the bilayer actuator based on CNT and BN can switch at frequencies from sub-Hertz to about 30 Hz by quickly heating the actuator to 2000 K within 100 ms.[235] The actuator was fabricated by sequential filtration of CNT and BN nanosheets. The formed CNT film not only offers excellent mechanical support for the BN layer but also serves as the heating element to generate CTS. The actuator with a length of 9.5 mm yielded a deflection of >3 mm. Besides, owing to the high thermo-mechanical stability of CNT and BN, this actuator worked steadily for over 10,000 cycles with negligible degradation in an inert gas environment.

In short, CTS can act as the efficient stimuli to drive the fast tensile, rotational, and deflectional movement of actuators and artificial muscles, enabling the construction of smart and interactive soft robotic systems. It will facilitate the application of these devices in engineering and biomedical fields. It should be noted that CTS-triggered actuators or artificial muscles rely on the thermal response of different materials. So, except for the mechanical work output, the energy consumption should be reduced by lowering the working temperature. To achieve this goal, the working medium, e.g., the phase change material embedded inside the carbon-based actuators or artificial muscles, and the architecture of the actuators or artificial muscles must be well designed.

4. FUTURE PROSPECTS

4.1. Precise Control of CTS. The low controllability is the main issue that limits the further development of the CTS technique. Consulting all the applications listed above, the heating and cooling procedure is critical for the synthesis of nanomaterials, recycling of waste materials, fabrication of nanodevices, and other applications in functional devices. For example, the nucleation and growth are controlled by the temperature procedure during the chemical vapor deposition process of low-dimensional materials.[236,237] So, accurate control over the temperature program, not only the maximum temperature and heating/cooling rate, but also the finely controlled heating/cooling procedure, and temperature field are necessary to exert the utmost performance of CTS in the fabrication and modification of nanomaterials or devices. The pressure change is also crucial for the CTS-triggered modification and synthesis of nanomaterials. However, the ultrahigh heating temperature, ultrahigh heating/cooling rate, and transient pressure change (i.e., barometric shock) of CTS make it difficult to precisely modulate all these key parameters using existing temperature and pressure measuring techniques. The commonly used power supplies, including capacity discharge and microwave irradiation, have their inherent shortcomings in the fine regulation of the temperature procedure of CTS.[11,143,178,191] Besides, the dramatically changed temperature must cause transient and localized changes in pressure and gas volume during the CTS process. The response speed of a highly sensitive state-of-the-art barometer based on MEMS piezoresistive cantilevers is only 10 Hz.[238] It still cannot catch up with the transient barometric shock and give the real-time pressure evolution. So, the overall controllability over CTS is currently lagging behind traditional heating techniques, and researchers have not understood the mechanism behind the CTS-triggered shock chemistry (especially CTS-triggered localized transient chemical vapor reaction) due to the absence of temperature and pressure information.

A high-precision energy supply and high-performance temperature monitoring system are the prerequisites for highly controllable CTS. Specially designed high-power pulse generators are needed to fulfill the controllable material synthesis and other functional applications. Very recently, with the help of a DC power supply equipped with a solid-state relay device, Dong et al. have realized programmable pulsed heating and quenching (PHQ) with finely regulated peak temperatures and heating/cooling profiles.[239] The carbon heater can be repeatedly and precisely heated to 2400 K for 0.2 s and then cooled to ambient temperature within 0.8 s by switching the electrical power on and off. The temporal temperature pattern is provided in this work. This high-efficiency heating technique ensures nonequilibrium thermochemical reactions with high selectivity. Taking CH_4 pyrolysis as the model reaction, a high C_2-product selectivity of about 80% has been reached via PHQ, while the selectivity is only 40% for the conventional continuous heating method. Besides, the temperature field of CTS can also be well regulated by the geometric structure design of carbon heaters. As mentioned in Section 3.3.1, a spatial temperature gradient is achieved in the bilayer heater made of porous carbon felts. Such temperature gradient promotes the continuous melting, wicking, vaporization, and reaction of plastics, which enables the eco-friendly recycling of plastic wastes.[177] But unfortunately, faster programmable heating and quenching have not been reported

https://doi.org/10.1021/acsnano.4c12350
ACS Nano XXXX, XXX, XXX−XXX

yet to provide more information for the mechanism revelation of the shock chemistry.

Researchers have just begun to study the effect of pressure shock on the CTS-triggered synthesis of materials and fabrication of devices. As estimated by Deng et al., the localized pressure reached about 5 atm, and the localized gas velocity was up to 800 m/s during the transient CTS process.[191] It definitely affects the modification and growth of the aforementioned nanomaterials as well as the fabrication of nanodevices. In the latest work, Huang et al. confirmed that the mechanical barometric shock significantly affects the graphitization of carbon materials.[240] The pressure quickly rises to 21.64 MPa and then drops to the equilibrium level within 76 ms. Such a transient barometric shock disrupts the $\pi-\pi$ interactions in the aromatic chains, causing the formation of hybrid-structured carbon composed of crystalline and amorphous carbon with the help of high-temperature thermal shock (maximum temperature at 3273 K, heating rate of 10^5 K/s, and cooling rate of 10^4 K/s). The obtained hybrid-structured carbon material exhibits excellent electrochemical properties when served as andodes of Li-ion batteries, e.g., 208.6 mAh/g in capacity and 81% retained performance after 3000 charge−discharge cycles.[240] More theoretical and experimental works are still needed to figure out how the transient temperature, pressure, and volume fluctuations affect the nucleation, growth, decomposition, and volatilization of different materials. The control parameters, including the peak temperature, heating/cooling rate, pressure, etc., should be added to the scope of regulation simultaneously to further improve the controllability of CTS and expand its technological advantages in the aforementioned applications or go to other application fields.

Moreover, with the fine-controlled CTS, the process−structure−property relationships should be mapped to guide the synthesis or modification of nanomaterials. Several works have dug into this area, but not deeply. For example, some theoretical calculations have predicted the composition-structure−property relationship of HEA NPs.[241−243] And experimentally, Ding et al. directly observed the atomic composition and structure differences of two different HEA alloys.[244] The five elements were randomly distributed in the face-centered cubic CrMnFeCoNi Cantor alloy, while the five elements in the face-centered cubic CrFeCoNiPd alloy aggregated with a wavelength of incipient concentration waves of 1−3 nm. Such pronounced composition fluctuations resulted in nanoscale alternating tensile and compressive strain fields, caused the increase in stacking-fault energy, and finally generated a higher yield strength without compromising the strain hardening and tensile ductility of the CrFeCoNiPd alloy. The authors established an atomic-scale composition-structure-mechanical property rule for this HEA NPs. The rapid manufacturing capability of CTS will help to figure out the process-structure−property relationships of other materials, which will significantly extend the impact of CTS in nanomaterial manufacturing.

4.2. Revelation of the Mechanism behind CTS. Usually, the whole CTS process is finished within a few seconds or even milliseconds, making it hard to review the underlying mechanism with conventional methods. We now lack enough knowledge about the mechanism of this cutting-edge thermal manufacturing method to guide the precise control of the component, morphology, and structure of the synthesized nanomaterials or regenerated wastes. So, in the next phase, efforts should be made to ravel out this issue and realize the highly controllable synthesis or modification of nanomaterials.

With the help of in-situ characterizations, researchers have some early snapshots into the real-time evolution of the nanomaterials during the CTS process. For example, Hettler et al. monitored the CTS reduction process of GO through in-situ TEM characterization.[70] They found that the CTS reduction of GO took place in a localized manner only when the input power density reached the threshold value. In another work, Huang et al. observed the formation of NPs on the carbon substrate during the CTS process and captured the kinetic process with high spatial and time resolution.[245] They demonstrated that the interaction between the substrate and NPs dominated the formation process and led to the uniform dispersion and high stability of the obtained HEA NPs. However, we have not found detailed information about the in situ TEM characterization. In a similar work, Hettler et al. confirmed that the ultrashort heating time and the strong bonding between HEA NPs and graphene nanosheets suppressed the migration and subsequent agglomeration of the formed NPs.[246] Or in other words, the GO nanosheets anchored the formed HEA NPs and thus guaranteed the narrow size distribution and uniform dispersion of HEA NPs. However, these works are insufficient to reveal the underlying mechanism of CTS-triggered manufacture clearly. For example, though the atomic-level resolution scanning transmission electron microscopy (STEM) coupled with energy dispersive Xray spectroscopy (EDS) analysis revealed the homogeneous mixing state in the HEA NP,[247] further theoretical and experimental works are still needed to figure out the mechanism and key parameters to control the component, morphology, and structure of the products.

4.3. Machine-Learning Guided Synthesis. Machine learning (ML) is a cutting-edge subfield of artificial intelligence and has become a powerful method for the fundamental study of material science.[248−250] It offers an efficient and important tool to analyze the existing materials, predict the properties of different materials, and accelerate the material design process.[251−254] Taking HEA as an example, many researchers have utilized ML to guide the discovery, phase prediction, and property design of HEA.[255−261] For example, Huang et al. employed three different ML algorithms, i.e., K-nearest neighbors (KNN), support vector machine (SVM), and artificial neural network (ANN), to explore the phase selection rule with a comprehensive experimental data set containing 401 HEAs, which includes 174 kinds of solid solution, intermetallic compound (IM), and mixed SS and IM phase. They found that ANN gave the highest accuracy in classifying the SS, IM, and mixed SS + IM phases.[256] Chang et al. then used the ANN algorithm to predict the composition of AlCoCrFeMnNi-based HEAs to achieve high hardness.[262] The ML prediction revealed that three candidates could have an optimum hardness of 670 HV, and the experimental data confirmed this prediction. Similarly, to search for HEA with high hardness, Wen et al. proposed a property-orientated design strategy combining ML, and they predicted 17 AlCoCrCuFeNi-based alloys that were harder than the existing HEAs used for training the model.[255] These works have shown the efficiency of ML in searching for HEAs with desired properties.

The combination of ML and CTS has sparked the enthusiasm of material scientists and will fuel the rapid expansion of the application of CTS in different fields. Beckham et al. utilized ML to guide the CTS synthesis of graphene.[263] Graphene

https://doi.org/10.1021/acsnano.4c12350
ACS Nano XXXX, XXX, XXX−XXX

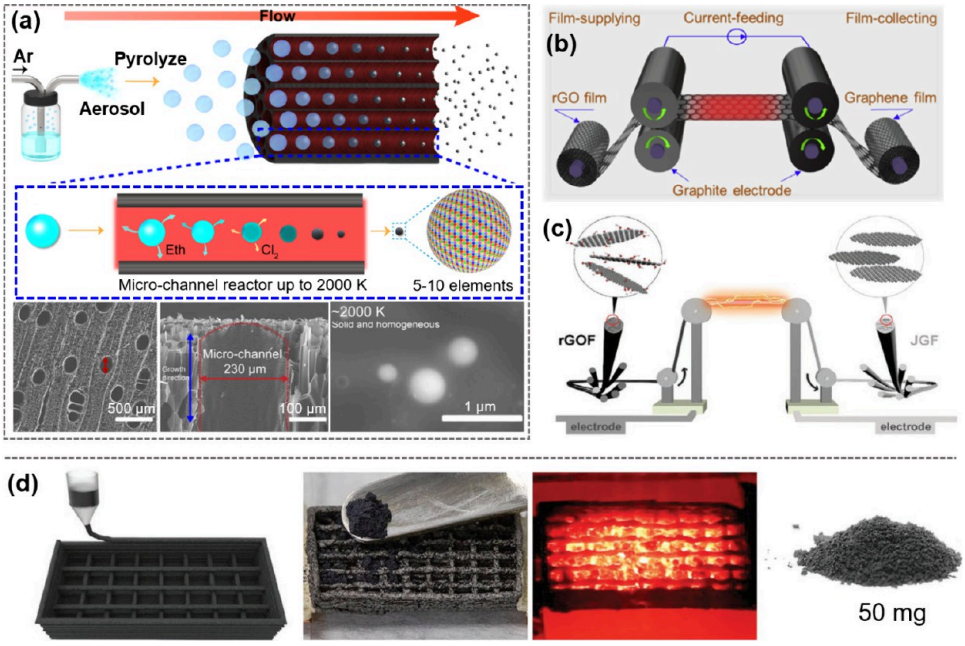

Figure 19. Mass production of nanomaterials realized via CTS. (a) Floating CVD-based mass production of nanoparticles, including its setup, mechanism schematic, the carbonized wood used to generate CTS, the microchannels that served as the microreactors, and the HEA products. Reprinted with permission from ref 33. Copyright 2020 Elsevier. (b) Roll-to-roll fabrication of graphene film. Reprinted with permission from ref 85. Copyright 2019 Elsevier. (c) Roll-to-roll fabrication of graphene fiber. Reprinted with permission from ref 277. Copyright 2022 John Wiley and Sons. (d) Batch production of Ru nanoparticles with the 3D printed rGO reactor. Reprinted with permission from ref 23. Copyright 2020 John Wiley and Sons.

synthesized from different starting materials, e.g., carbon black, plastic waste-derived pyrolysis ash, pyrolyzed rubber tires, and metallurgical coke, were analyzed by wide-area Raman mapping, which was chosen as the principal metric of characterization, to evaluate the yield of graphene. The obtained >20,000 Raman spectra were used as the database to train six ML regression models using 5-fold cross-validation, including linear regression (LR),[264] Bayesian (BR),[265] multilayer perceptron (MLP),[266] decision tree (DT),[267] random forest (RF),[268] and eXtreme Gradient Boosting (XGB)[269] regression models. RF and XGB performed better (root mean squared error and r^2 score of 12.7% and 0.7808 for RF and 11.3% and 0.8051 for XGB).

Five features, i.e., charge density (CD), material type (M), area under the time−current curve divided by the sample mass (A_{IT}), the maximum current divided by the sample mass (I_{Max}), and final current divided by the maximum current (I_F/I_{Max}) were used to train the ML models. The most accurate XGB model revealed that CD was the most critical one that affected the yield of graphene. A high CD should be employed to get a high graphene yield. The carbon source, i.e., M, also greatly affected the final yield. Metallurgical coke particles with large particle sizes offered the lowest yield. The authors gave a partial analysis in this work. Graphene yield increased with the increasing values of the three features (CD, A_{IT}, and I_{Max}). And then, the yield plateaued at higher values. This result demonstrated that the reaction kinetics changed from the surface reaction-controlled nucleation at a low energy density to the diffusion-controlled regime at a high energy density. The diffusion-controlled reaction might make it possible to control the size of synthesized graphene crystals.[263]

Then, the authors used the ML-predicted parameters to guide the synthesis of graphene from pyrolyzed rubber tires. A high yield of 79% was achieved with no prior knowledge about the starting material.[263] This work presents the power of the combination of ML and CTS in synthesizing graphene. However, the controllable factor in this work is limited. If high-power pulse current is employed to generate CTS, more features, including peak current, rise/fall time, frequency, duty ratio, and duration, can be input to train the ML model and thus give a detailed prediction to make the CTS synthesis of graphene and other 2D materials more controllable in the crystallinity, morphology, lateral size, and layer number.

Next, high throughput prediction (HTP)[270] and high throughput characterization (HTC)[271] can be integrated with ML-guided CTS synthesis of nanomaterials. The combination of CTS's ultrafast synthesis ability, ML's high efficiency in determining growth parameters, HTP's high efficiency in searching for customized materials to meet the requirements of specific applications, and HTC's ultrafast characterization capacity provides an highly efficient approach for the screening of desired materials with optimized composition, structure, and desired performances for specific application. It will boost the exploration of advanced nanomaterials and help to find a way to realize the controllable synthesis of customized nanomaterials, especially high-entropy materials with extreme diversity in composition and phase structure.

4.4. Mass Production. CTS has been validated as an efficient and economical method to synthesize low-dimensional nanomaterials. To extend its practical utility, the production capacity of CTS should be upgraded to realize the low-cost mass production of desired materials. This will be one of the key research directions in the next phase. Some forefront works have provided several feasible strategies to realize the mass production of HEA nanoparticles and graphene via CTS.

The first one is similar to the floating CVD growth of CNTs.[272−274] Precursors (usually solutions of metal salts) are carried by the gas mixture to pass through the high-temperature reacting region to continuously synthesize HEA NPs.[26,275]

https://doi.org/10.1021/acsnano.4c12350
ACS Nano XXXX, XXX, XXX−XXX

However, the finite heating temperature of conventional tube furnaces is not high enough to support the synthesis of arbitrary HEA NPs, and the energy consumption is high. To solve this problem, Wang et al. used carbonized wood as the heating element to fulfill the continuous synthesis of HEA and HEO nanoparticles via CTS with a high heating temperature (Figure 19a).[33] The vessel channels with diameters of about 200 μm in the carbonized balsa wood right served as the microchannel reactors. The compact size enabled homogeneous heating, reduced the residence time, and thus provided a superior heating capability, e.g., heating temperature of >2000 K, duration of milliseconds, and uniform temperature distribution inside these microchannel reactors. Then, with the continuously supplied precursors, HEA and HEO NPs with desired components and sizes were continuously synthesized inside these microchannel reactors.[33] In another work reported by Qiao et al., two carbon papers are set face-to-face with a small gap (1−3 mm) and heated up to 3200 K to serve as a fly through high-temperature reactor with a large reaction space and a uniform temperature gradient.[276] Precursors (Pt salts) loaded on carbon black can be quickly converted into Pt NPs via a shock reaction when they flow down through the heated reactor (1400 °C) under the force of gravity and carrier gas. The obtained Pt NPs are uniformly anchored on the surface of carbon black with an average size of about 4 nm. The particle size can be further improved to 7 nm by raising the heating temperature to 1700 °C.[276] These two works offer a highly feasible method to realize the mass production of NPs via continuous fly-CTS reaction.

Second, the roll-to-roll manufacturing technique has been widely used in the growth and transfer of 2D materials (especially graphene and TMDCs) at present,[278−283] and it can be further modified to incorporate with CTS to fulfill the mass production or massive modification of nanomaterials. For example, feeding current into the rGO film or fiber, the generated high temperature converted the rGO film and fiber into the highly crystalline graphene film or fiber (Figures 19b and 19c).[85,277] The rotating rollers made this CTS treatment continuously proceeded to realize the mass production of graphene film and fiber. In another roll-to-roll fabrication process, current was conducted in the continuously transferred copper film, and graphene was directly grown on the heated copper substrate with the continuously supplied H_2 and CH_4.[142] Owing to its easy implementation, this continuous fabrication strategy can realize the mass production of the aforementioned HEA NPs and SAs as well as other 1D and 2D nanomaterials on the carbon matrix.

Large-scale batch production is another alternative method to realize the mass production of nanomaterials via CTS, and it has been realized in carbon-based reactors. In 2020, Qiao et al. constructed a versatile miniature rGO reactor by 3D printing and applied it to synthesize Ru nanoparticles (Figure 19d).[23] This rGO reactor can be heated up to 3000 K with an ultrafast heating and cooling rate of about 10^4 K/s. $RuCl_3$ loaded inside the channels of the mesoporous carbon can be ultraquickly converted into Ru NPs with an average size of about 2 nm at about 1500 K within 500 ms. The yield reached 50 mg/batch in this miniature reactor,[23] which can be further scaled up by just magnifying the reactor and the input electrical energy. These works have revealed the potential of CTS in the mass production of nanomaterials. To realize this goal, it requires the deep cooperation of the material scientists, equipment manufacturers, producers, and users to establish a whole set of practicable production techniques.

5. CONCLUSION

In this review, we systematically introduce the CTS technique and its wide application in the synthesis and modification of nanomaterials as well as the fabrication of micro/nano-devices. Recent progress, future developing directions, and prospects have been summarized, from which we can outline the two main superiorities of CTS. First, the rapid reaction, high efficiency, and mass production ability will boost the low-cost and green manufacturing of nanomaterials and micro/nanodevices. Second, the wide range of heating temperatures, ultrafast heating and cooling rate, nonequilibrium reaction process, and extremely efficient manufacturing capabilities can promote the exploration of desired materials via CTS. However, there are still some problems and challenges related to the CTS technique. The first challenge is to investigate the transient CTS process and its mechanism. Specially designed measuring systems are required to monitor the transient temperature evolution and barometric shock, providing more information for fully understanding the reaction kinetics and growth mechanism behind the CTS-triggered synthesis of nanomaterials and the fabrication of devices. The second issue is how to realize the precise control of the morphology and structure of as-synthesized nanomaterials. More control parameters should be extracted to further improve the controllability of CTS-triggered reactions. Now, the high-speed thermal shock always facilitates the formation of small-size solid particles or lamellae. More efforts are needed to explore CTS's capacity in synthesizing nanomaterials with different configurations, such as large-scale 2D, hollow, and core−shell structures. Besides, the machining accuracy of carbon heaters, including thermal tips, flat, 2D-patterned, and 3D-structured carbon heaters, should be further improved for better control over the temperature field. All these efforts will make CTS an innovative heating technique for the synthesis of nanomaterials and the fabrication of nanodevices.

AUTHOR INFORMATION

Corresponding Authors

Jingyun Zou − *Jiangsu Key Laboratory of Micro and Nano Heat Fluid Flow Technology and Energy Application, School of Physical Science and Technology, Suzhou University of Science and Technology, Suzhou 215009, China; Division of Advanced Nano-Materials, Suzhou Institute of Nano-Tech and Nano-Bionics, Chinese Academy of Sciences, Suzhou 215123, China;* orcid.org/0000-0002-9976-6895; Email: jyzou2021@usts.edu.cn

Lei Tang − *Songshan Lake Materials Laboratory, Dongguan, Guangdong 523808, China;* orcid.org/0000-0002-4586-3104; Email: tl17@tsinghua.org.cn

Lixing Kang − *Division of Advanced Nano-Materials, Suzhou Institute of Nano-Tech and Nano-Bionics, Chinese Academy of Sciences, Suzhou 215123, China;* orcid.org/0000-0003-3837-7711; Email: lxkang2013@sinano.ac.cn

Complete contact information is available at: https://pubs.acs.org/10.1021/acsnano.4c12350

Notes

The authors declare no competing financial interest.

ACKNOWLEDGMENTS

The authors acknowledge the project supported by the National Natural Science Foundation of China (No. 52202044 and No. 52302190), the Suzhou Science and Technology Program for

https://doi.org/10.1021/acsnano.4c12350
ACS Nano XXXX, XXX, XXX−XXX

Industrial Prospect and Key Technology (No. SYC2022018), and the Startup Program of Suzhou University of Science and Technology (No. 332114704 and 342234701).

VOCABULARY

Carbothermal shock, a heating technique that relies on the rapid Joule heating and quenching ability of carbon materials to generate ultrahigh temperature and ultrafast heating/cooling rates; Single atom, a single isolated metal atom or single transparent metal complex modified on a suitable carrier with high catalytic activity; High entropy alloy, an alloy contains five or more principal metallic elements in near-equiatomic proportions and have a single-phase crystal structure; Upcycling, a term refers to the creative reuse or the process of transforming byproducts, waste materials, and useless or unwanted products into other valuable materials or products; Urban mining, to regard human habitat and the built environment as a source of raw materials, extract resources and recover/reuse wastes generated by human activities; Thermal tip, a tip that can convert electrical energy into highly centralized heat efficiently and generate localized high temperatures at micro- or even nanoscales; Machine-learning guided synthesis, the use of artificial intelligence to accelerate the synthesis of materials by optimizing the synthesis process according to the prediction given by the well-trained machine learning model

REFERENCES

(1) Taché, K.; Jaffe, Y.; Craig, O. E.; Lucquin, A.; Zhou, J.; Wang, H.; Jiang, S.; Standall, E.; Flad, R. K. What Do "Barbarians" Eat? Integrating Ceramic Use-Wear and Residue Analysis in the Study of Food and Society at the Margins of Bronze Age China. *PLoS One* **2021**, *16* (4), No. e0250819.

(2) Tite, M. S. Ceramic Production, Provenance and Use—a Review. *Archaeometry* **2008**, *50* (2), 216−231.

(3) Lianghui, Q. A Preliminary Study of the Characteristics of Metallurgical Technology in Ancient China. In *Chinese Studies in the History and Philosophy of Science and Technology*; Dainian, F.; Cohen, R. S., Eds.; Springer: Netherlands, 1996; pp 219−241.

(4) Sakr, M.; Liu, S. A Comprehensive Review on Applications of Ohmic Heating (OH). *Renewable Sustainable Energy Rev.* **2014**, *39*, 262−269.

(5) Sun, J.; Wang, W.; Yue, Q. Review on Microwave-Matter Interaction Fundamentals and Efficient Microwave-Associated Heating Strategies. *Materials* **2016**, *9* (4), 231.

(6) Prokhorov, A. M. *Laser Heating of Metals*; CRC Press, 2018.

(7) Zhang, Z.; Chen, P.; Duan, X.; Zang, K.; Luo, J.; Duan, X. Robust Epitaxial Growth of Two-Dimensional Heterostructures, Multiheterostructures, and Superlattices. *Science* **2017**, *357* (6353), 788−792.

(8) Wu, Q.; Zhang, J.; Tang, L.; Khan, U.; Nong, H.; Zhao, S.; Sun, Y.; Zheng, R.; Zhang, R.; Wang, J.; et al. Iodine-Assisted Ultrafast Growth of High-Quality Monolayer MoS_2 with Sulfur-Terminated Edges. *Natl. Sci. Open* **2023**, *2* (4), 20230009.

(9) Wan, X.; Miao, X.; Yao, J.; Wang, S.; Shao, F.; Xiao, S.; Zhan, R.; Chen, K.; Zeng, X.; Gu, X.; et al. In Situ Ultrafast and Patterned Growth of Transition Metal Dichalcogenides from Inkjet-Printed Aqueous Precursors. *Adv. Mater.* **2021**, *33* (16), 2100260.

(10) Yao, Y.; Huang, Z.; Xie, P.; Lacey, S. D.; Jacob, R. J.; Xie, H.; Chen, F.; Nie, A.; Pu, T.; Rehwoldt, M.; et al. Carbothermal Shock Synthesis of High-Entropy-Alloy Nanoparticles. *Science* **2018**, *359* (6383), 1489−1494.

(11) Deng, B.; Wang, Z.; Chen, W.; Li, J. T.; Luong, D. X.; Carter, R. A.; Gao, G.; Yakobson, B. I.; Zhao, Y.; Tour, J. M. Phase Controlled Synthesis of Transition Metal Carbide Nanocrystals by Ultrafast Flash Joule Heating. *Nat. Commun.* **2022**, *13* (1), 262.

(12) Zhu, W.; Zhang, J.; Luo, J.; Zeng, C.; Su, H.; Zhang, J.; Liu, R.; Hu, E.; Liu, Y.; Liu, W.-D.; et al. Ultrafast Non-Equilibrium Synthesis of Cathode Materials for Li-Ion Batteries. *Adv. Mater.* **2023**, *35* (2), 2208974.

(13) Zhang, W.; Wei, X.; Wu, T.; Wei, F.; Ma, L.; Lv, Y.; Zhou, W.; Liu, H. Carbothermal Shock Enabled Functional Nanomaterials for Energy-Related Applications. *Nano Energy* **2023**, *118*, 108994.

(14) Dou, S.; Xu, J.; Cui, X.; Liu, W.; Zhang, Z.; Deng, Y.; Hu, W.; Chen, Y. High-Temperature Shock Enabled Nanomanufacturing for Energy-Related Applications. *Adv. Energy Mater.* **2020**, *10* (33), 2001331.

(15) Kang, T. J.; Kim, T.; Seo, S. M.; Park, Y. J.; Kim, Y. H. Thickness-Dependent Thermal Resistance of a Transparent Glass Heater with a Single-Walled Carbon Nanotube Coating. *Carbon* **2011**, *49* (4), 1087−1093.

(16) Miyamoto, Y.; Berber, S.; Yoon, M.; Rubio, A.; Tománek, D. Onset of Nanotube Decay under Extreme Thermal and Electronic Excitations. *Physica B* **2002**, *323* (1−4), 78−85.

(17) Wang, H.; Wang, H.; Zhang, S.; Zhang, Y.; Xia, K.; Yin, Z.; Zhang, M.; Liang, X.; Lu, H.; Li, S.; et al. Carbothermal Shock Enabled Facile and Fast Growth of Carbon Nanotubes in a Second. *Nano Research* **2022**, *15* (3), 2576−2581.

(18) Baloch, K. H.; Voskanian, N.; Bronsgeest, M.; Cumings, J. Remote Joule Heating by a Carbon Nanotube. *Nat. Nanotechnol.* **2012**, *7* (5), 316−319.

(19) Perebeinos, V.; Rotkin, S. V.; Petrov, A. G.; Avouris, P. The Effects of Substrate Phonon Mode Scattering on Transport in Carbon Nanotubes. *Nano Lett.* **2009**, *9* (1), 312−316.

(20) Xiong, G.; Jia, J.; Zhao, L.; Liu, X.; Zhang, X.; Liu, H.; Zhou, W. Non-Thermal Radiation Heating Synthesis of Nanomaterials. *Sci. Bull.* **2021**, *66* (4), 386−406.

(21) Chen, Y.; Egan, G. C.; Wan, J.; Zhu, S.; Jacob, R. J.; Zhou, W.; Dai, J.; Wang, Y.; Danner, V. A.; Yao, Y.; et al. Ultra-Fast Self-Assembly and Stabilization of Reactive Nanoparticles in Reduced Graphene Oxide Films. *Nat. Commun.* **2016**, *7* (1), 12332.

(22) Zou, J.; Zhang, X.; Xu, C.; Zhao, J.; Zhu, Y. T.; Li, Q. Soldering Carbon Nanotube Fibers by Targeted Electrothermal-Induced Carbon Deposition. *Carbon* **2017**, *121*, 242−247.

(23) Qiao, Y.; Yao, Y.; Liu, Y.; Chen, C.; Wang, X.; Zhong, G.; Liu, D.; Hu, L. Thermal Shock Synthesis of Nanocatalyst by 3D-Printed Miniaturized Reactors. *Small* **2020**, *16* (22), 2000509.

(24) Liu, L.; Aouraghe, M. A.; Xiao, S.; Wang, R.; Xu, F. Superior Stable, Highly Efficient, and Anisotropic Electrothermal Composite Heater in Various Directions with Fast Response Based on Aligned Carbon Nanotube Sheets. *Adv. Eng. Mater.* **2022**, *24* (12), 2200752.

(25) Stanford, M. G.; Bets, K. V.; Luong, D. X.; Advincula, P. A.; Chen, W.; Li, J. T.; Wang, Z.; McHugh, E. A.; Algozeeb, W. A.; Yakobson, B. I.; et al. Flash Graphene Morphologies. *ACS Nano* **2020**, *14* (10), 13691−13699.

(26) Yang, Y.; Ghildiyal, P.; Zachariah, M. R. Thermal Shock Synthesis of Metal Nanoclusters within On-the-Fly Graphene Particles. *Langmuir* **2019**, *35* (9), 3413−3420.

(27) Chen, Y.; Xu, S.; Li, Y.; Jacob, R. J.; Kuang, Y.; Liu, B.; Wang, Y.; Pastel, G.; Salamanca-Riba, L. G.; Zachariah, M. R.; et al. FeS_2 Nanoparticles Embedded in Reduced Graphene Oxide toward Robust, High-Performance Electrocatalysts. *Adv. Energy Mater.* **2017**, *7* (19), 1700482.

(28) Liang, Z.; Yao, Y.; Jiang, B.; Wang, X.; Xie, H.; Jiao, M.; Liang, C.; Qiao, H.; Kline, D.; Zachariah, M. R.; et al. 3D Printed Graphene-Based 3000 K Probe. *Adv. Funct. Mater.* **2021**, *31* (34), 2102994.

(29) Xu, X.; Du, Y.; Wang, C.; Guo, Y.; Zou, J.; Zhou, K.; Zeng, Z.; Liu, Y.; Li, L. High-Entropy Alloy Nanoparticles on Aligned Electronspun Carbon Nanofibers for Supercapacitors. *J. Alloy. Comp.* **2020**, *822*, 153642.

(30) Yao, Y.; Huang, Z.; Xie, P.; Wu, L.; Ma, L.; Li, T.; Pang, Z.; Jiao, M.; Liang, Z.; Gao, J.; et al. High Temperature Shockwave Stabilized Single Atoms. *Nat. Nanotechnol.* **2019**, *14* (9), 851−857.

(31) Zhong, G.; Xu, S.; Dong, Q.; Wang, X.; Hu, L. Rapid, Universal Surface Engineering of Carbon Materials via Microwave-Induced Carbothermal Shock. *Adv. Funct. Mater.* **2021**, *31* (18), 2010968.

https://doi.org/10.1021/acsnano.4c12350
ACS Nano XXXX, XXX, XXX−XXX

(32) Abdelhafiz, A.; Wang, B.; Harutyunyan, A. R.; Li, J. Carbothermal Shock Synthesis of High Entropy Oxide Catalysts: Dynamic Structural and Chemical Reconstruction Boosting the Catalytic Activity and Stability toward Oxygen Evolution Reaction. *Adv. Energy Mater.* **2022**, *12* (35), 2200742.
(33) Wang, X.; Huang, Z.; Yao, Y.; Qiao, H.; Zhong, G.; Pei, Y.; Zheng, C.; Kline, D.; Xia, Q.; Lin, Z.; et al. Continuous 2000%K Droplet-to-Particle Synthesis. *Mater. Today* **2020**, *35*, 106−114.
(34) Li, Y.; Gao, T.; Yao, Y.; Liu, Z.; Kuang, Y.; Chen, C.; Song, J.; Xu, S.; Hitz, E. M.; Liu, B.; et al. In Situ "Chainmail Catalyst" Assembly in Low-Tortuosity, Hierarchical Carbon Frameworks for Efficient and Stable Hydrogen Generation. *Adv. Energy Mater.* **2018**, *8* (25), 1801289.
(35) Begtrup, G. E.; Ray, K. G.; Kessler, B. M.; Yuzvinsky, T. D.; Garcia, H.; Zettl, A. Probing Nanoscale Solids at Thermal Extremes. *Phys. Rev. Lett.* **2007**, *99* (15), 155901.
(36) Chen, W.; Li, J. T.; Ge, C.; Yuan, Z.; Algozeeb, W. A.; Advincula, P. A.; Gao, G.; Chen, J.; Ling, K.; Choi, C. H.; et al. Turbostratic Boron-Carbon-Nitrogen and Boron Nitride by Flash Joule Heating. *Adv. Mater.* **2022**, *34* (33), 2202666.
(37) Wang, J.; Zhao, J.; Zhao, L.; Lu, Q.; Zhou, T.; Yong, Z.; Wang, P.; Zhang, X.; Li, Q. Interfacial-Bubbling-Induced Nondestructive Expansion to Reconstruct Superstrong and Multifunctional Carbon Nanotube Fibers. *Carbon* **2021**, *184*, 24−33.
(38) Xu, L.; Wang, H.; Wu, Y.; Wang, Z.; Wu, L.; Zheng, L. A One-Step Approach to Green and Scalable Production of Graphene Inks for Printed Flexible Film Heaters. *Mater. Chem. Front.* **2021**, *5* (4), 1895−1905.
(39) Barmpakos, D.; Belessi, V.; Xanthopoulos, N.; Krontiras, C. A.; Kaltsas, G. Flexible Inkjet-Printed Heaters Utilizing Graphene-Based Inks. *Sensors* **2022**, *22* (3), 1173.
(40) Li, H.; Zhu, H.; Zhang, S.; Zhang, N.; Du, M.; Chai, Y. Nano High-Entropy Materials: Synthesis Strategies and Catalytic Applications. *Small Struct.* **2020**, *1* (2), 2000033.
(41) Zheng, J.; Zhang, J.; Zhang, L.; Zhang, W.; Wang, X.; Cui, Z.; Song, H.; Liang, Z.; Du, L. Ultrafast Carbothermal Shock Constructing $Ni_3Fe_{1-x}Cr_x$ Intermetallic Integrated Electrodes for Efficient and Durable Overall Water Splitting. *ACS Appl. Mater. Interfaces* **2022**, *14* (17), 19524−19533.
(42) Song, J.-Y.; Kim, C.; Kim, M.; Cho, K. M.; Gereige, I.; Jung, W.-B.; Jeong, H.; Jung, H.-T. Generation of High-Density Nanoparticles in the Carbothermal Shock Method. *Sci. Adv.* **2021**, *7* (48), No. eabk2984.
(43) Liu, Y.; Tian, X.; Han, Y.-C.; Chen, Y.; Hu, W. High-Temperature Shock Synthesis of High-Entropy-Alloy Nanoparticles for Catalysis. *Chin. J. Catal.* **2023**, *48*, 66−89.
(44) Chen, S.; Qiu, X.; Zhang, B.; Xu, J.; Zhong, F.; Zhu, B.; Zhang, Y.; Ou-Yang, J.; Yang, X. Advances in Antioxidation Coating Materials for Carbon/Carbon Composites. *J. Alloys Compd.* **2021**, *886*, 161143.
(45) Li, Y.; Yang, M.; Xu, B.; Sun, Q.; Zhang, W.; Zhang, Y.; Meng, F. Synthesis, Structure and Antioxidant Performance of Boron Nitride (Hexagonal) Layers Coating on Carbon Nanotubes (Multi-Walled). *Appl. Surf. Sci.* **2018**, *450*, 284−291.
(46) Vázquez, E.; Prato, M. Carbon Nanotubes and Microwaves: Interactions, Responses, and Applications. *ACS Nano* **2009**, *3* (12), 3819−3824.
(47) Zhang, M.; Lei, D.; Yin, X.; Chen, L.; Li, Q.; Wang, Y.; Wang, T. Magnetite/Graphene Composites: Microwave Irradiation Synthesis and Enhanced Cycling and Rate Performances for Lithium Ion Batteries. *J. Mater. Chem.* **2010**, *20* (26), 5538−5543.
(48) Voiry, D.; Yang, J.; Kupferberg, J.; Fullon, R.; Lee, C.; Jeong, H. Y.; Shin, H. S.; Chhowalla, M. High-Quality Graphene via Microwave Reduction of Solution-Exfoliated Graphene Oxide. *Science* **2016**, *353* (6306), 1413−1416.
(49) Xu, S.; Zhong, G.; Chen, C.; Zhou, M.; Kline, D. J.; Jacob, R. J.; Xie, H.; He, S.; Huang, Z.; Dai, J.; et al. Uniform, Scalable, High-Temperature Microwave Shock for Nanoparticle Synthesis through Defect Engineering. *Matter* **2019**, *1* (3), 759−769.
(50) Wan, C.; Duan, X. Microwave Shock Synthesis beyond Thermodynamic Equilibrium. *Matter* **2019**, *1* (3), 555−557.
(51) Raghuveer, M. S.; Agrawal, S.; Bishop, N.; Ramanath, G. Microwave-Assisted Single-Step Functionalization and in Situ Derivatization of Carbon Nanotubes with Gold Nanoparticles. *Chem. Mater.* **2006**, *18* (6), 1390−1393.
(52) Kim, S. J.; Park, Y. J.; Ra, E. J.; Kim, K. K.; An, K. H.; Lee, Y. H.; Choi, J. Y.; Park, C. H.; Doo, S. K.; Park, M. H.; et al. Defect-Induced Loading of Pt Nanoparticles on Carbon Nanotubes. *Appl. Phys. Lett.* **2007**, *90* (2), 023114.
(53) Matovic, B.; Saponjic, A.; Devecerski, A.; Miljkovic, M. Fabrication of SiC by Carbothermal-Reduction Reactions of Diatomaceous Earth. *J. Mater. Sci.* **2007**, *42* (14), 5448−5451.
(54) Koepf, E. E.; Advani, S. G.; Prasad, A. K.; Steinfeld, A. Experimental Investigation of the Carbothermal Reduction of ZnO Using a Beam-Down, Gravity-Fed Solar Reactor. *Ind. Eng. Chem. Res.* **2015**, *54* (33), 8319−8332.
(55) Nakao, W.; Fukuyama, H.; Nagata, K. Gibbs Energy Change of Carbothermal Nitridation Reaction of Al_2O_3 to Form AlN and Reassessment of Thermochemical Properties of AlN. *J. Am. Ceram. Soc.* **2002**, *85* (4), 889−896.
(56) Shrestha, R.; Lee, K. M.; Chang, W. S.; Kim, D. S.; Rhee, G. H.; Choi, T. Y. Steady Heat Conduction-Based Thermal Conductivity Measurement of Single Walled Carbon Nanotubes Thin Film Using a Micropipette Thermal Sensor. *Rev. Sci. Instrum.* **2013**, *84* (3), 034901.
(57) Chen, S.; Nie, L.; Hu, X.; Zhang, Y.; Zhang, Y.; Yu, Y.; Liu, W. Ultrafast Sintering for Ceramic-Based All-Solid-State Lithium-Metal Batteries. *Adv. Mater.* **2022**, *34* (33), 2200430.
(58) Liao, Y.; Li, Y.; Zhao, R.; Zhang, J.; Zhao, L.; Ji, L.; Zhang, Z.; Liu, X.; Qin, G.; Zhang, X. High-Entropy-Alloy Nanoparticles with 21 Ultra-Mixed Elements for Efficient Photothermal Conversion. *Natl. Sci. Rev.* **2022**, *9* (6), nwac041.
(59) Dougakiuchi, T.; Ito, A.; Hitaka, M.; Fujita, K.; Yamanishi, M. Ultimate Response Time in Mid-Infrared High-Speed Low-Noise Quantum Cascade Detectors. *Appl. Phys. Lett.* **2021**, *118* (4), 041101.
(60) Grujić, K. A Review of Thermal Spectral Imaging Methods for Monitoring High-Temperature Molten Material Streams. *Sensors* **2023**, *23* (3), 1130.
(61) Xie, P.; Yao, Y.; Huang, Z.; Liu, Z.; Zhang, J.; Li, T.; Wang, G.; Shahbazian-Yassar, R.; Hu, L.; Wang, C. Highly Efficient Decomposition of Ammonia Using High-Entropy Alloy Catalysts. *Nat. Commun.* **2019**, *10* (1), 4011.
(62) Kume, H.; Koyama, K.; Nakatsugawa, K.; Suzuki, S.; Fatlowitz, D. Ultrafast Microchannel Plate Photomultipliers. *Appl. Opt.* **1988**, *27* (6), 1170−1178.
(63) Jacob, R. J.; Kline, D. J.; Zachariah, M. R. High Speed 2-Dimensional Temperature Measurements of Nanothermite Composites: Probing Thermal vs. Gas Generation Effects. *J. Appl. Phys.* **2018**, *123* (11), 115902.
(64) Luo, J.; Lu, H.; Zhang, Q.; Yao, Y.; Chen, M.; Li, Q. Flexible Carbon Nanotube/Polyurethane Electrothermal Films. *Carbon* **2016**, *110*, 343−349.
(65) Ilanchezhiyan, P.; Zakirov, A. S.; Kumar, G. M.; Yuldashev, S. U.; Cho, H. D.; Kang, T. W.; Mamadalimov, A. T. Highly Efficient CNT Functionalized Cotton Fabrics for Flexible/Wearable Heating Applications. *RSC Adv.* **2015**, *5* (14), 10697−10702.
(66) Harutyunyan, A. R.; Pradhan, B. K.; Chang, J.; Chen, G.; Eklund, P. C. Purification of Single-Wall Carbon Nanotubes by Selective Microwave Heating of Catalyst Particles. *J. Phys. Chem. B* **2002**, *106* (34), 8671−8675.
(67) Zou, J.; Zhang, X.; Zhao, J.; Lei, C.; Zhao, Y.; Zhu, Y.; Li, Q. Strengthening and Toughening Effects by Strapping Carbon Nanotube Cross-Links with Polymer Molecules. *Compos. Sci. Technol.* **2016**, *135*, 123−127.
(68) Schniepp, H. C.; Li, J.-L.; McAllister, M. J.; Sai, H.; Herrera-Alonso, M.; Adamson, D. H.; Prud'homme, R. K.; Car, R.; Saville, D. A.; Aksay, I. A. Functionalized Single Graphene Sheets Derived from Splitting Graphite Oxide. *J. Phys. Chem. B* **2006**, *110* (17), 8535−8539.
(69) Li, X.; Zhang, G.; Bai, X.; Sun, X.; Wang, X.; Wang, E.; Dai, H. Highly Conducting Graphene Sheets and Langmuir-Blodgett Films. *Nat. Nanotechnol.* **2008**, *3* (9), 538−542.

https://doi.org/10.1021/acsnano.4c12350
ACS Nano XXXX, XXX, XXX−XXX

(70) Hettler, S.; Sebastian, D.; Pelaez-Fernandez, M.; Benito, A. M.; Maser, W. K.; Arenal, R. In-Situ Reduction by Joule Heating and Measurement of Electrical Conductivity of Graphene Oxide in a Transmission Electron Microscope. *2D Mater.* **2021**, *8* (3), 031001.
(71) Bazargan, A. M.; Sharif, F.; Mazinani, S.; Naderi, N. Highly Conductive Reduced Graphene Oxide Transparent Ultrathin Film through Joule-Heat Induced Direct Reduction. *J. Mater. Sci- Mater. El.* **2017**, *28* (2), 1419−1427.
(72) Dong, L.; Yang, J.; Chhowalla, M.; Loh, K. P. Synthesis And Reduction of Large Sized Graphene Oxide Sheets. *Chem. Soc. Rev.* **2017**, *46* (23), 7306−7316.
(73) Ko, J. S.; Meng, P. Y.; Elazar-Mittelman, H.; Johnson, J. K.; Xia, Z.; Holdren, S. Rapid Carbothermal Shock Enhances the Double-Layer Response of Graphene Oxide-Carbon Nanotube Electrodes. *Energy Fuels* **2021**, *35* (21), 17919−17929.
(74) Wang, Y.; Chen, Y.; Lacey, S. D.; Xu, L.; Xie, H.; Li, T.; Danner, V. A.; Hu, L. Reduced Graphene Oxide Film with Record-High Conductivity and Mobility. *Mater. Today* **2018**, *21* (2), 186−192.
(75) Yao, P.; Chen, P.; Jiang, L.; Zhao, H.; Zhu, H.; Zhou, D.; Hu, W.; Han, B.-H.; Liu, M. Electric Current Induced Reduction of Graphene Oxide and Its Application as Gap Electrodes in Organic Photoswitching Devices. *Adv. Mater.* **2010**, *22* (44), 5008−5012.
(76) Ekiz, O. Ö.; Ürel, M.; Güner, H.; Mizrak, A. K.; Dâna, A. Reversible Electrical Reduction and Oxidation of Graphene Oxide. *ACS Nano* **2011**, *5* (4), 2475−2482.
(77) Jakhar, R.; Yap, J. E.; Joshi, R. Microwave Reduction of Graphene Oxide. *Carbon* **2020**, *170*, 277−293.
(78) Tang, S.; Jin, S.; Zhang, R.; Liu, Y.; Wang, J.; Hu, Z.; Lu, W.; Yang, S.; Qiao, W.; Ling, L.; et al. Effective Reduction of Graphene Oxide via a Hybrid Microwave Heating Method by Using Mildly Reduced Graphene Oxide as a Susceptor. *Appl. Surf. Sci.* **2019**, *473*, 222−229.
(79) Barman, B. K.; Nanda, K. K. Ultrafast-Versatile-Domestic-Microwave-Oven Based Graphene Oxide Reactor for the Synthesis of Highly Efficient Graphene Based Hybrid Electrocatalysts. *ACS Sustainable Chem. Eng.* **2018**, *6* (3), 4037−4045.
(80) Li, Z.; Yao, Y.; Lin, Z.; Moon, K.-S.; Lin, W.; Wong, C. Ultrafast, Dry Microwave Synthesis of Graphene Sheets. *J. Mater. Chem.* **2010**, *20* (23), 4781−4783.
(81) Park, O.-K.; Kim, N. H.; Lee, J. H. Rapid Effective Reduction by Microwave-Irradiated Thermal Reaction for Large-Scale Production of High-Quality Reduced Graphene Oxide. *Carbon* **2022**, *187*, 330−337.
(82) López, V.; Sundaram, R. S.; Gómez-Navarro, C.; Olea, D.; Burghard, M.; Gómez-Herrero, J.; Zamora, F.; Kern, K. Chemical Vapor Deposition Repair of Graphene Oxide: A Route to Highly-Conductive Graphene Monolayers. *Adv. Mater.* **2009**, *21* (46), 4683−4686.
(83) Wu, J.; Zhao, J.; Vaidhyanathan, B.; Zhang, H.; Anshuman, A.; Nare, A.; Saremi-Yarahmadi, S. Rapid Microwave-Assisted Bulk Production of High-Quality Reduced Graphene Oxide for Lithium Ion Batteries. *Materialia* **2020**, *13*, 100833.
(84) Chen, Y.; Fu, K.; Zhu, S.; Luo, W.; Wang, Y.; Li, Y.; Hitz, E.; Yao, Y.; Dai, J.; Wan, J.; et al. Reduced Graphene Oxide Films with Ultrahigh Conductivity as Li-Ion Battery Current Collectors. *Nano Lett.* **2016**, *16* (6), 3616−3623.
(85) Liu, Y.; Li, P.; Wang, F.; Fang, W.; Xu, Z.; Gao, W.; Gao, C. Rapid Roll-To-Roll Production of Graphene Films Using Intensive Joule Heating. *Carbon* **2019**, *155*, 462−468.
(86) Chen, W.; Wang, Z.; Bets, K. V.; Luong, D. X.; Ren, M.; Stanford, M. G.; McHugh, E. A.; Algozeeb, W. A.; Guo, H.; Gao, G.; et al. Millisecond Conversion of Metastable 2D Materials by Flash Joule Heating. *ACS Nano* **2021**, *15* (1), 1282−1290.
(87) Gao, G.; Jiao, Y.; Ma, F.; Jiao, Y.; Waclawik, E.; Du, A. Charge Mediated Semiconducting-to-Metallic Phase Transition in Molybdenum Disulfide Monolayer and Hydrogen Evolution Reaction in New 1T' Phase. *J. Phys. Chem. C* **2015**, *119* (23), 13124−13128.
(88) Son, M.; Park, J.; Im, E.; Ryu, J. H.; Durmus, Y. E.; Eichel, R.-A.; Kang, S. J. Sacrificial Catalyst of Carbothermal-Shock-Synthesized 1T-MoS_2 Layers for Ultralong-Lifespan Seawater Battery. *Nano Lett.* **2023**, *23* (1), 344−352.
(89) Upama, S.; Mikhalchan, A.; Arévalo, L.; Rana, M.; Pendashteh, A.; Green, M. J.; Vilatela, J. J. Processing of Composite Electrodes of Carbon Nanotube Fabrics and Inorganic Matrices via Rapid Joule Heating. *ACS Appl. Mater. Interfaces* **2023**, *15* (4), 5590−5599.
(90) Shi, W.; Li, Z.; Gong, Z.; Liang, Z.; Liu, H.; Han, Y.-C.; Niu, H.; Song, B.; Chi, X.; Zhou, J.; et al. Transient and General Synthesis of High-Density and Ultrasmall Nanoparticles on Two-Dimensional Porous Carbon via Coordinated Carbothermal Shock. *Nat. Commun.* **2023**, *14* (1), 2294.
(91) Liu, Q.; Chen, S. W. Ultrafast Synthesis of Electrocatalysts. *Trends Chem.* **2022**, *4* (10), 918−934.
(92) Kim, C.; Song, J.-Y.; Choi, C.; Ha, J. P.; Lee, W.; Nam, Y. T.; Lee, D.-m.; Kim, G.; Gereige, I.; Jung, W.-B.; et al. Atomic-Scale Homogeneous Ru-Cu Alloy Nanoparticles for Highly Efficient Electrocatalytic Nitrogen Reduction. *Adv. Mater.* **2022**, *34* (40), 2205270.
(93) Chen, Y.; Li, Y.; Wang, Y.; Fu, K.; Danner, V. A.; Dai, J.; Lacey, S. D.; Yao, Y.; Hu, L. Rapid, in Situ Synthesis of High Capacity Battery Anodes through High Temperature Radiation-Based Thermal Shock. *Nano Lett.* **2016**, *16* (9), 5553−5558.
(94) Yao, Y.; Huang, Z.; Xie, P.; Li, T.; Lacey, S. D.; Jiao, M.; Xie, H.; Fu, K. K.; Jacob, R. J.; Kline, D. J.; et al. Ultrafast, Controllable Synthesis of Sub-Nano Metallic Clusters through Defect Engineering. *ACS Appl. Mater. Interfaces* **2019**, *11* (33), 29773−29779.
(95) Han, Y.-C.; Liu, M.-L.; Sun, L.; Li, S.; Li, G.; Song, W.-S.; Wang, Y.-J.; Nan, Z.-A.; Ding, S.-Y.; Liao, H.-G.; et al. A general method for rapid synthesis of refractory carbides by low-pressure carbothermal shock reduction. *Proc. Natl. Acad. Sci. U.S.A.* **2022**, *119* (37), No. e2121848119.
(96) Chen, W.; Li, J. T.; Ge, C.; Yuan, Z.; Algozeeb, W. A.; Advincula, P. A.; Gao, G.; Chen, J.; Ling, K.; Choi, C. H.; et al. Turbostratic Boron-Carbon-Nitrogen and Boron Nitride by Flash Joule Heating. *Adv. Mater.* **2022**, *34* (33), 2202666.
(97) Hassine, N. A.; Binner, J. G. P.; Cross, T. E. Synthesis of Refractory Metal Carbide Powders via Microwave Carbothermal Reduction. *Int. J. Refract. Met. H.* **1995**, *13* (6), 353−358.
(98) Ryu, J. H.; Park, J.; Park, J.; Mun, J.; Im, E.; Lee, H.; Hong, S. Y.; An, K.; Lee, G.; Kim, Y.; et al. Carbothermal Shock-Induced Bifunctional Pt-Co Alloy Electrocatalysts for High-Performance Seawater Batteries. *Energy Storage Mater.* **2022**, *45*, 281−290.
(99) Chen, Y.; Zhao, Y.; Zhao, Z.; Liu, Y. Highly Dispersed Face-Centered Cubic Copper-Cobalt Alloys Constructed by Ultrafast Carbothermal Shock for Efficient Electrocatalytic Nitrate-to-Ammonia Conversion. *Mater. Today Energy* **2022**, *29*, 101112.
(100) Qiu, Y.; Hu, Z.; Li, H.; Ren, Q.; Chen, Y.; Hu, S. Hybrid Electrocatalyst Ag/Co/C via Flash Joule Heating for Oxygen Reduction Reaction in Alkaline Media. *Chem. Eng. J.* **2022**, *430*, 132769.
(101) Wei, W.; Li, P.; Lu, F.; Fan, K.; Li, B.; Wei, Y.; Zong, L.; Wang, L. Loading Uniformly Distributed CuRu Alloys on Carbon Nanotubes via Flash Joule Heating for High-Performance Electrocatalytic Water Splitting. *J. Alloy. Comp.* **2023**, *936*, 168349.
(102) Li, M.; Hu, Z.; Li, H.; Zhao, W.; Zhou, W.; Yang, Q.; Hu, S. Pt-Ni Alloy Nanoparticles via High-Temperature Shock as Efficient Electrocatalysts in the Oxygen Reduction Reaction. *ACS Appl. Nano Mater.* **2022**, *5* (6), 8243−8250.
(103) Zhang, Z.; Liu, Y.; Su, X.; Zhao, Z.; Mo, Z.; Wang, C.; Zhao, Y.; Chen, Y.; Gao, S. Electro-Triggered Joule Heating Method to Synthesize Single-Phase CuNi Nano-Alloy Catalyst for Efficient Electrocatalytic Nitrate Reduction toward Ammonia. *Nano Res.* **2023**, *16* (5), 6632−6641.
(104) Zhang, H.; Qi, S.; Zhu, K.; Wang, H.; Zhang, G.; Ma, W.; Zong, X. Ultrafast Synthesis of Mo_2C-Based Catalyst by Joule Heating towards Electrocatalytic Hydrogen Evolution Reaction. *Symmetry* **2023**, *15* (4), 801.
(105) Abrahamson, J. Graphite Sublimation Temperatures, Carbon Arcs and Crystallite Erosion. *Carbon* **1974**, *12* (2), 111−141.

https://doi.org/10.1021/acsnano.4c12350
ACS Nano XXXX, XXX, XXX−XXX

(106) Yao, Y.; Huang, Z.; Hughes, L. A.; Gao, J.; Li, T.; Morris, D.; Zeltmann, S. E.; Savitzky, B. H.; Ophus, C.; Finfrock, Y. Z.; et al. Extreme Mixing in Nanoscale Transition Metal Alloys. *Matter* **2021**, *4* (7), 2340−2353.
(107) Qiao, H.; Saray, M. T.; Wang, X.; Xu, S.; Chen, G.; Huang, Z.; Chen, C.; Zhong, G.; Dong, Q.; Hong, M.; et al. Scalable Synthesis of High Entropy Alloy Nanoparticles by Microwave Heating. *ACS Nano* **2021**, *15* (9), 14928−14937.
(108) Hume-Rothery, W. The Structure of Metals and Alloys. *Indian J. Phys.* **1969**, *11*, 74−74.
(109) Troparevsky, M. C.; Morris, J. R.; Kent, P. R. C.; Lupini, A. R.; Stocks, G. M. Criteria for Predicting the Formation of Single-Phase High-Entropy Alloys. *Phys. Rev. X* **2015**, *5* (1), 011041.
(110) Wu, D.; Kusada, K.; Yamamoto, T.; Toriyama, T.; Matsumura, S.; Kawaguchi, S.; Kubota, Y.; Kitagawa, H. Platinum-Group-Metal High-Entropy-Alloy Nanoparticles. *J. Am. Chem. Soc.* **2020**, *142* (32), 13833−13838.
(111) Yang, P.; Liu, Y.; Zhao, X.; Cheng, J.; Li, H. Electromagnetic Wave Absorption Properties of $FeCoNiCrAl_{0.8}$ High Entropy Alloy Powders and its Amorphous Structure Prepared by High-Energy Ball Milling. *J. Mater. Res.* **2016**, *31* (16), 2398−2406.
(112) Tsai, M.-H.; Yuan, H.; Cheng, G.; Xu, W.; Tsai, K.-Y.; Tsai, C.-W.; Jian, W. W.; Juan, C.-C.; Shen, W.-J.; Chuang, M.-H.; et al. Morphology, Structure and Composition of Precipitates in $Al_{0.3}CoCrCu_{0.5}FeNi$ High-Entropy Alloy. *Intermetallics* **2013**, *32*, 329−336.
(113) Islam, N.; Huang, W.; Zhuang, H. L. Machine Learning for Phase Selection in Multi-Principal Element Alloys. *Comput. Mater. Sci.* **2018**, *150*, 230−235.
(114) Rost, C. M.; Sachet, E.; Borman, T.; Moballegh, A.; Dickey, E. C.; Hou, D.; Jones, J. L.; Curtarolo, S.; Maria, J.-P. Entropy-Stabilized Oxides. *Nat. Commun.* **2015**, *6* (1), 8485.
(115) Yu, L.; Zeng, K.; Li, C.; Lin, X.; Liu, H.; Shi, W.; Qiu, H.-J.; Yuan, Y.; Yao, Y. High-Entropy Alloy Catalysts: From Bulk to Nano toward Highly Efficient Carbon and Nitrogen Catalysis. *Carbon Energy* **2022**, *4* (5), 731−761.
(116) Liu, Y.; Chen, Z.; Yang, X.; Zhang, J.; Sun, Z.; Chen, Y.; Liu, F. High Entropy Nanoparticles of CoCrXFeNi (X = Al, Cu, Mn) Loaded on Activated Carbon for Efficient Degradation of Methylene Blue. *J. Mater. Res. Technol.* **2021**, *15*, 256−267.
(117) Minamihara, H.; Kusada, K.; Wu, D.; Yamamoto, T.; Toriyama, T.; Matsumura, S.; Kumara, L. S. R.; Ohara, K.; Sakata, O.; Kawaguchi, S.; et al. Continuous-Flow Reactor Synthesis for Homogeneous 1 nm-Sized Extremely Small High-Entropy Alloy Nanoparticles. *J. Am. Chem. Soc.* **2022**, *144* (26), 11525−11529.
(118) Wang, C.; Ping, W.; Bai, Q.; Cui, H.; Hensleigh, R.; Wang, R.; Brozena, A. H.; Xu, Z.; Dai, J.; Pei, Y.; et al. A General Method to Synthesize and Sinter Bulk Ceramics in Seconds. *Science* **2020**, *368* (6490), 521−526.
(119) Lu, Q.; Wu, H.; Zheng, X.; Cao, Y.; Li, J.; Wang, Y.; Wang, H.; Zhi, C.; Deng, Y.; Han, X.; et al. Controllable Constructing Janus Homologous Heterostructures of Transition Metal Alloys/Sulfides for Efficient Oxygen Electrocatalysis. *Adv. Energy Mater.* **2022**, *12* (42), 2202215.
(120) Yang, C.; Cui, M.; Li, N.; Liu, Z.; Hwang, S.; Xie, H.; Wang, X.; Kuang, Y.; Jiao, M.; Su, D.; et al. In Situ Iron Coating on Nanocatalysts for Efficient and Durable Oxygen Evolution Reaction. *Nano Energy* **2019**, *63*, 103855.
(121) Luo, Z.; Wang, X.; Cui, B.; Luo, H.; Zhang, T.; Ding, J.; Chen, Y.; Deng, Y.; Hu, W. A Universal and Ultrafast Method for Fabricating a Library of Nanocellulose-Supported Metal Nanoparticles. *Prog. Nat. Sci. - Mater.* **2024**, *34* (2), 389−395.
(122) Li, S.; Tang, X.; Jia, H.; Li, H.; Xie, G.; Liu, X.; Lin, X.; Qiu, H.-J. Nanoporous High-Entropy Alloys with Low Pt Loadings for High-Performance Electrochemical Oxygen Reduction. *J. Catal.* **2020**, *383*, 164−171.
(123) Sharma, L.; Katiyar, N. K.; Parui, A.; Das, R.; Kumar, R.; Tiwary, C. S.; Singh, A. K.; Halder, A.; Biswas, K. Low-Cost High Entropy Alloy (HEA) for High-Efficiency Oxygen Evolution Reaction (OER). *Nano Res.* **2022**, *15* (6), 4799−4806.
(124) Wu, D.; Kusada, K.; Yamamoto, T.; Toriyama, T.; Matsumura, S.; Gueye, I.; Seo, O.; Kim, J.; Hiroi, S.; Sakata, O.; et al. On the Electronic Structure and Hydrogen Evolution Reaction Activity of Platinum Group Metal-Based High-Entropy-Alloy Nanoparticles. *Chem. Sci.* **2020**, *11* (47), 12731−12736.
(125) Nellaiappan, S.; Katiyar, N. K.; Kumar, R.; Parui, A.; Malviya, K. D.; Pradeep, K. G.; Singh, A. K.; Sharma, S.; Tiwary, C. S.; Biswas, K. High-Entropy Alloys as Catalysts for the CO2 and CO Reduction Reactions: Experimental Realization. *ACS Catal.* **2020**, *10* (6), 3658−3663.
(126) Ai, Y.; He, M.-Q.; Sun, H.; Jia, X.; Wu, L.; Zhang, X.; Sun, H.-b.; Liang, Q. Ultra-Small High-Entropy Alloy Nanoparticles: Efficient Nanozyme for Enhancing Tumor Photothermal Therapy. *Adv. Mater.* **2023**, *35* (23), 2302335.
(127) Wang, A.; Li, J.; Zhang, T. Heterogeneous Single-Atom Catalysis. *Nat. Rev. Chem.* **2018**, *2* (6), 65−81.
(128) Peng, Y.; Lu, B.; Chen, S. Carbon-Supported Single Atom Catalysts for Electrochemical Energy Conversion and Storage. *Adv. Mater.* **2018**, *30* (48), 1801995.
(129) Shang, Y.; Xu, X.; Gao, B.; Wang, S.; Duan, X. Single-Atom Catalysis in Advanced Oxidation Processes for Environmental Remediation. *Chem. Soc. Rev.* **2021**, *50* (8), 5281−5322.
(130) Zhang, X.; Li, G.; Chen, G.; Wu, D.; Zhou, X.; Wu, Y. Single-Atom Nanozymes: A Rising Star for Biosensing and Biomedicine. *Coordin. Chem. Rev.* **2020**, *418*, 213376.
(131) He, G.; Yan, M.; Gong, H.; Fei, H.; Wang, S. Ultrafast Synthetic Strategies under Extreme Heating Conditions toward Single-Atom Catalysts. *Int. J. Extreme Manuf.* **2022**, *4* (3), 032003.
(132) Jiang, D.; Yao, Y.; Li, T.; Wan, G.; Pereira-Hernández, X. I.; Lu, Y.; Tian, J.; Khivantsev, K.; Engelhard, M. H.; Sun, C.; et al. Tailoring the Local Environment of Platinum in Single-Atom Pt_1/CeO_2 Catalysts for Robust Low-Temperature CO Oxidation. *Angew. Chem.* **2021**, *133* (50), 26258−26266.
(133) Lu, Q.; Wu, H.; Zheng, X.; Chen, Y.; Rogach, A. L.; Han, X.; Deng, Y.; Hu, W. Encapsulating Cobalt Nanoparticles in Interconnected N-Doped Hollow Carbon Nanofibers with Enriched Co-N-C Moiety for Enhanced Oxygen Electrocatalysis in Zn-Air Batteries. *Adv. Sci.* **2021**, *8* (20), 2101438.
(134) Du, J.; Wu, G.; Liang, K.; Yang, J.; Zhang, Y.; Lin, Y.; Zheng, X.; Yu, Z.-Q.; Wu, Y.; Hong, X. Rapid Controllable Synthesis of Atomically Dispersed Co on Carbon under High Voltage within One Minute. *Small* **2021**, *17* (6), 2007264.
(135) Ji, S.; Chen, Y.; Wang, X.; Zhang, Z.; Wang, D.; Li, Y. Chemical Synthesis of Single Atomic Site Catalysts. *Chem. Rev.* **2020**, *120* (21), 11900−11955.
(136) Xing, L.; Jin, Y.; Weng, Y.; Feng, R.; Ji, Y.; Gao, H.; Chen, X.; Zhang, X.; Jia, D.; Wang, G. Top-Down Synthetic Strategies toward Single Atoms on the Rise. *Matter* **2022**, *5* (3), 788−807.
(137) Zhang, Z.; Feng, C.; Liu, C.; Zuo, M.; Qin, L.; Yan, X.; Xing, Y.; Li, H.; Si, R.; Zhou, S.; et al. Electrochemical Deposition as a Universal Route for Fabricating Single-Atom Catalysts. *Nat. Commun.* **2020**, *11* (1), 1215.
(138) Xing, L.; Liu, R.; Gong, Z.; Liu, J.; Liu, J.; Gong, H.; Huang, K.; Fei, H. Ultrafast Joule Heating Synthesis of Hierarchically Porous Graphene-Based Co-N-C Single-Atom Monoliths. *Nano Res.* **2022**, *15* (5), 3913−3919.
(139) Lal, M. S.; Sundara, R. High Entropy Oxides—A Cost-Effective Catalyst for the Growth of High Yield Carbon Nanotubes and Their Energy Applications. *ACS Appl. Mater. Interfaces* **2019**, *11* (34), 30846−30857.
(140) Lee, J. M.; Jeong, H. Y.; Park, W. I. Large-Scale Synthesis of Graphene Films by Joule-Heating-Induced Chemical Vapor Deposition. *J. Electron. Mater.* **2010**, *39* (10), 2190−2195.
(141) Huang, L.; Chang, Q. H.; Guo, G. L.; Liu, Y.; Xie, Y. Q.; Wang, T.; Ling, B.; Yang, H. F. Synthesis of High-Quality Graphene Films on Nickel Foils by Rapid Thermal Chemical Vapor Deposition. *Carbon* **2012**, *50* (2), 551−556.

https://doi.org/10.1021/acsnano.4c12350
ACS Nano XXXX, XXX, XXX−XXX

(142) Kobayashi, T.; Bando, M.; Kimura, N.; Shimizu, K.; Kadono, K.; Umezu, N.; Miyahara, K.; Hayazaki, S.; Nagai, S.; Mizuguchi, Y.; et al. Production of a 100-M-Long High-Quality Graphene Transparent Conductive Film by Roll-To-Roll Chemical Vapor Deposition and Transfer Process. *Appl. Phys. Lett.* **2013**, *102* (2), 023112.
(143) Luong, D. X.; Bets, K. V.; Algozeeb, W. A.; Stanford, M. G.; Kittrell, C.; Chen, W.; Salvatierra, R. V.; Ren, M.; McHugh, E. A.; Advincula, P. A.; et al. Gram-Scale Bottom-Up Flash Graphene Synthesis. *Nature* **2020**, *577* (7792), 647−651.
(144) Zhu, S.; Zhang, F.; Lu, H.-G.; Sheng, J.; Wang, L.; Li, S.-D.; Han, G.; Li, Y. Flash Nitrogen-Doped Graphene for High-Rate Supercapacitors. *ACS Mater. Lett.* **2022**, *4* (10), 1863−1871.
(145) Zhou, C.; Zhang, K.; Sun, X.; Zhao, X.; Zheng, K.; Mi, J.; Qing, F.; Wen, Q.; Li, X. Porous Graphene Produced by Carbothermal Shock for Green Electromagnetic Interference Shielding in Both Microwave and Terahertz Bands. *Small Methods* **2023**, *7* (3), 2201493.
(146) Advincula, P. A.; Luong, D. X.; Chen, W.; Raghuraman, S.; Shahsavari, R.; Tour, J. M. Flash Graphene from Rubber Waste. *Carbon* **2021**, *178*, 649−656.
(147) Barbhuiya, N. H.; Kumar, A.; Singh, A.; Chandel, M. K.; Arnusch, C. J.; Tour, J. M.; Singh, S. P. The Future of Flash Graphene for the Sustainable Management of Solid Waste. *ACS Nano* **2021**, *15* (10), 15461−15470.
(148) Algozeeb, W. A.; Savas, P. E.; Luong, D. X.; Chen, W.; Kittrell, C.; Bhat, M.; Shahsavari, R.; Tour, J. M. Flash Graphene from Plastic Waste. *ACS Nano* **2020**, *14* (11), 15595−15604.
(149) Wyss, K. M.; Beckham, J. L.; Chen, W.; Luong, D. X.; Hundi, P.; Raghuraman, S.; Shahsavari, R.; Tour, J. M. Converting Plastic Waste Pyrolysis Ash into Flash Graphene. *Carbon* **2021**, *174*, 430−438.
(150) Wyss, K. M.; Chen, W.; Beckham, J. L.; Savas, P. E.; Tour, J. M. Holey and Wrinkled Flash Graphene from Mixed Plastic Waste. *ACS Nano* **2022**, *16* (5), 7804−7815.
(151) Wyss, K. M.; De Kleine, R. D.; Couvreur, R. L.; Kiziltas, A.; Mielewski, D. F.; Tour, J. M. Upcycling End-of-Life Vehicle Waste Plastic into Flash Graphene. *Commun. Eng.* **2022**, *1* (1), 3.
(152) Wyss, K. M.; Wang, Z.; Alemany, L. B.; Kittrell, C.; Tour, J. M. Bulk Production of Any Ratio ^{12}C:^{13}C Turbostratic Flash Graphene and Its Unusual Spectroscopic Characteristics. *ACS Nano* **2021**, *15* (6), 10542−10552.
(153) Chen, W.; Ge, C.; Li, J. T.; Beckham, J. L.; Yuan, Z.; Wyss, K. M.; Advincula, P. A.; Eddy, L.; Kittrell, C.; Chen, J.; et al. Heteroatom-Doped Flash Graphene. *ACS Nano* **2022**, *16* (4), 6646−6656.
(154) Eddy, L.; Xu, S.; Liu, C.; Scotland, P.; Chen, W.; Beckham, J. L.; Damasceno, B.; Choi, C. H.; Silva, K.; Lathem, A.; et al. Electric Field Effects in Flash Joule Heating Synthesis. *J. Am. Chem. Soc.* **2024**, *146* (23), 16010−16019.
(155) Arvidsson, R.; Kushnir, D.; Sandén, B. A.; Molander, S. Prospective Life Cycle Assessment of Graphene Production by Ultrasonication and Chemical Reduction. *Environ. Sci. Technol.* **2014**, *48* (8), 4529−4536.
(156) Cossutta, M.; McKechnie, J.; Pickering, S. J. A Comparative LCA of Different Graphene Production Routes. *Green Chem.* **2017**, *19* (24), 5874−5884.
(157) Arvidsson, R.; Kushnir, D.; Molander, S.; Sandén, B. A. Energy and Resource Use Assessment of Graphene as a Substitute for Indium Tin Oxide in Transparent Electrodes. *J. Cleaner Prod.* **2016**, *132*, 289−297.
(158) Ferronato, N.; Torretta, V. Waste Mismanagement in Developing Countries: A Review of Global Issues. *Int. J. Environ. Res. Public Health* **2019**, *16* (6), 1060.
(159) Vitorino de Souza Melaré, A.; Montenegro González, S.; Faceli, K.; Casadei, V. Technologies and Decision Support Systems to Aid Solid-Waste Management: A Systematic Review. *Waste Manage.* **2017**, *59*, 567−584.
(160) Noor, T.; Javid, A.; Hussain, A.; Bukhari, S. M.; Ali, W.; Akmal, M.; Hussain, S. M. Chapter 14 - Types, sources and management of urban wastes. In *Urban Ecology*; Verma, P.; Singh, P.; Singh, R.; Raghubanshi, A. S., Eds.; Elsevier: Amsterdam, 2020; pp 239−263.
(161) Kaza, S.; Yao, L.; Bhada-Tata, P.; Van Woerden, F. *What a Waste 2.0: A Global Snapshot of Solid Waste Management to 2050*; World Bank Group Publications: Washington, DC, 2018.
(162) Desa, U. World Urbanization Prospects, the 2011 Revision. *Population Division, department of economic and social affairs*; United Nations Secretariat: New York, 2014.
(163) Jerin, D. T.; Sara, H. H.; Radia, M. A.; Hema, P. S.; Hasan, S.; Urme, S. A.; Audia, C.; Hasan, M. T.; Quayyum, Z. An Overview of Progress towards Implementation of Solid Waste Management Policies in Dhaka, Bangladesh. *Heliyon* **2022**, *8* (2), No. e08918.
(164) D'Adamo, I.; Gastaldi, M.; Rosa, P. Recycling of End-Of-Life Vehicles: Assessing Trends and Performances in Europe. *Technol. Forecasting Social Change* **2020**, *152*, 119887.
(165) Advincula, P. A.; Granja, V.; Wyss, K. M.; Algozeeb, W. A.; Chen, W.; Beckham, J. L.; Luong, D. X.; Higgs, C. F.; Tour, J. M. Waste Plastic- and Coke-Derived Flash Graphene as Lubricant Additives. *Carbon* **2023**, *203*, 876−885.
(166) Saadi, M. A. S. R.; Advincula, P. A.; Thakur, M. S. H.; Khater, A. Z.; Saad, S.; Shayesteh Zeraati, A.; Nabil, S. K.; Zinke, A.; Roy, S.; Lou, M. Sustainable Valorization of Asphaltenes via Flash Joule Heating. *Sci. Adv.* **2022**, *8* (46), No. eadd3555.
(167) Jia, C.; Pang, M.; Lu, Y.; Liu, Y.; Zhuang, M.; Liu, B.; Lu, J.; Wei, T.; Wang, L.; Bian, T.; et al. Graphene Environmental Footprint Greatly Reduced When Derived from Biomass Waste via Flash Joule Heating. *One Earth* **2022**, *5* (12), 1394−1403.
(168) Liao, Y.; Zhu, R.; Zhang, W.; Huang, P.; Sun, Y.; Zhu, H. Ultrafast Synthesis of 3D Porous Flash Graphene and Its Adsorption Properties. *Colloid. Surfaces A* **2023**, *676*, 132178.
(169) Gómez-Sanabria, A.; Höglund-Isaksson, L.; Rafaj, P.; Schöpp, W. Carbon in Global Waste and Wastewater Flows - Its Potential as Energy Source under Alternative Future Waste Management Regimes. *Adv. Geosci.* **2018**, *45*, 105−113.
(170) Beyene, H. D.; Werkneh, A. A.; Ambaye, T. G. Current Updates on Waste to Energy (WtE) Technologies: A Review. *Renew. Energy Focus* **2018**, *24*, 1−11.
(171) Davoli, E.; Gangai, M. L.; Morselli, L.; Tonelli, D. Characterisation of Odorants Emissions from Landfills by SPME and GC/MS. *Chemosphere* **2003**, *51* (5), 357−368.
(172) Fang, J.-J.; Yang, N.; Cen, D.-Y.; Shao, L.-M.; He, P.-J. Odor Compounds from Different Sources of Landfill: Characterization and Source Identification. *Waste Manage* **2012**, *32* (7), 1401−1410.
(173) Wijesekara, S. S. R. M. D. H. R.; Mayakaduwa, S. S.; Siriwardana, A. R.; de Silva, N.; Basnayake, B. F. A.; Kawamoto, K.; Vithanage, M. Fate and Transport of Pollutants through a Municipal Solid Waste Landfill Leachate in Sri Lanka. *Environ. Earth Sci.* **2014**, *72* (5), 1707−1719.
(174) Gunarathne, V.; Ashiq, A.; Ramanayaka, S.; Wijekoon, P.; Vithanage, M. Biochar from Municipal Solid Waste for Resource Recovery and Pollution Remediation. *Environ. Chem. Lett.* **2019**, *17*, 1225−1235.
(175) Elsamadony, M.; Tawfik, A. Potential of Biohydrogen Production from Organic Fraction of Municipal Solid Waste (OFMSW) Using Pilot-Scale Dry Anaerobic Reactor. *Bioresour. Technol.* **2015**, *196*, 9−16.
(176) Wyss, K. M.; Deng, B.; Tour, J. M. Upcycling and Urban Mining for Nanomaterial Synthesis. *Nano Today* **2023**, *49*, 101781.
(177) Dong, Q.; Lele, A. D.; Zhao, X.; Li, S.; Cheng, S.; Wang, Y.; Cui, M.; Guo, M.; Brozena, A. H.; Lin, Y.; et al. Depolymerization of Plastics by Means of Electrified Spatiotemporal Heating. *Nature* **2023**, *616* (7957), 488−494.
(178) Dong, S.; Song, Y.; Ye, K.; Yan, J.; Wang, G.; Zhu, K.; Cao, D. Ultra-Fast, Low-Cost, and Green Regeneration of Graphite Anode Using Flash Joule Heating Method. *EcoMat* **2022**, *4* (5), No. e12212.
(179) Luo, J.; Zhang, J.; Guo, Z.; Liu, Z.; Dou, S.; Liu, W.-D.; Chen, Y.; Hu, W. Recycle Spent Graphite to Defect-Engineered, High-Power Graphite Anode. *Nano Res.* **2023**, *16* (4), 4240−4245.
(180) Zheng, X.; Zhao, X.; Lu, J.; Li, J.; Miao, Z.; Xu, W.; Deng, Y.; Rogach, A. L. Regeneration of Spent Cathodes of Li-Ion Batteries into Multifunctional Electrodes for Overall Water Splitting and Recharge-

https://doi.org/10.1021/acsnano.4c12350
ACS Nano XXXX, XXX, XXX−XXX

able Zn-Air Batteries by Ultrafast Carbothermal Shock. *Sci. China Mater.* **2022**, *65* (9), 2393−2400.
(181) Zhu, X.-H.; Li, Y.; Gong, M.-Q.; Mo, R.; Luo, S.-Y.; Yan, X.; Yang, S. Recycling Valuable Metals from Spent Lithium-Ion Batteries Using Carbothermal Shock Method. *Angew. Chem.* **2023**, *135* (15), No. e202300074.
(182) Jiang, H.; Zeng, C.; Zhu, W.; Luo, J.; Liu, Z.; Zhang, J.; Liu, R.; Xu, Y.; Chen, Y.; Hu, W. Boosting Cycling Stability by Regulating Surface Oxygen Vacancies of LNMO by Rapid Calcination. *Nano Res.* **2024**, *17* (4), 2671−2677.
(183) Luo, J.; Zhang, J.; Guo, Z.; Liu, Z.; Wang, C.; Jiang, H.; Zhang, J.; Fan, L.; Zhu, H.; Xu, Y.; et al. Coupling Antisite Defect and Lattice Tensile Stimulates Facile Isotropic Li-Ion Diffusion. *Adv. Mater.* **2024**, *36* (32), 2405956.
(184) Guo, Z.; Qian, G.; Wang, C.; Zhang, G.; Yin, R.; Liu, W.-D.; Liu, R.; Chen, Y. Progress in Electrode Materials for the Industrialization of Sodium-Ion Batteries. *Prog. Nat. Sci.* **2023**, *33* (1), 1−7.
(185) Cui, R.; Wang, S.; Kong, J.; Ming, Y.; Sun, T.; Miao, J.; Lv, Z.; Yan, R.; Wang, Z. Mixed Cathode and Anode Materials from Spent Lithium-Ion Battery for High-Stability Oxygen Evolution Reaction Electrode. *J. Alloy. Comp.* **2023**, *934*, 167847.
(186) Dong, Q.; Li, T.; Yao, Y.; Wang, X.; He, S.; Li, J.; Luo, J.; Zhang, H.; Pei, Y.; Zheng, C.; et al. A General Method for Regenerating Catalytic Electrodes. *Joule* **2020**, *4* (11), 2374−2386.
(187) Chen, W.; Salvatierra, R. V.; Li, J. T.; Kittrell, C.; Beckham, J. L.; Wyss, K. M.; La, N.; Savas, P. E.; Ge, C.; Advincula, P. A.; et al. Flash Recycling of Graphite Anodes. *Adv. Mater.* **2023**, *35* (8), 2207303.
(188) Oleszek, S.; Grabda, M.; Nakamura, T.; Buekens, A. Upcycling of E-Waste Plastics Containing Brominated Flame Retardants into Valuable Carbon Material. In *2018 Advances in Science and Engineering Technology International Conferences (ASET)*, 2018; IEEE, pp 1−4.
(189) Misra, N. R.; Kumar, S.; Jain, A. A review on E-waste: Fostering the Need for Green Electronics. In *2021 International Conference on Computing, Communication, and Intelligent Systems (ICCCIS)*, 2021; IEEE, pp 1032−1036.
(190) Cayumil, R.; Khanna, R.; Rajarao, R.; Mukherjee, P. S.; Sahajwalla, V. Concentration of Precious Metals during their Recovery from Electronic Waste. *Waste Manage.* **2016**, *57*, 121−130.
(191) Deng, B.; Luong, D. X.; Wang, Z.; Kittrell, C.; McHugh, E. A.; Tour, J. M. Urban Mining by Flash Joule Heating. *Nat. Commun.* **2021**, *12* (1), 5794.
(192) Deng, B.; Carter, R. A.; Cheng, Y.; Liu, Y.; Eddy, L.; Wyss, K. M.; Ucak-Astarlioglu, M. G.; Luong, D. X.; Gao, X.; JeBailey, K.; et al. High-Temperature Electrothermal Remediation of Multi-Pollutants in Soil. *Nat. Commun.* **2023**, *14* (1), 6371.
(193) Chen, X.; Wang, Y.; Zhang, L. Recent Progress in the Chemical Upcycling of Plastic Wastes. *ChemSusChem* **2021**, *14* (19), 4137−4151.
(194) Terrones, M.; Terrones, H.; Banhart, F.; Charlier, J. C.; Ajayan, P. M. Coalescence of Single-Walled Carbon Nanotubes. *Science* **2000**, *288* (5469), 1226−1229.
(195) Hirayama, H.; Kawamoto, Y.; Ohshima, Y.; Takayanagi, K. Nanospot Welding of Carbon Nanotubes. *Appl. Phys. Lett.* **2001**, *79* (8), 1169−1171.
(196) Jin, C.; Suenaga, K.; Iijima, S. Plumbing Carbon Nanotubes. *Nat. Nanotechnol.* **2008**, *3* (1), 17−21.
(197) Santini, C. A.; Vereecken, P. M.; Volodin, A.; Groeseneken, G.; De Gendt, S.; Haesendonck, C. V. A Study of Joule Heating-Induced Breakdown of Carbon Nanotube Interconnects. *Nanotechnology* **2011**, *22* (39), 395202.
(198) Yoo, B.; Xu, Z.; Ding, F. How Single-Walled Carbon Nanotubes are Transformed into Multiwalled Carbon Nanotubes during Heat Treatment. *ACS Omega* **2021**, *6* (5), 4074−4079.
(199) Zhao, S.; Miyata, Y.; Shinohara, H.; Kitaura, R. Direct Observation of Zipper-Like Wall-to-Wall Coalescence of Double-Wall Carbon Nanotubes. *Carbon* **2014**, *71*, 159−165.
(200) Yao, Y.; Fu, K. K.; Zhu, S.; Dai, J.; Wang, Y.; Pastel, G.; Chen, Y.; Li, T.; Wang, C.; Li, T.; et al. Carbon Welding by Ultrafast Joule Heating. *Nano Lett.* **2016**, *16* (11), 7282−7289.
(201) Banhart, F. The Formation of a Connection between Carbon Nanotubes in an Electron Beam. *Nano Lett.* **2001**, *1* (6), 329−332.
(202) Liu, Y.; Liang, C.; Wei, A.; Jiang, Y.; Tian, Q.; Wu, Y.; Xu, Z.; Li, Y.; Guo, F.; Yang, Q.; et al. Solder-Free Electrical Joule Welding of Macroscopic Graphene Assemblies. *Mater. Today Nano* **2018**, *3*, 1−8.
(203) Famprikis, T.; Canepa, P.; Dawson, J. A.; Islam, M. S.; Masquelier, C. Fundamentals of Inorganic Solid-State Electrolytes for Batteries. *Nat. Mater.* **2019**, *18* (12), 1278−1291.
(204) Li, Y.; Han, J.-T.; Wang, C.-A.; Xie, H.; Goodenough, J. B. Optimizing Li^+ Conductivity in a Garnet Framework. *J. Mater. Chem.* **2012**, *22* (30), 15357−15361.
(205) Lin, Y.; Luo, N.; Quattrocchi, E.; Ciucci, F.; Wu, J.; Kermani, M.; Dong, J.; Hu, C.; Grasso, S. Ultrafast High-Temperature Sintering (UHS) of $Li_{1.3}Al_{0.3}Ti_{1.7}(PO_4)_3$. *Ceram. Int.* **2021**, *47* (15), 21982−21987.
(206) Li, H. W.; Zhao, Y. P.; Chen, G. Q.; Li, M. H.; Wei, Z. F.; Fu, X. S.; Zhou, W. L. SiC-Based Ceramics with Remarkable Electrical Conductivity Prepared by Ultrafast High-Temperature Sintering. *J. Eur. Ceram. Soc.* **2023**, *43* (5), 2269−2274.
(207) Talalay, P. G.; Li, Y.; Sysoev, M. A.; Hong, J.; Li, X.; Fan, X. Thermal Tips for Ice Hot-Point Drilling: Experiments and Preliminary Thermal Modeling. *Cold Reg. Sci. Technol.* **2019**, *160*, 97−109.
(208) Albisetti, E.; Calò, A.; Zanut, A.; Zheng, X.; de Peppo, G. M.; Riedo, E. Thermal Scanning Probe Lithography. *Nat. Rev. Method. Prim.* **2022**, *2* (1), 32.
(209) Wolf, H.; Cho, Y. K. R.; Karg, S.; Mensch, P.; Schwemmer, C.; Knoll, A.; Spieser, M.; Bisig, S.; Rawlings, C.; Paul, P. Thermal Scanning Probe Lithography (T-SPL) for Nano-Fabrication. In *2019 Pan Pacific Microelectronics Symposium (Pan Pacific)*, 2019; IEEE, pp 1−9.
(210) Paul, P. C. Chapter 16 - Thermal Scanning Probe Lithography. In *Frontiers of Nanoscience*; Robinson, A.; Lawson, R., Eds.; Elsevier: Amsterdam, 2016; pp 543−561.
(211) Tang, S. W.; Uddin, M. H.; Tong, W. Y.; Pasic, P.; Yuen, W.; Thissen, H.; Lam, Y. W.; Voelcker, N. H. Replication of a Tissue Microenvironment by Thermal Scanning Probe Lithography. *ACS Appl. Mater. Interfaces* **2019**, *11* (21), 18988−18994.
(212) Ryu, Y. K.; Knoll, A. W. Oxidation and Thermal Scanning Probe Lithography for High-Resolution Nanopatterning and Nanodevices. In *Electrical Atomic Force Microscopy for Nanoelectronics*; Celano, U., Ed.; Springer International Publishing: Berlin, 2019; pp 143−172.
(213) Cheong, L. L.; Paul, P.; Holzner, F.; Despont, M.; Coady, D. J.; Hedrick, J. L.; Allen, R.; Knoll, A. W.; Duerig, U. Thermal Probe Maskless Lithography for 27.5 nm Half-Pitch Si Technology. *Nano Lett.* **2013**, *13* (9), 4485−4491.
(214) Ryu Cho, Y. K.; Rawlings, C. D.; Wolf, H.; Spieser, M.; Bisig, S.; Reidt, S.; Sousa, M.; Khanal, S. R.; Jacobs, T. D. B.; Knoll, A. W. Sub-10 Nanometer Feature Size in Silicon Using Thermal Scanning Probe Lithography. *ACS Nano* **2017**, *11* (12), 11890−11897.
(215) Conde-Rubio, A.; Liu, X.; Boero, G.; Brugger, J. Edge-Contact MoS_2 Transistors Fabricated Using Thermal Scanning Probe Lithography. *ACS Appl. Mater. Interfaces* **2022**, *14* (37), 42328−42336.
(216) Peng, M.; Wen, Z.; Xie, L.; Cheng, J.; Jia, Z.; Shi, D.; Zeng, H.; Zhao, B.; Liang, Z.; Li, T.; et al. 3D Printing of Ultralight Biomimetic Hierarchical Graphene Materials with Exceptional Stiffness and Resilience. *Adv. Mater.* **2019**, *31* (35), 1902930.
(217) Yang, M.; Zhao, N.; Cui, Y.; Gao, W.; Zhao, Q.; Gao, C.; Bai, H.; Xie, T. Biomimetic Architectured Graphene Aerogel with Exceptional Strength and Resilience. *ACS Nano* **2017**, *11* (7), 6817−6824.
(218) Liu, X.; Howell, S. T.; Conde-Rubio, A.; Boero, G.; Brugger, J. Thermomechanical Nanocutting of 2D Materials. *Adv. Mater.* **2020**, *32* (31), 2001232.
(219) Wang, W.; Pfeiffer, P.; Schmidt-Mende, L. Direct Patterning of Metal Chalcogenide Semiconductor Materials. *Adv. Funct. Mater.* **2020**, *30* (27), 2002685.
(220) Tovee, P. D.; Pumarol, M. E.; Rosamond, M. C.; Jones, R.; Petty, M. C.; Zeze, D. A.; Kolosov, O. V. Nanoscale Resolution Scanning Thermal Microscopy Using Carbon Nanotube Tipped Thermal Probes. *Phys. Chem. Chem. Phys.* **2014**, *16* (3), 1174−1181.

https://doi.org/10.1021/acsnano.4c12350
ACS Nano XXXX, XXX, XXX−XXX

(221) Prasher, R. S.; Phelan, P. E. Microscopic and Macroscopic Thermal Contact Resistances of Pressed Mechanical Contacts. *J. Appl. Phys.* **2006**, *100* (6), 063538.
(222) Ordonez-Miranda, J.; Yang, R.; Alvarado-Gil, J. J. A Constitutive Equation for Nano-to-Macro-Scale Heat Conduction Based on The Boltzmann Transport Equation. *J. Appl. Phys.* **2011**, *109* (8), 084319.
(223) Xie, H.; Liu, N.; Zhang, Q.; Zhong, H.; Guo, L.; Zhao, X.; Li, D.; Liu, S.; Huang, Z.; Lele, A. D.; et al. A Stable Atmospheric-Pressure Plasma for Extreme-Temperature Synthesis. *Nature* **2023**, *623* (7989), 964−971.
(224) Liu, X.; Huang, Z.; Zheng, X.; Shahrjerdi, D.; Riedo, E. Nanofabrication of Graphene Field-Effect Transistors by Thermal Scanning Probe Lithography. *APL Mater.* **2021**, *9* (1), 011107.
(225) Ryu, Y. K.; Dago, A. I.; He, Y.; Espinosa, F. M.; López-Elvira, E.; Munuera, C.; Garcia, R. Sub-10 nm Patterning of Few-Layer MoS_2 and $MoSe_2$ Nanolectronic Devices by Oxidation Scanning Probe Lithography. *Appl. Surf. Sci.* **2021**, *539*, 148231.
(226) Prasher, R. Acoustic Mismatch Model for Thermal Contact Resistance of van Der Waals Contacts. *Appl. Phys. Lett.* **2009**, *94* (4), 041905.
(227) Mosadegh, B.; Polygerinos, P.; Keplinger, C.; Wennstedt, S.; Shepherd, R. F.; Gupta, U.; Shim, J.; Bertoldi, K.; Walsh, C. J.; Whitesides, G. M. Pneumatic Networks for Soft Robotics that Actuate Rapidly. *Adv. Funct. Mater.* **2014**, *24* (15), 2163−2170.
(228) Chun, K.-Y.; Hyeong Kim, S.; Kyoon Shin, M.; Hoon Kwon, C.; Park, J.; Tae Kim, Y.; Spinks, G. M.; Lima, M. D.; Haines, C. S.; Baughman, R. H.; et al. Hybrid Carbon Nanotube Yarn Artificial Muscle Inspired by Spider Dragline Silk. *Nat. Commun.* **2014**, *5* (1), 3322.
(229) Haines, C. S.; Lima, M. D.; Li, N.; Spinks, G. M.; Foroughi, J.; Madden, J. D. W.; Kim, S. H.; Fang, S.; Jung de Andrade, M.; Göktepe, F.; et al. Artificial Muscles from Fishing Line and Sewing Thread. *Science* **2014**, *343* (6173), 868−872.
(230) Li, M.; Pal, A.; Aghakhani, A.; Pena-Francesch, A.; Sitti, M. Soft Actuators for Real-World Applications. *Nat. Rev. Mater.* **2022**, *7* (3), 235−249.
(231) Ryu, S.; Lee, Y.; Hwang, J.-W.; Hong, S.; Kim, C.; Park, T. G.; Lee, H.; Hong, S. H. High-Strength Carbon Nanotube Fibers Fabricated by Infiltration and Curing of Mussel-Inspired Catecholamine Polymer. *Adv. Mater.* **2011**, *23* (17), 1971−1975.
(232) Jeong, J.-H.; Mun, T. J.; Kim, H.; Moon, J. H.; Lee, D. W.; Baughman, R. H.; Kim, S. J. Carbon Nanotubes-Elastomer Actuator Driven Electrothermally by Low-Voltage. *Nanoscale Adv.* **2019**, *1* (3), 965−968.
(233) Lima, M. D.; Li, N.; Jung de Andrade, M.; Fang, S.; Oh, J.; Spinks, G. M.; Kozlov, M. E.; Haines, C. S.; Suh, D.; Foroughi, J.; et al. Electrically, Chemically, and Photonically Powered Torsional and Tensile Actuation of Hybrid Carbon Nanotube Yarn Muscles. *Science* **2012**, *338* (6109), 928−932.
(234) Mu, J.; Jung de Andrade, M.; Fang, S.; Wang, X.; Gao, E.; Li, N.; Kim, S. H.; Wang, H.; Hou, C.; Zhang, Q.; et al. Sheath-Run Artificial Muscles. *Science* **2019**, *365* (6449), 150−155.
(235) Wang, C.; Wang, Y.; Yao, Y.; Luo, W.; Wan, J.; Dai, J.; Hitz, E.; Fu, K.; Hu, L. A Solution-Processed High-Temperature, Flexible, Thin-Film Actuator. *Adv. Mater.* **2016**, *28* (39), 8618−8624.
(236) Zou, J.; Cai, Z.; Lai, Y.; Tan, J.; Zhang, R.; Feng, S.; Wang, G.; Lin, J.; Liu, B.; Cheng, H.-M. Doping Concentration Modulation in Vanadium-Doped Monolayer Molybdenum Disulfide for Synaptic Transistors. *ACS Nano* **2021**, *15* (4), 7340−7347.
(237) Gao, Y.; Hong, Y.-L.; Yin, L.-C.; Wu, Z.; Yang, Z.; Chen, M.-L.; Liu, Z.; Ma, T.; Sun, D.-M.; Ni, Z.; et al. Ultrafast Growth of High-Quality Monolayer WSe_2 on Au. *Adv. Mater.* **2017**, *29* (29), 1700990.
(238) Wada, R.; Takahashi, H. Time Response Characteristics of a Highly Sensitive Barometric Pressure Change Sensor Based on MEMS Piezoresistive Cantilevers. *Jpn. J. Appl. Phys.* **2020**, *59* (7), 070906.
(239) Dong, Q.; Yao, Y.; Cheng, S.; Alexopoulos, K.; Gao, J.; Srinivas, S.; Wang, Y.; Pei, Y.; Zheng, C.; Brozena, A. H.; et al. Programmable Heating and Quenching for Efficient Thermochemical Synthesis. *Nature* **2022**, *605* (7910), 470−476.
(240) Huang, P.; Li, Z.; Chen, L.; Li, Y.; Liu, Z.; Zhang, J.; Luo, J.; Zhang, W.; Liu, W.-D.; Zhang, X.; et al. Ultrafast Dual-Shock Chemistry Synthesis of Ordered/Disordered Hybrid Carbon Anodes: High-Rate Performance of Li-Ion Batteries. *ACS Nano* **2024**, *18* (28), 18344−18354.
(241) Shi, L.; Shao, Y.; Fan, Z.; Wang, R.; Lu, C.; Yao, K. Connecting the Composition, Structure, and Magnetic Property in High-Entropy Metallic Glasses. *Acta Mater.* **2023**, *254*, 118983.
(242) Zhang, Y.; Lu, Z. P.; Ma, S. G.; Liaw, P. K.; Tang, Z.; Cheng, Y. Q.; Gao, M. C. Guidelines in Predicting Phase Formation of High-Entropy Alloys. *MRS Commun.* **2014**, *4* (2), 57−62.
(243) Qiao, L.; Ramanujan, R. V.; Zhu, J. Machine Learning Discovery of a New Cobalt Free Multi-Principal-Element Alloy with Excellent Mechanical Properties. *Mater. Sci. Eng., A* **2022**, *845*, 143198.
(244) Ding, Q.; Zhang, Y.; Chen, X.; Fu, X.; Chen, D.; Chen, S.; Gu, L.; Wei, F.; Bei, H.; Gao, Y.; et al. Tuning Element Distribution, Structure and Properties by Composition in High-Entropy Alloys. *Nature* **2019**, *574* (7777), 223−227.
(245) Huang, Z.; Yao, Y.; Hu, L.; Shahbazian-Yassar, R. In situ TEM Observation of Nanoparticles Formation during Carbothermal Shock. *Microsc. Microanal.* **2019**, *25* (S2), 1534−1535.
(246) Saray, M. T.; Shahbazian-Yassar, R. In Situ TEM Studies on the Nucleation and Growth of Multicomponent Alloy Nanoparticles on 2D Materials. *Microsc. Microanal.* **2021**, *27* (S1), 2978−2980.
(247) Yao, Y.; Dong, Q.; Brozena, A.; Luo, J.; Miao, J.; Chi, M.; Wang, C.; Kevrekidis, I. G.; Ren, Z. J.; Greeley, J.; et al. High-Entropy Nanoparticles: Synthesis-Structure-Property Relationships and Data-Driven Discovery. *Science* **2022**, *376* (6589), No. eabn3103.
(248) Cai, J.; Chu, X.; Xu, K.; Li, H.; Wei, J. Machine Learning-Driven New Material Discovery. *Nanoscale Adv.* **2020**, *2* (8), 3115−3130.
(249) Wei, J.; Chu, X.; Sun, X.-Y.; Xu, K.; Deng, H.-X.; Chen, J.; Wei, Z.; Lei, M. Machine Learning in Materials Science. *InfoMat* **2019**, *1* (3), 338−358.
(250) Moosavi, S. M.; Jablonka, K. M.; Smit, B. The Role of Machine Learning in the Understanding and Design of Materials. *J. Am. Chem. Soc.* **2020**, *142* (48), 20273−20287.
(251) Lopez, E.; Gonzalez, D.; Aguado, J. V.; Abisset-Chavanne, E.; Cueto, E.; Binetruy, C.; Chinesta, F. A Manifold Learning Approach for Integrated Computational Materials Engineering. *Arch. Comput. Method. Eng.* **2018**, *25* (1), 59−68.
(252) Coley, C. W.; Green, W. H.; Jensen, K. F. Machine Learning in Computer-Aided Synthesis Planning. *Acc. Chem. Res.* **2018**, *51* (5), 1281−1289.
(253) Ryu, B.; Wang, L.; Pu, H.; Chan, M. K. Y.; Chen, J. Understanding, Discovery, and Synthesis of 2D Materials Enabled by Machine Learning. *Chem. Soc. Rev.* **2022**, *51* (6), 1899−1925.
(254) Frey, N. C.; Akinwande, D.; Jariwala, D.; Shenoy, V. B. Machine Learning-Enabled Design of Point Defects in 2D Materials for Quantum and Neuromorphic Information Processing. *ACS Nano* **2020**, *14* (10), 13406−13417.
(255) Wen, C.; Zhang, Y.; Wang, C.; Xue, D.; Bai, Y.; Antonov, S.; Dai, L.; Lookman, T.; Su, Y. Machine Learning Assisted Design of High Entropy Alloys with Desired Property. *Acta Mater.* **2019**, *170*, 109−117.
(256) Huang, W.; Martin, P.; Zhuang, H. L. Machine-Learning Phase Prediction of High-Entropy Alloys. *Acta Mater.* **2019**, *169*, 225−236.
(257) Kaufmann, K.; Vecchio, K. S. Searching for High Entropy Alloys: A Machine Learning Approach. *Acta Mater.* **2020**, *198*, 178−222.
(258) Zhang, Y.; Wen, C.; Wang, C.; Antonov, S.; Xue, D.; Bai, Y.; Su, Y. Phase Prediction in High Entropy Alloys with a Rational Selection of Materials Descriptors and Machine Learning Models. *Acta Mater.* **2020**, *185*, 528−539.
(259) Rao, Z.; Tung, P.-Y.; Xie, R.; Wei, Y.; Zhang, H.; Ferrari, A.; Klaver, T. P. C.; Körmann, F.; Sukumar, P. T.; Kwiatkowski da Silva, A.; et al. Machine Learning-Enabled High-Entropy Alloy Discovery. *Science* **2022**, *378* (6615), 78−85.

https://doi.org/10.1021/acsnano.4c12350
ACS Nano XXXX, XXX, XXX−XXX

(260) Zhou, Z.; Zhou, Y.; He, Q.; Ding, Z.; Li, F.; Yang, Y. Machine Learning Guided Appraisal and Exploration of Phase Design for High Entropy Alloys. *npj Comput. Mater.* **2019**, *5* (1), 128.
(261) Krishna, Y. V.; Jaiswal, U. K.; R, R. M. Machine Learning Approach to Predict New Multiphase High Entropy Alloys. *Scripta Mater.* **2021**, *197*, 113804.
(262) Chang, Y.-J.; Jui, C.-Y.; Lee, W.-J.; Yeh, A.-C. Prediction of the Composition and Hardness of High-Entropy Alloys by Machine Learning. *JOM* **2019**, *71* (10), 3433−3442.
(263) Beckham, J. L.; Wyss, K. M.; Xie, Y.; McHugh, E. A.; Li, J. T.; Advincula, P. A.; Chen, W.; Lin, J.; Tour, J. M. Machine Learning Guided Synthesis of Flash Graphene. *Adv. Mater.* **2022**, *34* (12), 2106506.
(264) Kruglov, I.; Sergeev, O.; Yanilkin, A.; Oganov, A. R. Energy-Free Machine Learning Force Field for Aluminum. *Sci. Rep.* **2017**, *7* (1), 8512.
(265) Yamashita, T.; Sato, N.; Kino, H.; Miyake, T.; Tsuda, K.; Oguchi, T. Crystal Structure Prediction Accelerated by Bayesian Optimization. *Phys. Rev. Mater.* **2018**, *2* (1), 013803.
(266) Jaeger, S.; Fulle, S.; Turk, S. Mol2vec: Unsupervised Machine Learning Approach with Chemical Intuition. *J. Chem. Inf. Model.* **2018**, *58* (1), 27−35.
(267) Ture, M.; Tokatli, F.; Kurt, I. Using Kaplan-Meier Analysis together with Decision Tree Methods (C&RT, CHAID, QUEST, C4.5 and ID3) in Determining Recurrence-Free Survival of Breast Cancer Patients. *Expert Sys. Appl.* **2009**, *36* (2, Part 1), 2017−2026.
(268) Segal, M. R. *Machine Learning Benchmarks and Random Forest Regression*; Center for Bioinformatics & Molecular, UC San Francisco, 2004.
(269) Chen, T.; Guestrin, C. Xgboost: A Scalable Tree Boosting System. In *Proceedings of the 22nd Acm Sigkdd International Conference on Knowledge Discovery and Data Mining*; Association for Computing Machinery: New York, 2016; pp 785−794.
(270) Song, D.; Chen, X.; Lin, Z.; Tang, Z.; Ma, W.; Zhang, Q.; Li, Y.; Zhang, X. Usability Identification Framework and High-Throughput Screening of Two-Dimensional Materials in Lithium Ion Batteries. *ACS Nano* **2021**, *15* (10), 16469−16477.
(271) Kumbhakar, M.; Khandelwal, A.; Jha, S. K.; Kante, M. V.; Keßler, P.; Lemmer, U.; Hahn, H.; Aghassi-Hagmann, J.; Colsmann, A.; Breitung, B.; et al. High-Throughput Screening of High-Entropy Fluorite-Type Oxides as Potential Candidates for Photovoltaic Applications. *Adv. Energy Mater.* **2023**, *13* (24), 2204337.
(272) Li, Y.-L.; Kinloch, I. A.; Windle, A. H. Direct Spinning of Carbon Nanotube Fibers from Chemical Vapor Deposition Synthesis. *Science* **2004**, *304* (5668), 276−278.
(273) Hou, P.-X.; Zhang, F.; Zhang, L.; Liu, C.; Cheng, H.-M. Synthesis of Carbon Nanotubes by Floating Catalyst Chemical Vapor Deposition and Their Applications. *Adv. Funct. Mater.* **2022**, *32* (11), 2108541.
(274) Lee, S.-H.; Park, J.; Park, J. H.; Lee, D.-M.; Lee, A.; Moon, S. Y.; Lee, S. Y.; Jeong, H. S.; Kim, S. M. Deep-Injection Floating-Catalyst Chemical Vapor Deposition to Continuously Synthesize Carbon Nanotubes with High Aspect Ratio and High Crystallinity. *Carbon* **2021**, *173*, 901−909.
(275) Yang, Y.; Song, B.; Ke, X.; Xu, F.; Bozhilov, K. N.; Hu, L.; Shahbazian-Yassar, R.; Zachariah, M. R. Aerosol Synthesis of High Entropy Alloy Nanoparticles. *Langmuir* **2020**, *36* (8), 1985−1992.
(276) Qiao, Y.; Chen, C.; Liu, Y.; Liu, Y.; Dong, Q.; Yao, Y.; Wang, X.; Shao, Y.; Wang, C.; Hu, L. Continuous Fly-Through High-Temperature Synthesis of Nanocatalysts. *Nano Lett.* **2021**, *21* (11), 4517−4523.
(277) Cheng, Y.; Cui, G.; Liu, C.; Liu, Z.; Yan, L.; Liu, B.; Yuan, H.; Shi, P.; Jiang, J.; Huang, K.; et al. Electric Current Aligning Component Units during Graphene Fiber Joule Heating. *Adv. Funct. Mater.* **2022**, *32* (11), 2103493.
(278) Juang, Z.-Y.; Wu, C.-Y.; Lu, A.-Y.; Su, C.-Y.; Leou, K.-C.; Chen, F.-R.; Tsai, C.-H. Graphene Synthesis by Chemical Vapor Deposition and Transfer by a Roll-To-Roll Process. *Carbon* **2010**, *48* (11), 3169−3174.
(279) Hong, N.; Kireev, D.; Zhao, Q.; Chen, D.; Akinwande, D.; Li, W. Roll-to-Roll Dry Transfer of Large-Scale Graphene. *Adv. Mater.* **2022**, *34* (3), 2106615.
(280) Bae, S.; Kim, H.; Lee, Y.; Xu, X.; Park, J.-S.; Zheng, Y.; Balakrishnan, J.; Lei, T.; Ri Kim, H.; Song, Y. I.; et al. Roll-to-Roll Production of 30-in. Graphene Films for Transparent Electrodes. *Nat. Nanotechnol.* **2010**, *5* (8), 574−578.
(281) Gao, Y.; Liu, Z.; Sun, D.-M.; Huang, L.; Ma, L.-P.; Yin, L.-C.; Ma, T.; Zhang, Z.; Ma, X.-L.; Peng, L.-M.; et al. Large-Area Synthesis of High-Quality and Uniform Monolayer WS_2 on Reusable Au Foils. *Nat. Commun.* **2015**, *6* (1), 8569.
(282) Lim, Y. R.; Han, J. K.; Kim, S. K.; Lee, Y. B.; Yoon, Y.; Kim, S. J.; Min, B. K.; Kim, Y.; Jeon, C.; Won, S.; et al. Roll-to-Roll Production of Layer-Controlled Molybdenum Disulfide: A Platform for 2D Semiconductor-Based Industrial Applications. *Adv. Mater.* **2018**, *30* (5), 1705270.
(283) Wells, R. A.; Johnson, H.; Lhermitte, C. R.; Kinge, S.; Sivula, K. Roll-to-Roll Deposition of Semiconducting 2D Nanoflake Films of Transition Metal Dichalcogenides for Optoelectronic Applications. *ACS Appl. Nano Mater.* **2019**, *2* (12), 7705−7712.

https://doi.org/10.1021/acsnano.4c12350
ACS Nano XXXX, XXX, XXX−XXX